CHALMERS

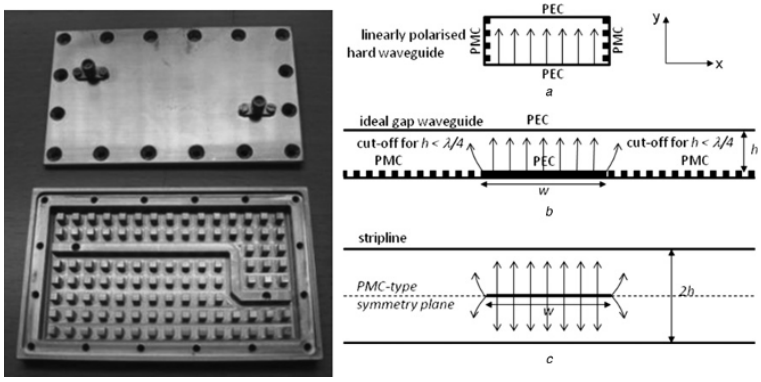

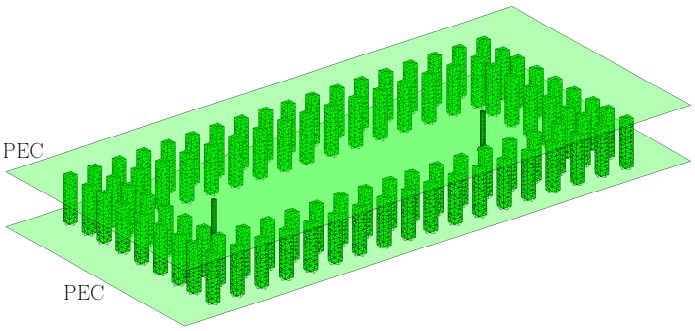

Fast Analysis of Gap Waveguides using the Characteristic Basis Function Method and Advanced Green's Function Approaches

Master's Thesis

Pegah Takook

Department of Signals and Systems
Antenna Group
Chalmers University of Technology
Gothenburg, Sweden 2012
Master's Thesis 2012:6

Fast Analysis of Gap Waveguides using the Characteristic Basis Function Method and Advanced Green's Function Approaches

MASTER's THESIS
as part of mandatory clauses in
fulfillment of Master's Degree from the
Chalmers University of Technology, Gothenburg, Sweden

by

Pegah Takook
Department of Signals and Systems

June, 2012

Fast Analysis of Gap Waveguides using the Characteristic Basis Function Method and Advanced Green's Function Approaches / by
Pegah Takook. - Gothenburg : Chalmers University of Technology, 2012.

This thesis is carried out under supervision of:
Dr. Rob Maaskant

Examiner:
Prof. Dr. Per-Simon Kildal

Keywords: computational electromagnetics / method of moments / Green's functions / integral equations.
Subject headings: computational electromagnetics / electric field integral equation / characteristic basis function method

Technical Report No. 2012:xx
Antenna Group, Department of Signals & Systems
Chalmers University of Technology,
SE-41296, Gothenburg, Sweden.
Telephone: +46 31 772 1000

Cover design: Pegah Takook
Press: Chalmers Reproservice, Göteborg

The work presented in this thesis has been financed partly by the Netherlands Organization for Scientific Research (NWO), and has been performed at the Chalmers University of Technology, Sweden.

Abstract

To overcome the problems of ohmic and dielectric losses in conventional microstrip and coplanar (CPW) transmission lines at mm wave and sub-mm wave frequencies, a novel low-loss low-cost waveguide and transmission-line technology has been proposed, referred to as the gap waveguide technology. The presence of small geometrical details in the gap waveguide structure requires a fine discretization of the current in method of moment (MoM) codes leading to a large matrix equation. Moreover, an electrically large structure leads to a large matrix equation as well. The solution of this multi-scale problem is therefore time demanding and memory consuming. Hence, the fast analysis and optimization of these gap waveguides requires the development of tailored numerically efficient computational electromagnetic methods.

In this thesis, we study a number of efficiency enhancement techniques that can be employed to expedient the numerical analysis of conventional MoM codes. Starting with the parallel-plate Green's function concept, we examine different methods for the fast computation of the parallel-plate dyadic Green's function, among which the Shanks-accelerated spatial Green's function method, the Ewald summation method, and the spectral-domain summation method. It is found that for our type of problems, where only few digits of accuracy is required, the Shanks-accelerated spatial Green's function method is the preferred method among the others to compute the parallel-plate dyadic Green's function.

After formulating and computing the parallel-plate Green's function, the MoM and its applications for the numerical evaluation of electromagnetic structures is studied in more detail. Toward this end, we first describe the procedure for the development, discretization and solution of the electric field integral equation (EFIE). Afterwards, the verification of the herein implemented MoM is examined through the in-house developed CAESAR software, and the numerically computed results are validated for several parallel-plate waveguiding structure through the commercially available HFSS software.

To further accelerate the numerical computations, we study the Padé approximation method in conjunction with an adaptive frequency sampling scheme for minimizing the number of

frequency samples that are needed for the prediction of the input impedance characteristics of a multi-port structure within a certain bandwidth. The adaptive estimation method is verified through a circuit model as well as for a parallel-plate waveguiding structure.

Finally, the Characteristic Basis Function Method (CBFM) is studied as another numerically efficient method which can be used to solve large electromagnetic problems. We describe the proposed procedure for generating Characteristic Basis Functions, which are macro-domain basis functions defined on each building block of a geometrically subdivided structure. Furthermore, translation symmetry is exploited and the Adaptive Cross Approximation is used to improve the computational efficiency. Numerical results are presented to demonstrate the accuracy and the computational efficiency of the proposed CBFM compared to a conventional MoM approach and the HFSS software.

Acknowledgements

I wish to thank, first and foremost, my supervisor, Dr. Rob Maaskant who was abundantly helpful and offered invaluable assistance and support during my thesis. This thesis would not have been possible without the guidance of Dr. Rob Maaskant. Finally, I would like to express my deepest gratitude to Prof. Per-Simon Kildal who provided me the opportunity to work in the antenna group and financially supported this thesis.

Contents

Chapter 1

Introduction

In this chapter, we introduce the concept of the gap waveguide technology, and provide a brief motivation for the numerical modeling and studies that are performed in this thesis. Afterwards, a short description of the chapters is given.

1.1 The Gap Waveguide Technology

The gap waveguide is a recently developed technology aimed to be used for high frequency applications, i.e, at millimeter and submillimeter wave frequencies [1]. This novel low-cost technology is a metal-only structure and therefore overcomes the dielectric losses of conventional transmission-line structures at high frequencies. The herein considered gap waveguide employs perfect electric conductors as the upper and lower ground planes of a parallel-plate waveguide. One of the plates usually consists of a ridge, Fig. 1.1(a), or a groove, Fig. 1.1(b), surrounded by a bed of nails or metal pins [2]. This bed of nails, which is applied to realize the perfect magnetic conductor condition, creates a high impedance condition when the parallel-plate distance is smaller than a quarter wavelength. For the ridge gap waveguide, it is then possible to excite a quasi-TEM wave which is confined only along the ridge in an octave bandwidth. A structure that can be used instead of the bed of nails, for realizing an artificial magnetic conductor (AMC) is the mushroom-type EBG. This structure is more suitable for low frequency applications due to its compact size compared to the metal pin structure [3, 4].

Gap waveguides can be realized in ridge, groove, or microstrip transmission-line technology. The ridge gap waveguide supports a quasi-TEM mode, while the groove gap waveguide can support TE/TM modes as in conventional rectangular waveguides. The microstrip type of gap waveguides, used in low frequency applications, are compact in size and work as inverted microstrip lines. An advantageous property of gap waveguides is that no metal contact is required between the upper and lower plates of the parallel-plate waveguide, since the bed of nails which surrounds the ridge or groove prevents the fields from leaking transverse to the propagation direction. It is pointed out that ideal rectangular waveguides should not have air gaps between metal parts, which cannot easily be achieved at high frequencies, so that the leakage problem is almost unavoidable in rectangular waveguides [5].

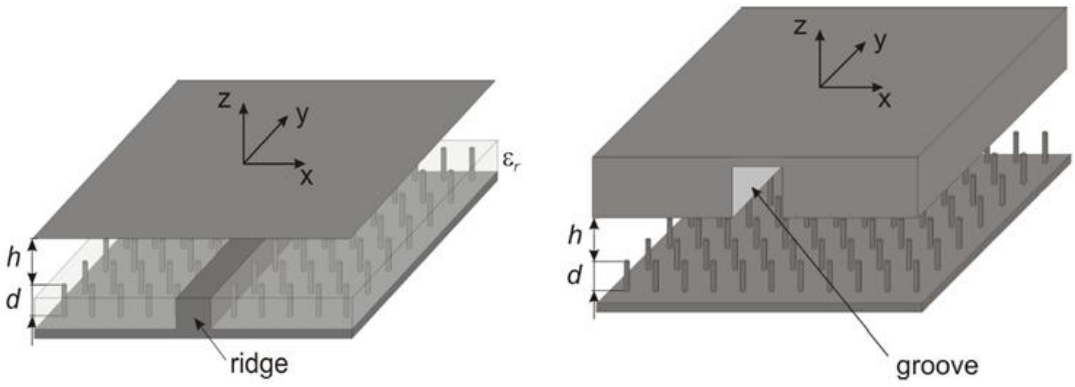

(a) (b)

Figure 1.1: A possible realization of a ridge and Groove gap waveguide.

1.2 Motivation

At this moment, the numerical analysis of gap waveguides using commercially available CEM software tools is a very time-consuming (if not impossible) task. This is caused by the tiny geometrical details that the gap waveguide exhibits, which in turn requires a fine discretization of the geometrical structure and Maxwell's field equations. On the contrary, the whole structure itself can be electrically large and thus represents a multiscale problem. This leads to an extremely large matrix equation requiring huge amounts of RAM memory and very large solve times. Hence, there is an urgent need to develop customized

computational electromagnetic (CEM) codes to expedient the numerical analysis of the next generation waveguiding structures.

To allow for a fast numerical analysis (and optimization) of these gap-waveguide structures, it is proposed to employ advanced Green's function approaches to analytically account for the EM fields generated by an elementary current inside a perfect electrically conducting enclosure (rectangular box and/or parallel plates). Accordingly, an integral equation is formulated for the equivalent unknown current representing the physical one. The method-of-moments is then used to discretize the integral equation to arrive at a relatively large matrix equation. The size of this matrix equation can be reduced further by employing the Characteristic Basis Function Method. The resulting system of linear equations can then be solved very rapidly.

1.3 Outline

In Chapter 2, the thesis starts with a geometrical description of the recently proposed gap waveguide structures and the motivation to consider the infinite parallel-plate waveguide as the basic structure in the numerical analysis. The mathematical formulation of the problem is developed afterwards, which includes the formulation of the electromagnetic fields radiated in free space for an infinitesimal dipole and through using the magnetic vector and electric scalar potentials. After defining the free space Green's function, the electric field integral equation is derived and descretized using Galerkin's method. The dyadic parallel-plate Green's function is formulated through three orthogonally-polarized dipole currents located in between two infinite parallel-plates forming the waveguide. Afterwards, different acceleration methods are introduced for the fast computation of the dyadic parallel plate Green's function. Starting with the infinite spatial summation, the corresponding Green's function series is transformed to the spectral domain. The Ewald method is presented which is a combination of the spectral and spatial summation. Finally, two techniques utilizing the Shanks transformation and the asymptotic form of the Hankel function are shown to further accelerate the computation of the dyadic parallel-plate Green's function.

In Chapter 3, the numerical evaluation of the dyadic Parallel plate Green's function is studied through different acceleration methods and convergence results are presented to compare the computational efficiency of the different techniques.

The method of moments is described in detail in Chapter 4, where the selection of basis and test functions, the moment matrix computation, the singularity in the potential integrals, and the solution of the moment matrix equation are discussed. Also, the application of the moment method to a waveguide structure is examined through the CAESAR software and the numerical results are compared to those obtained from a simulation done with the HFSS software.

In Chapter 5, the Padé rational function fitting model is introduced. This rational function is used for the interpolation of frequency dependent data sets. The method is applied to a parallel-plate waveguiding structure of two monopoles, in order to rapidly compute its impedance characteristics in a frequency range of $10 - 60$ GHz. Accordingly, an adaptive frequency sampling scheme is developed for minimizing the number of required frequency sampling points.

In Chapter 6, the Characteristic Basis Function Method (CBFM) is described to solve an electrically large groove gap waveguiding structure. After formulating the basic principles of the entire-domain basis function method, we explain the methodology of employing characteristic basis functions and describe a procedure for generating them. Also, we introduce the adaptive cross approximation (ACA) algorithm for the fast generation of the reduced matrix resulting from the application of the CBFM. We conclude by presenting the accuracy and efficiency of the CBFM through several numerical examples.

Finally, in Chapter 7, the conclusions and recommendations are presented.

Chapter 2

Mathematical Problem Formulation

This chapter starts with the derivation of the field equations for an electric dipole point source located in a parallel-plate waveguiding region. This is done with the help of a mixed potential formulation. Afterwards, the Electric Field Integral Equation (EFIE) is developed and we see how the application of the moment method can be used to determine the equivalent electric current distribution. Finally, several methods for accelerating the evaluation of the infinite series summation arising in the dyadic parallel-plate Green's function computation are described, among which are the Shanks-accelerated spatial summation, the spectral, and the Ewald summation method.

2.1 Introduction

Consider Fig. 2.1, which illustrates an example of a ridge-gap waveguide that has been manufactured and measured [5]. It is shown that the propagating electric field is confined in the gap formed by the ridge and the top ground plane, which therefore demonstrates a close resemblance with the TEM stripline transmission line. Indeed, below the parallel-plate cut-off frequency, when the distance between the upper metallic surface and the bottom ground plane is smaller than $\lambda/4$, a single dispersion-free quasi TEM-wave can be excited that can propagate over an octave bandwidth [1, 3].

In the stop-band, the pins inside the PEC box prevent the fields from leaking towards

its sidewalls, so that one can remove the sidewalls without affecting the field propagation characteristics at these frequencies. Hence, the equivalent structure that can be analyzed constitutes a bed of nails which is connected only to the bottom (or top) plate of a parallel-plate waveguide. Consequently, in a method-of-moment (MoM)-based approach, it suffices to employ the simpler parallel-plate instead of the more complex cavity Green's function, which simplifies the numerical analysis of gap waveguide structures – operating in the stop band – significantly. Furthermore; the MoM matrix-fill time can be reduced, since the translation symmetry of the computed reaction integrals between pairs of basis functions can be exploited.

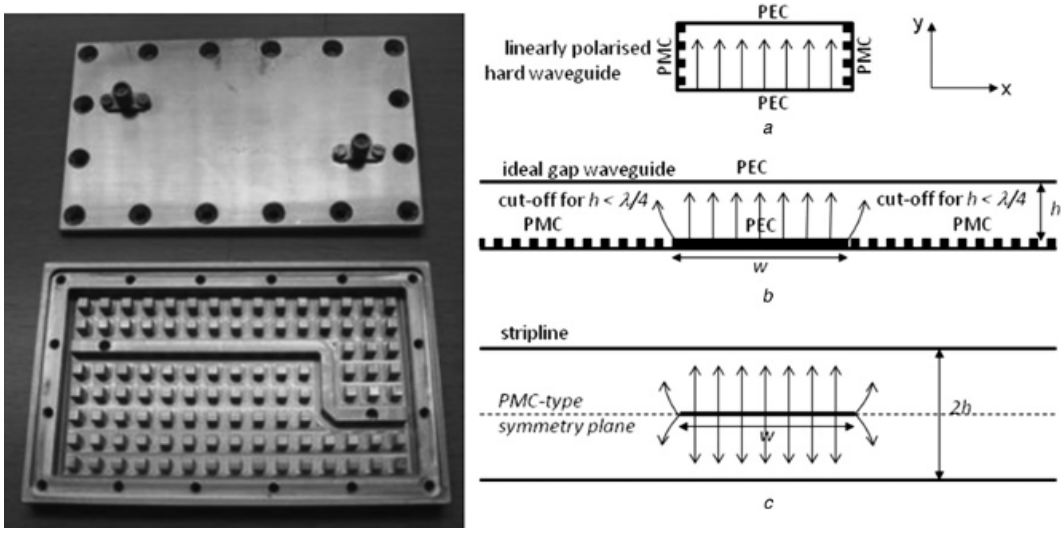

Figure 2.1: Left: ridge gap-waveguide with S-bended ridge. Right: (a) ideal PMC-PEC waveguide boundary conditions for TEM-mode propagation; (b) PMC realization using a bed of nails; (c) stripline transmission line equivalence.

Before formulating the parallel-plate Green's function, we need to recall some of the basic mathematical field formulations. We will use equivalent current sources and the corresponding Green's function to compute the magnetic vector and electric scalar potentials, $\boldsymbol{A}$ and ϕ. The radiated electric and magnetic fields, $\boldsymbol{E}$ and $\boldsymbol{H}$, can be determined accordingly.

In Sec. 2.3 we take a closer look at several possible ways to compute the parallel-plate Green's function summation representing an infinite series of dipole fields. We will consider the convergence of these infinite series as a function of the position of the source and observation point. The spatial domain summation, the spectral domain summation, and

Ewald's summation method are described first, which is followed by the Shanks transformation and the asymptotic form of the Hankel function that are all considered as accelerating methods.

2.2 Fields from Sources in Free Space

Maxwell's equations describe how the electric and magnetic fields, $\boldsymbol{E}(\boldsymbol{r})$ and $\boldsymbol{H}(\boldsymbol{r})$, are related to the volumetric electric current distribution $\boldsymbol{J}(\boldsymbol{r})$ and the electric charge distribution $\rho(\boldsymbol{r})$. These equations have a unique solution, provided that a complete set of boundary conditions is given and that the medium parameters, $\varepsilon(\boldsymbol{r})$ and $\mu(\boldsymbol{r})$ are known, which are the permittivity and permeability of the medium, respectively. In frequency domain, Maxwell's equations for the fields in free space (i.e. $\varepsilon(\boldsymbol{r}) = \varepsilon_0, \mu(\boldsymbol{r}) = \mu_0$) are defined as:

$$\boldsymbol{\nabla} \times \boldsymbol{E} = -j\omega\mu_0 \boldsymbol{H} \tag{2.1a}$$

$$\boldsymbol{\nabla} \times \boldsymbol{H} = \boldsymbol{J} + j\omega\varepsilon_0 \boldsymbol{E} \tag{2.1b}$$

$$\boldsymbol{\nabla} \cdot \boldsymbol{E} = \frac{\rho}{\varepsilon_0} \tag{2.1c}$$

$$\boldsymbol{\nabla} \cdot \boldsymbol{H} = 0. \tag{2.1d}$$

Since $\boldsymbol{H}$ is solenoidal, see Eq. (2.1d), it can be expressed in terms of a magnetic vector potential $\boldsymbol{A}$ as

$$\boldsymbol{\nabla} \cdot \boldsymbol{H} = 0 \Rightarrow \boldsymbol{H} = \boldsymbol{\nabla} \times \boldsymbol{A}. \tag{2.2}$$

Upon using the fact that a vector quantity with zero curl can be described as the gradient of a scalar potential, we have that

$$\boldsymbol{\nabla} \times (\boldsymbol{E} + j\omega\mu_0 \boldsymbol{A}) = 0 \Rightarrow \boldsymbol{E}(\boldsymbol{r}) = -j\omega\mu_0 \boldsymbol{A}(\boldsymbol{r}) - \boldsymbol{\nabla}\phi(\boldsymbol{r}) - \boldsymbol{C} \tag{2.3}$$

where ϕ is an electric scalar potential, yet to be determined, and $\boldsymbol{C} = \boldsymbol{0}$ since $\boldsymbol{E} = \boldsymbol{0}$ at infinity. To define the electric scalar and magnetic vector potentials, we use Maxwell's equations and the vector identity $\boldsymbol{\nabla} \times \boldsymbol{\nabla} \times \boldsymbol{A} = \boldsymbol{\nabla}(\boldsymbol{\nabla} \cdot \boldsymbol{A}) - \boldsymbol{\nabla}^2 \boldsymbol{A}$ to arrive at

$$\boldsymbol{\nabla}\left(\boldsymbol{\nabla} \cdot \boldsymbol{A}\right) - \boldsymbol{\nabla}^2 \boldsymbol{A} = \boldsymbol{J} - j\omega\varepsilon_0 \left(\boldsymbol{\nabla}\phi + j\omega\mu_0 \boldsymbol{A}\right) \tag{2.4}$$

which can be written as

$$\boldsymbol{\nabla}\left(\boldsymbol{\nabla}\cdot\boldsymbol{A}+j\omega\varepsilon_0\phi\right)-\boldsymbol{J}=\boldsymbol{\nabla}^2\boldsymbol{A}+k_0^2\boldsymbol{A} \tag{2.5}$$

where $k_0=\omega\sqrt{\varepsilon_0\mu_0}$ is the free space wavenumber. Next, we choose that

$$\boldsymbol{\nabla}\cdot\boldsymbol{A}=-j\omega\varepsilon_0\phi \tag{2.6}$$

which is known as the Lorenz gauge. By substituting this relation in (2.5), we obtain the inhomogeneous Helmholtz wave equation for the magnetic vector potential:

$$\boldsymbol{\nabla}^2\boldsymbol{A}+k_0^2\boldsymbol{A}=-\boldsymbol{J}. \tag{2.7}$$

Taking the divergence of (2.3), using Maxwell's equations, and (2.6), we obtain the inhomogeneous wave equation for the electric scalar potential ϕ:

$$\boldsymbol{\nabla}^2\phi+k_0^2\phi=-\frac{\rho}{\varepsilon_0}. \tag{2.8}$$

The well-known general solutions for the magnetic vector potential and electric scalar potential in Eqs. (2.7) and (2.8) are given by [6]

$$\boldsymbol{A}\left(\boldsymbol{r}\right)=\iiint_{\mathcal{V}}G\left(\boldsymbol{r}-\boldsymbol{r}'\right)\boldsymbol{J}\left(\boldsymbol{r}'\right)\mathrm{d}V' \tag{2.9a}$$

$$\phi\left(\boldsymbol{r}\right)=\frac{1}{\varepsilon_0}\iiint_{\mathcal{V}}G\left(\boldsymbol{r}-\boldsymbol{r}'\right)\rho\left(\boldsymbol{r}'\right)\mathrm{d}V' \tag{2.9b}$$

where the free space Green's function is defined as

$$G\left(\boldsymbol{r}-\boldsymbol{r}'\right)=\frac{e^{-jk_0|\boldsymbol{r}-\boldsymbol{r}'|}}{4\pi\left|\boldsymbol{r}-\boldsymbol{r}'\right|}. \tag{2.10}$$

Substitution of (2.6) in (2.3), leads to a single potential formulation for the E-field, that is

$$\boldsymbol{E}=\frac{1}{j\omega\varepsilon_0}\left(\boldsymbol{\nabla}\left(\boldsymbol{\nabla}\cdot\boldsymbol{A}\right)+k_0^2\boldsymbol{A}\right). \tag{2.11}$$

Upon applying the current continuity equation $\boldsymbol{\nabla}'\cdot\boldsymbol{J}\left(\boldsymbol{r}'\right)=-j\omega\rho\left(\boldsymbol{r}'\right)$, the electric scalar potential is given as

$$\phi\left(\boldsymbol{r}\right)=\frac{-1}{j\omega\varepsilon_0}\iiint_{\mathcal{V}}G\left(\boldsymbol{r}-\boldsymbol{r}'\right)\boldsymbol{\nabla}'\cdot\boldsymbol{J}\left(\boldsymbol{r}'\right)\mathrm{d}V'. \tag{2.12}$$

In conclusion, if the current $\boldsymbol{J}(\boldsymbol{r})$ is known, the magnetic vector and electric scalar potentials $\boldsymbol{A}$ and ϕ can be computed, after which the radiated $\boldsymbol{E}$ and $\boldsymbol{H}$ fields can be evaluated through (2.11) and (2.2).

2.3 Dyadic Parallel-Plate Green's Function

In the previous section we derived the free-space Green's function, which is the solution for the electromagnetic field of a point source in free space. The free space Green's function is used in this section to derive expressions for the electromagnetic field generated by a point source in a parallel-plate waveguide region: the dyadic parallel-plate Green's function. Since each pin in the parallel-plate waveguide can be considered as an actual radiating element generating the scattered field, it is possible to represent the volumetric current density $\boldsymbol{J}$ supported by each pin by an equivalent surface current density $\boldsymbol{J}_{\mathcal{S}}$, through the application of the surface equivalence principle [6, pp. 329-333]. Each pin can then be replaced by a suitable surface current density, representing the physical current.

We will consider the field of an electric dipole current inside the parallel-plate waveguide as shown in Fig. 2.2(a). The two infinite parallel plates are separated by a distance d along the z-axis. The repeated application of the image principle for an x-polarized or z-polarized dipole [7, p. 184], leads to an infinite summation of electromagnetic fields generated by the resulting images of the original dipole [see Fig. 2.2(c) and (d)].

After defining the free space Green's function as in Eq. (2.10), the dyadic parallel-plate Green's function $\mathbf{G}$ can be defined as

$$\mathbf{G}(\boldsymbol{r}, \boldsymbol{r}') = G_{xx}\hat{\boldsymbol{x}}\hat{\boldsymbol{x}}^T + G_{yy}\hat{\boldsymbol{y}}\hat{\boldsymbol{y}}^T + G_{zz}\hat{\boldsymbol{z}}\hat{\boldsymbol{z}}^T \tag{2.13}$$

where T is the transposition operator. Since G_{xy} is the x-component of $\boldsymbol{A}$ as a result of a y-polarized dipole current, it is herein zero. Note that for free space

$$\mathbf{G} = G\mathbf{I}, \quad \text{where} \quad G\left(\boldsymbol{r} - \boldsymbol{r}'\right) = \frac{e^{-jk_0|\boldsymbol{r}-\boldsymbol{r}'|}}{4\pi\left|\boldsymbol{r} - \boldsymbol{r}'\right|} \tag{2.14}$$

and where $\mathbf{I}$ is the 3×3 identity matrix defined as

$$\mathbf{I} = \hat{\boldsymbol{x}}\hat{\boldsymbol{x}}^T + \hat{\boldsymbol{y}}\hat{\boldsymbol{y}}^T + \hat{\boldsymbol{z}}\hat{\boldsymbol{z}}^T. \tag{2.15}$$

Using the Dyadic Green's function, the magnetic vector potential, $\boldsymbol{A}$, is expressed as

$$\boldsymbol{A} = \iint_{\mathcal{S}} \mathbf{G}\left(\boldsymbol{r}, \boldsymbol{r}'\right) \cdot \boldsymbol{J}_{\mathcal{S}}\left(\boldsymbol{r}'\right) \mathrm{d}S' \tag{2.16}$$

where $\mathcal{S}$ is the support of the equivalent surface current density $\boldsymbol{J}_{\mathcal{S}}$,

$$\boldsymbol{J}_{\mathcal{S}}\left(\boldsymbol{r}'\right) = J_x\hat{\boldsymbol{x}} + J_y\hat{\boldsymbol{y}} + J_z\hat{\boldsymbol{z}} \tag{2.17}$$

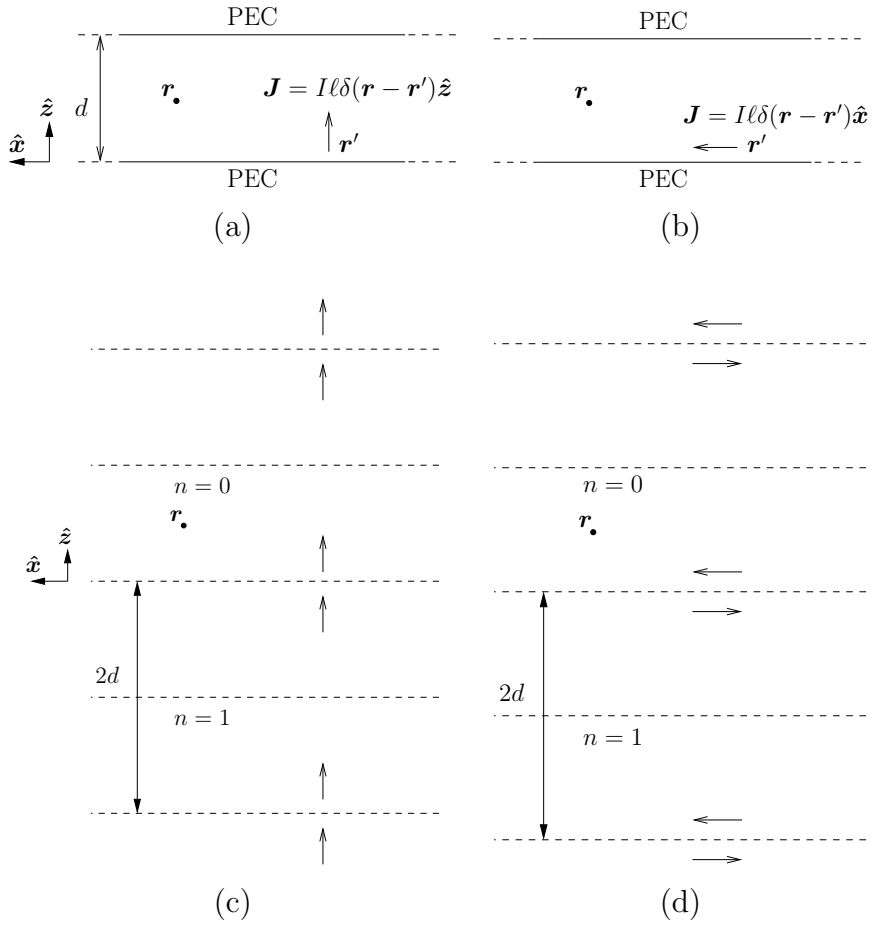

Figure 2.2: (a) z-polarized and (b) x-polarized electric Hertzian dipole currents in between two infinitely large parallel PEC plates separated by a distance d; (c) and (d), the repeated application of the image principle for both dipole polarizations, respectively.

and hence,

$$\mathbf{G}\left(\boldsymbol{r},\boldsymbol{r}'\right)\cdot\boldsymbol{J}_{\mathcal{S}}\left(\boldsymbol{r}'\right)=G_{xx}J_x\hat{\boldsymbol{x}}+G_{yy}J_y\hat{\boldsymbol{y}}+G_{zz}J_z\hat{\boldsymbol{z}}. \tag{2.18}$$

Next, upon using the image principle, the expression for the dyadic Green's function components in the spatial domain can be obtained. As shown in Fig. 2.2, the x component of the Dyadic Green's function due to an x-polarized dipole, G_{xx}, can be written as the sum of two infinite summations corresponding to the images of the original dipole; one array of dipoles polarized along the positive x-axis and the other one along the negative x-axis, each with a dipole separation distance $2d$. Similarly, in case of a z-polarized dipole, G_{zz} is written as the sum of two infinite summations due to the images of a z-polarized dipole, whose images are all polarized along the positive z-axis. In conclusion,

$$\begin{aligned}
G_{xx}&=\sum_{n=-\infty}^{\infty}\frac{e^{-jk_0\sqrt{(x-x')^2+(y-y')^2+(z-z'+2nd)^2}}}{4\pi\sqrt{(x-x')^2+(y-y')^2+(z-z'+2nd)^2}}\\
&\quad-\sum_{n=-\infty}^{\infty}\frac{e^{-jk_0\sqrt{(x-x')^2+(y-y')^2+(z-(d+(d-z'))+2nd)^2}}}{4\pi\sqrt{(x-x')^2+(y-y')^2+(z-(d+(d-z'))+2nd)^2}}\\
G_{yy}&=G_{xx}\\
G_{zz}&=\sum_{n=-\infty}^{\infty}\frac{e^{-jk_0\sqrt{(x-x')^2+(y-y')^2+(z-z'+2nd)^2}}}{4\pi\sqrt{(x-x')^2+(y-y')^2+(z-z'+2nd)^2}}\\
&\quad+\sum_{n=-\infty}^{\infty}\frac{e^{-jk_0\sqrt{(x-x')^2+(y-y')^2+(z-(d+(d-z'))+2nd)^2}}}{4\pi\sqrt{(x-x')^2+(y-y')^2+(z-(d+(d-z'))+2nd)^2}}.
\end{aligned} \tag{2.19}$$

By substituting (2.18) in Eq. (2.16), one can write that

$$\boldsymbol{\nabla}\cdot\boldsymbol{A}=\iint_{\mathcal{S}}\boldsymbol{\nabla}\cdot\left(\mathbf{G}\left(\boldsymbol{r},\boldsymbol{r}'\right)\cdot\boldsymbol{J}_{\mathcal{S}}\left(\boldsymbol{r}'\right)\right)\mathrm{d}S'=\iint_{\mathcal{S}}\partial_x\left(G_{xx}J_x\right)+\partial_y\left(G_{yy}J_y\right)+\partial_z\left(G_{zz}J_z\right)\mathrm{d}S'. \tag{2.20}$$

Also, we have that

$$\partial_x\left(G_{xx}\left(\boldsymbol{r},\boldsymbol{r}'\right)J_x\left(\boldsymbol{r}'\right)\right)=J_x\partial_xG_{xx}=-J_x\partial_{x'}G_{xx}=G_{xx}\partial_{x'}J_x-\partial_{x'}\left(G_{xx}J_x\right) \tag{2.21}$$

and similarly that $\partial_y\left(G_{yy}J_y\right)=G_{yy}\partial_{y'}J_y-\partial_{y'}\left(G_{yy}J_y\right)$. To also rewrite the term $\partial_z\left(G_{zz}J_z\right)$ in a different form, we first note that (2.19) is of the form $G_{xx}=G_{yy}=A-B$, and $G_{zz}=A+B$. This means that $\partial_z\left(G_{zz}J_z\right)=J_z\partial_zG_{zz}=-J_z\partial_{z'}A+J_z\partial_{z'}B$, since $\partial_zA=-\partial_{z'}A$ and $\partial_zB=\partial_{z'}B$. Accordingly, this can be written in expanded form as $\partial_z\left(G_{zz}J_z\right)=A\partial_{z'}J_z-\partial_{z'}\left(AJ_z\right)-B\partial_{z'}J_z+\partial_{z'}\left(BJ_z\right)$, which finally yields

$$\partial_z\left(G_{zz}J_z\right)=\left(A-B\right)\partial_{z'}J_z-\partial_{z'}\left(A-B\right)J_z=G_{xx}\partial_{z'}J_z-\partial_{z'}\left(G_{xx}J_z\right). \tag{2.22}$$

Upon substituting the above results for the partial derivatives in (2.20), and using that $G_{xx} = G_{yy}$, gives

$$\begin{aligned}\boldsymbol{\nabla}\cdot\boldsymbol{A} &= \iint_{\mathcal{S}} \left[G_{xx}\partial_{x'}J_x - \partial_{x'}\left(G_{xx}J_x\right) + G_{xx}\partial_{y'}J_y - \partial_{y'}\left(G_{xx}J_y\right) + G_{xx}\partial_{z'}J_z - \partial_{z'}\left(G_{xx}J_z\right)\right]\mathrm{d}S' \\ &= \iint_{\mathcal{S}} G_{xx}\left(\partial_{x'}J_x + \partial_{y'}J_y + \partial_{z'}J_z\right)\mathrm{d}S' - \iint_{\mathcal{S}} \partial_{x'}\left(G_{xx}J_x\right) + \partial_{y'}\left(G_{xx}J_y\right) + \partial_{z'}\left(G_{xx}J_z\right)\mathrm{d}S' \\ &= \iint_{\mathcal{S}} G_{xx}\boldsymbol{\nabla}'_t\cdot\boldsymbol{J}_{\mathcal{S}}\mathrm{d}S' - \iint_{\mathcal{S}} \boldsymbol{\nabla}'\cdot\left(G_{xx}\mathbf{I}\cdot\boldsymbol{J}_{\mathcal{S}}\right)\mathrm{d}S'. \end{aligned} \tag{2.23}$$

Applying the 2-D version of Gauss' theorem,

$$\iint_{\mathcal{S}} \boldsymbol{\nabla}'\cdot\left(G_{xx}\mathbf{I}\cdot\boldsymbol{J}_{\mathcal{S}}\right)\mathrm{d}S' = \oint_{\partial\mathcal{S}} \left(G_{xx}\mathbf{I}\cdot\boldsymbol{J}_{\mathcal{S}}\right)\cdot\hat{\boldsymbol{\nu}}\mathrm{d}l' \tag{2.24}$$

where $\hat{\boldsymbol{\nu}}$ is the outward pointing unit vector along the edge $\partial\mathcal{S}$, and $\boldsymbol{J}_{\mathcal{S}}\cdot\hat{\boldsymbol{\nu}} = 0$ at $\partial\mathcal{S}$, Eq. (2.23) and then (2.11) and (2.3) are finally evaluated as

$$\begin{aligned}\boldsymbol{E} &= \frac{1}{j\omega\varepsilon_0}\boldsymbol{\nabla}\left(\iint_{\mathcal{S}} G_{xx}\boldsymbol{\nabla}'_t\cdot\boldsymbol{J}_{\mathcal{S}}\mathrm{d}S'\right) + \frac{k_0^2}{j\omega\varepsilon_0}\iint_{\mathcal{S}}\mathbf{G}\cdot\boldsymbol{J}_{\mathcal{S}}\mathrm{d}S' \\ &= \frac{1}{j\omega\varepsilon_0}\boldsymbol{\nabla}\left(\iint_{\mathcal{S}} G_{xx}\boldsymbol{\nabla}'_t\cdot\boldsymbol{J}_{\mathcal{S}}\mathrm{d}S'\right) - j\omega\mu_0\iint_{\mathcal{S}}\mathbf{G}\cdot\boldsymbol{J}_{\mathcal{S}}\mathrm{d}S'. \end{aligned} \tag{2.25}$$

By comparing Eq. (2.3) with Eq. (2.25), the electric scalar potential ϕ is found to be

$$\phi = \frac{-1}{j\omega\varepsilon_0}\iint_{\mathcal{S}} G_{xx}\boldsymbol{\nabla}'_t\cdot\boldsymbol{J}_{\mathcal{S}}\mathrm{d}S'. \tag{2.26}$$

2.3.1 Spatial Summation

Equation (2.19) shows that the dyadic Green's function can be written as an infinite sum of free-space Green's functions. Similarly as defined in (2.14), the Green's function for a homogenous medium, G, is the field radiated by a single point source, which is given by

$$G = \frac{e^{-jkR}}{4\pi R} \tag{2.27}$$

where $k = \omega\sqrt{\mu\varepsilon}$ and R is the distance between the source point $\boldsymbol{r}' = x'\hat{\boldsymbol{x}} + y'\hat{\boldsymbol{y}} + z'\hat{\boldsymbol{z}}$ and observation point $\boldsymbol{r} = x\hat{\boldsymbol{x}} + y\hat{\boldsymbol{y}} + z\hat{\boldsymbol{z}}$, i.e.,

$$R = |\boldsymbol{r} - \boldsymbol{r}'| = \sqrt{(x-x')^2 + (y-y')^2 + (z-z')^2}. \tag{2.28}$$

For 1D periodic infinite arrays of equally strong and equidistant point sources placed along

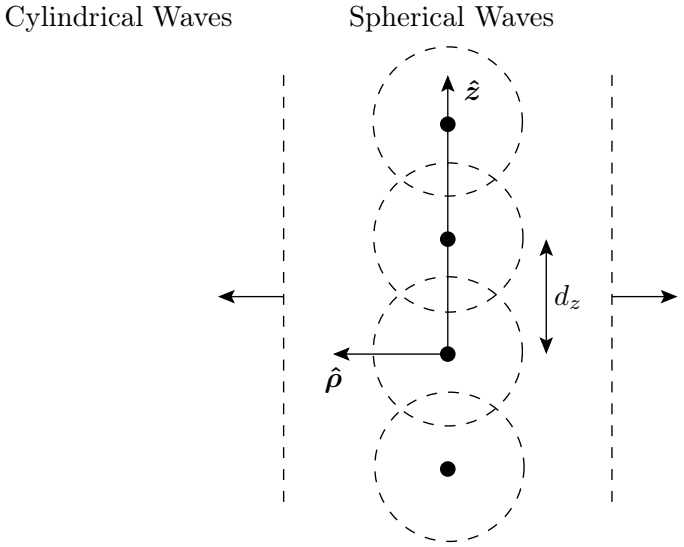

Figure 2.3: Line array of point sources spaced a distance d_z apart, which individually generate spherical waves (observation point near one of the sources), but collectively generate cylindrical waves (observation point away from the sources).

the z-axis, see Fig. 2.3, the periodic Green's function is given by the superposition of the homogenous-space Green's functions as

$$\boxed{G = \frac{1}{4\pi}\sum_{n=-\infty}^{\infty}\frac{e^{-jkR_n}}{R_n}} \tag{2.29}$$

where

$$R_n = \sqrt{x^2 + y^2 + (z - nd_z)^2} = \sqrt{\rho^2 + (z - nd_z)^2} \tag{2.30}$$

where $\rho^2 = x^2 + y^2$ and d_z is the distance between the point sources located along the z-axis. Also, note that $d_z = 2d$ in accordance with one of the infinite summations in (2.19).

If the observation point is close to one of the source points, that source will contribute significantly to the total sum. On the contrary, the fields of the surrounding sources have to travel a certain distance to reach the observation point and are therefore weaker. In that

case, the above sum converges relatively fast. However, if the observation point is taken away from the 1-D array of point sources, more terms start to contribute almost with equal strength to the sum. This effect is enhanced if the distance d_z between the point sources is relatively small. In that case the above sum is slowly convergent. In conclusion, the above spatial summation of the fields is preferred if the observation point is taken close to the line of the sources, relative to the plate distance d or source separation distance d_z.

As a physical motivation one could refer to Fig. 2.4. It can be seen that a cylindrical-wave expansion seems more appropriate for observation points farther out from the source point, while the spherical type of wave expansion is best suited near the source point.

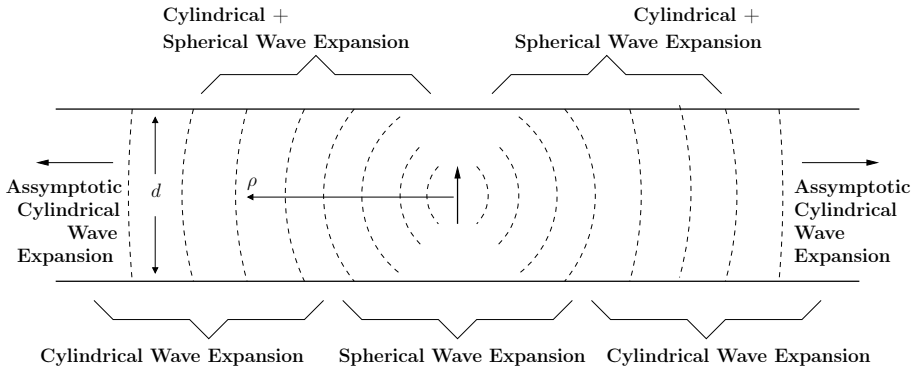

Figure 2.4: An illustration of the radiated field of a z-oriented dipole centered inside a parallel-plate waveguide. Physics shows that a spherical-type of wave expansion is best suited near the source point, while a cylindrical-wave expansion seems more appropriate for observation points farther out and for a small plate distance d. Furthermore, the fields in the intermediate region may be best described by a hybrid method.

2.3.2 Spectral Summation

As explained above, when the fields of more point sources contribute significantly, as in case of observation points away from the 1D array of point source, and/or small d_z, the summation of spectral terms is desired instead. Physically, this can be understood by realizing that each point source emits a spherical wave and, on account of Huygen's principle, all spherical wave fronts together form a cylindrical wave which propagates away from the line array as shown in Fig. 2.4. Accordingly, the field at a distance from the line array is better represented in terms of cylindrical waves.

To derive the spectral summation of the 1-D periodic Green's function, we first use the identity [8]

$$G = \frac{e^{-jkR}}{4\pi R} = \frac{1}{2\pi^{3/2}} \int_0^\infty e^{-R^2\epsilon^2 + \frac{k^2}{4\epsilon^2}} \mathrm{d}\epsilon. \tag{2.31}$$

Assuming that there are losses in the homogenous medium, the complex ambient wavenumber has a negative imaginary part, so that $k = k_r + jk_i = |k|e^{j\phi_k}$ with $\phi_k = \arctan(k_i/k_r) < 0$. Also we have $\epsilon = \epsilon_r + j\epsilon_i = |\epsilon|e^{j\phi_\epsilon}$ with $\phi_\epsilon = \arctan(\epsilon_i/\epsilon_r) < 0$. The convergence of (2.31) is then ensured when [9]

$$\begin{aligned} \frac{3}{4}\pi + \phi_k \geqslant \phi_\epsilon \geqslant \frac{\pi}{4} + \phi_k \quad \text{for} \quad \epsilon \to 0 \\ \frac{\pi}{4} > \phi_\epsilon > \frac{-\pi}{4} \quad \text{for} \quad \epsilon \to \infty \end{aligned} \tag{2.32}$$

hence, for a line array of point sources, we have that

$$\begin{aligned} G &= \frac{1}{2\pi^{3/2}} \sum_{n=-\infty}^{\infty} \int_0^\infty e^{-R_n^2\epsilon^2 + \frac{k^2}{4\epsilon^2}} \mathrm{d}\epsilon = \frac{1}{2\pi^{3/2}} \int_0^\infty \sum_{n=-\infty}^{\infty} e^{-R_n^2\epsilon^2 + \frac{k^2}{4\epsilon^2}} \mathrm{d}\epsilon \\ &= \frac{1}{2\pi^{3/2}} \int_0^\infty \sum_{n=-\infty}^{\infty} e^{-[\rho^2 + (z-nd_z)^2]\epsilon^2 + \frac{k^2}{4\epsilon^2}} \mathrm{d}\epsilon \\ &= \frac{1}{2\pi^{3/2}} \int_0^\infty e^{-\rho^2\epsilon^2 + \frac{k^2}{4\epsilon^2}} \sum_{n=-\infty}^{\infty} e^{-(z-nd_z)^2\epsilon^2} \mathrm{d}\epsilon. \end{aligned} \tag{2.33}$$

Next, the slowly convergent series summation can be transformed into a rapidly converging one through Poisson's summation formula. As derived in Appendix A, we have that

$$\sum_{n=-\infty}^{\infty} e^{-(z-nd_z)^2\epsilon^2} = \frac{\sqrt{\pi}}{d_z\epsilon} \sum_{n=-\infty}^{\infty} e^{-\left(\frac{\pi n}{d_z\epsilon}\right)^2} e^{j\frac{2\pi}{d_z}nz}, \tag{2.34}$$

so that Eq. (2.33) can be written as

$$\begin{aligned} G &= \frac{1}{2\pi d_z} \int_0^\infty e^{-\rho^2\epsilon^2 + \frac{k^2}{4\epsilon^2}} \frac{1}{\epsilon} \sum_{n=-\infty}^{\infty} e^{-\left(\frac{\pi n}{d_z\epsilon}\right)^2} e^{j2\pi\frac{nz}{d_z}} \mathrm{d}\epsilon \\ &= \frac{1}{2\pi d_z} \sum_{n=-\infty}^{\infty} e^{j2\pi\frac{nz}{d_z}} \int_0^\infty \frac{e^{-\rho^2\epsilon^2 + \frac{k^2}{4\epsilon^2} - \left(\frac{\pi n}{d_z\epsilon}\right)^2}}{\epsilon} \mathrm{d}\epsilon. \end{aligned} \tag{2.35}$$

Furthermore, upon defining

$$\alpha_n^2 = k^2 - \left(\frac{2\pi n}{d_z}\right)^2 = k^2 - k_{z,n}^2 \qquad \text{where} \qquad k_{z,n} = \frac{2\pi n}{d_z} \tag{2.36}$$

we have that

$$G = \frac{1}{2\pi d_z} \sum_{n=-\infty}^{\infty} e^{jk_{z,n}z} \int_0^{\infty} \frac{e^{-\rho^2\epsilon^2 + \frac{\alpha_n^2}{4\epsilon^2}}}{\epsilon} \mathrm{d}\epsilon. \tag{2.37}$$

Next, we use the identity [10]

$$\frac{1}{4j} H_0^{(2)}(\alpha_n \rho) = \frac{1}{2\pi} \int_0^{\infty} \frac{e^{-\rho^2\epsilon^2 + \frac{\alpha_n^2}{4\epsilon^2}}}{\epsilon} \mathrm{d}\epsilon \tag{2.38}$$

where $H_0^{(2)}$ is the Hankel function of zero order and second kind. So that the 1D periodic Green's function in the spectral domain is finally written as [11]

$$\boxed{G = \frac{1}{4jd_z} \sum_{n=-\infty}^{\infty} H_0^{(2)}(\alpha_n \rho) e^{jk_{z,n}z}} \tag{2.39}$$

or as

$$\boxed{G = \frac{1}{4jd_z} H_0^{(2)}(k\rho) + \frac{1}{2jd_z} \sum_{n=1}^{\infty} H_0^{(2)}(\alpha_n \rho) \cos(k_{z,n}z)} \tag{2.40}$$

where

$$\alpha_n = \begin{cases} \sqrt{k^2 - k_{z,n}^2}, & k^2 > k_{z,n}^2 \\ -j\sqrt{k_{z,n}^2 - k^2}, & k^2 < k_{z,n}^2 \end{cases} \tag{2.41}$$

Here, α_n is the nth transverse wavenumber, along ρ. For a lossless medium, when $\alpha_n > 0$, the harmonics represent radially outward propagating waves, while $\alpha_n = -j\sqrt{k_{z,n}^2 - k^2}$ corresponds to radially attenuating waves.

Asymptotic form of Hankel function for large arguments

Hankel functions, which are also called Bessel functions of the third kind, are a linear combination of the Bessel function of the first and the second kind. Hankel functions of the second kind are defined as:

$$H_\nu^{(2)}(z) = J_\nu(z) - jY_\nu(z) \qquad \nu = 0, 1, 2, ... \tag{2.42}$$

where $J_\nu(z)$ and $Y_\nu(z)$ are Bessel functions of the first and second kind, respectively. To increase the speed of the numerical computation in (2.39), it is recommended to use the

asymptotic approximation of the functions for large arguments. The asymptotic expansion for the Hankel function of the second kind, when ν is fixed and $|z| \to \infty$, has the following analytical form [12, p. 364]

$$H_\nu^2(z) \sim \left(\frac{2}{\pi z}\right)^{1/2} e^{-j(z-\frac{\nu\pi}{2}-\frac{\pi}{4})} \qquad (-2\pi < \arg(z) < \pi)\,. \tag{2.43}$$

In Chapter 3 the relative error between the zeroth-order Hankel function and its asymptotic form will be examined. It will be concluded, based on an empirical study, for which argument the relative approximation error is in the order of a certain specified accuracy.

2.3.3 Spatial and Spectral Summation (Ewald's Method)

As it has been shown in Fig. 2.4, for a dipole located inside a parallel-plate waveguide, the fields in the intermediate region may be best described by a hybrid mode. It means, rather than summing the fields either in the spatial or spectral domain, one can perform the summation in both the spatial and spectral domains simultaneously using Ewald's summation method. Potentially, Ewald's summation requires to sum only a few spectral and spatial terms, since it exhibits Gaussian decay for the spectral and spatial summation. As in (2.33), the periodic Green's function is first written in integral form, but then split up as [8, 13]

$$\begin{aligned} G &= \frac{1}{2\pi^{3/2}} \sum_{n=-\infty}^{\infty} \int_0^\infty e^{-R_n^2\epsilon^2+\frac{k^2}{4\epsilon^2}}\,\mathrm{d}\epsilon \\ &= \frac{1}{2\pi^{3/2}} \sum_{n=-\infty}^{\infty} \left[\int_0^E e^{-R_n^2\epsilon^2+\frac{k^2}{4\epsilon^2}}\,\mathrm{d}\epsilon + \int_E^\infty e^{-R_n^2\epsilon^2+\frac{k^2}{4\epsilon^2}}\,\mathrm{d}\epsilon\right] \end{aligned} \tag{2.44}$$

where E is the so-called Ewald splitting parameter. Next, we can define that

$$\boxed{G = G_{\text{spatial}} + G_{\text{spectral}}} \tag{2.45}$$

where the spatial part of the Green's function is defined as [9]

$$G_{\text{spatial}} = \frac{1}{2\pi^{3/2}} \sum_{n=-\infty}^{\infty} \int_E^\infty e^{-R_n^2\epsilon^2+\frac{k^2}{4\epsilon^2}}\,\mathrm{d}\epsilon \tag{2.46}$$

and the spectral Green's function as

$$G_{\text{spectral}} = \frac{1}{2\pi^{3/2}} \sum_{n=-\infty}^{\infty} \int_0^E e^{-R_n^2\epsilon^2+\frac{k^2}{4\epsilon^2}}\,\mathrm{d}\epsilon. \tag{2.47}$$

Since the convergence of the Ewald summation depends on the convergence of both the spectral and the spatial parts, the path of integration is the same as given in (2.32), except that the point $\epsilon = E$ must be included along the integration contour. The path of integration is shown in Fig. 2.5.

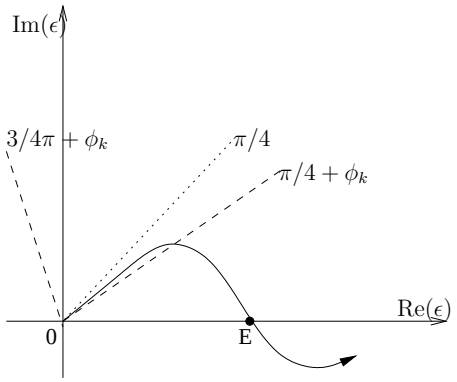

Figure 2.5: The region of convergence of (2.47) which is also given in (2.32).

With reference to (2.46), let us first evaluate

$$I = \frac{1}{2\pi^{3/2}} \int_E^\infty e^{-R_n^2\epsilon^2 + \frac{k^2}{4\epsilon^2}} \mathrm{d}\epsilon. \tag{2.48}$$

By making use of the substitution

$$u = R_n\epsilon + j\frac{k}{2\epsilon} \tag{2.49}$$

we will choose that

$$\epsilon = \frac{1}{2R_n}\left(u + \sqrt{u^2 - j2kR_n}\right), \qquad \text{so that} \qquad \mathrm{d}\epsilon = \frac{1}{2R_n}\left(1 + \frac{u}{\sqrt{u^2 - j2kR_n}}\right)\mathrm{d}u \tag{2.50}$$

which yields

$$\begin{aligned} I &= \frac{1}{4\pi^{3/2}}\frac{e^{jkR_n}}{R_n}\int_{R_nE+\frac{jk}{2E}}^\infty e^{-u^2}\left(1 + \frac{u}{\sqrt{u^2 - j2kR_n}}\right)\mathrm{d}u \\ &= \frac{1}{4\pi^{3/2}}\frac{e^{jkR_n}}{R_n}\int_{R_nE+\frac{jk}{2E}}^\infty e^{-u^2}\mathrm{d}u + \frac{1}{4\pi^{3/2}}\frac{e^{jkR_n}}{R_n}\int_{R_nE+\frac{jk}{2E}}^\infty e^{-u^2}\left(\frac{u}{\sqrt{u^2 - j2kR_n}}\right)\mathrm{d}u. \end{aligned} \tag{2.51}$$

Next, since the complementary error function is defined as [12, p. 297]

$$\operatorname{erfc}(z) = \frac{2}{\sqrt{\pi}} \int_z^\infty e^{-t^2} \mathrm{d}t \tag{2.52}$$

the first term on the right-hand side of (2.51) can directly be evaluated as

$$\frac{1}{4\pi^{3/2}} \frac{e^{jkR_n}}{R_n} \int_{R_n E + \frac{jk}{2E}}^\infty e^{-u^2} \mathrm{d}u = \frac{1}{8\pi} \frac{e^{jkR_n}}{R_n} \operatorname{erfc}\left(R_n E + \frac{jk}{2E} \right). \tag{2.53}$$

The second term on the right-hand side of (2.51) can be evaluated in a similar manner. Using the change of variable

$$w^2 = u^2 - j2kR_n \tag{2.54}$$

we choose that

$$u = \sqrt{w^2 + j2kR_n}, \qquad \text{so that} \qquad \mathrm{d}u = \frac{w}{\sqrt{w^2 + 2jkR_n}} \mathrm{d}w \tag{2.55}$$

which yields

$$\begin{aligned} \frac{1}{4\pi^{3/2}} \frac{e^{jkR_n}}{R_n} \int_{R_n E + \frac{jk}{2E}}^\infty e^{-u^2} \left(\frac{u}{\sqrt{u^2 - j2kR_n}} \right) \mathrm{d}u &= \frac{1}{4\pi^{3/2}} \frac{e^{-jkR_n}}{R_n} \int_{R_n E - \frac{jk}{2E}}^\infty e^{-w^2} \mathrm{d}w \\ &= \frac{1}{8\pi} \frac{e^{-jkR_n}}{R_n} \operatorname{erfc}\left(R_n E - \frac{jk}{2E} \right). \end{aligned} \tag{2.56}$$

Hence, Eq. (2.46) can therefore be evaluated as

$$\boxed{G_{\text{spatial}} = \frac{1}{8\pi} \sum_{n=-\infty}^{\infty} \frac{1}{R_n} \left[e^{jkR_n} \operatorname{erfc}\left(R_n E + \frac{jk}{2E} \right) + e^{-jkR_n} \operatorname{erfc}\left(R_n E - \frac{jk}{2E} \right) \right]} \tag{2.57}$$

where the complementary error function is defined in (2.52). This function is approximated by $\operatorname{erfc}(z) \sim e^{-z^2}/(\sqrt{\pi} z)$ for large arguments [12, pp. 297-304], which shows the Gaussian exponential convergence of (2.57).

To evaluate G_{spectral}, we can follow the procedure up to (2.37), except that the integration limits are different, i.e.,

$$G_{\text{spectral}} = \frac{1}{2\pi d_z} \sum_{n=-\infty}^{\infty} e^{jk_{z,n} z} \int_0^E \frac{e^{-\rho^2 \epsilon^2 + \frac{\alpha_n^2}{4\epsilon^2}}}{\epsilon} \mathrm{d}\epsilon. \tag{2.58}$$

Due to the limited integration limit, Eq. (2.58) is not the integral representation of the Hankel function, although it does represent a spectrum which is close to the cylindrical wave spectrum. Upon performing the change of variable $u = \epsilon^2$, we have that $\mathrm{d}u = 2\epsilon\mathrm{d}\epsilon$ and obtain (see also [10] which uses a similar approach)

$$L = \frac{1}{4\pi d_z} \sum_{n=-\infty}^{\infty} e^{jk_{z,n}z} \int_0^{E^2} \frac{e^{-\rho^2 u + \frac{\alpha_n^2}{4u}}}{u} \mathrm{d}u. \tag{2.59}$$

Next, we utilize the Taylor expansion

$$e^{-\rho^2 u} = \sum_{q=0}^{\infty} \frac{(j\rho)^{2q}}{q!} u^q. \tag{2.60}$$

Accordingly, we can write (2.59) as

$$L = \frac{1}{4\pi d_z} \sum_{n=-\infty}^{\infty} e^{jk_{z,n}z} \sum_{q=0}^{\infty} \frac{(j\rho)^{2q}}{q!} \int_0^{E^2} u^{q-1} e^{\frac{\alpha_n^2}{4u}} \mathrm{d}u. \tag{2.61}$$

Changing to the variable $t = E^2/u$, where $\mathrm{d}u = \frac{-E^2}{t^2}\mathrm{d}t$, yields

$$L = \frac{1}{4\pi d_z} \sum_{n=-\infty}^{\infty} e^{jk_{z,n}z} \sum_{q=0}^{\infty} \frac{(j\rho E)^{2q}}{q!} \int_1^{\infty} \frac{e^{\frac{\alpha_n^2 t}{4E^2}}}{t^{q+1}} \mathrm{d}t. \tag{2.62}$$

Finally, with the qth order exponential integral defined as [12, p. 228]

$$\mathcal{E}_q(z) = \int_1^{\infty} \frac{e^{-zt}}{t^q} \mathrm{d}t \qquad (q = 0, 1, ...; \mathfrak{Re}\{z\} > 0) \tag{2.63}$$

we arrive at [9]

$$\boxed{G_{\text{spectral}} = \frac{1}{4\pi d_z} \sum_{n=-\infty}^{\infty} e^{jk_{z,n}z} \sum_{q=0}^{\infty} \frac{1}{q!} (j\rho E)^{2q} \mathcal{E}_{q+1}\left(\frac{-\alpha_n^2}{4E^2}\right)} \tag{2.64}$$

where $\mathfrak{Re}\{\frac{-\alpha_n^2}{4E^2}\} > 0$. We note the property that [12, p. 229]

$$\mathcal{E}_{q+1}(z) = \frac{1}{q}[e^{-z} - z\mathcal{E}_q(z)] \qquad (n = 1, 2, ...) \tag{2.65}$$

which is useful for the numerical evaluation of (2.64). Hence, only the exponential integral $\mathcal{E}_1(z)$ needs to be evaluated numerically. This integral is defined as [12, p. 228]

$$\mathcal{E}_1(z) = \int_z^{\infty} \frac{e^{-t}}{t} \mathrm{d}t \qquad |\arg z| < \pi \tag{2.66}$$

where a branch cut exists along the negative real axis. We should note that in the absence of losses, all propagating waves have $\alpha_n^2 = k^2 - k_{z,n}^2 > 0$, which causes the argument of the exponential integral in Eq. (2.64) to become negative. To resolve this ambiguous condition, small ambient losses can be considered so that $\mathfrak{Im}(-\alpha_n^2) > 0$. In case of lossless media, evaluation of $\mathcal{E}_{q+1}(z)$ can be done by using the formula $\mathcal{E}_1(-z + j0^+) = -\mathrm{Ei}(z) - j\pi$, [12, p. 228], with

$$\mathrm{Ei}(z) = -\mathrm{P.V.} \int_{-z}^{\infty} \frac{e^{-t}}{t} \mathrm{d}t \qquad z > 0 \tag{2.67}$$

where P.V. denotes the Cauchy principal-value integration [12, pp. 228-235]. The exponential integral for small arguments can be evaluated as

$$\mathrm{Ei}(z) = \gamma + \ln z + \sum_{n=1}^{\infty} z^n/(nn!) \tag{2.68}$$

for $z > 0$, where $\gamma \approx 0.57721566$ is the Euler constant. Once $\mathcal{E}_1(-z + j0^+)$ is obtained, $\mathcal{E}_{q+1}(-z + j0^+)$ follows directly from (2.65).

Ewald's splitting parameter extraction

To obtain an optimum value for the Ewald splitting parameter $E = E_0$, we first examine the convergence of G_{spectral} and G_{spatial} given in (2.64) and (2.57), respectively, for large n. The complementary error function for large arguments behaves as

$$\mathrm{erfc}(z) \sim e^{-z^2}/(\sqrt{\pi}z) \tag{2.69}$$

so that, in the spatial summation,

$$\begin{aligned} e^{-(R_n E \pm \frac{jk}{2E})^2} &= e^{-(R_n^2 E^2 \pm jkR_n - \frac{k^2}{4E^2})} \\ &= e^{-R_n^2 E^2 (1 \pm \frac{jk}{R_n E^2} - \frac{k^2}{4R_n^2 E^4})} \\ &\sim e^{-R_n^2 E^2} \qquad \text{for large value of } n. \end{aligned} \tag{2.70}$$

In the spectral summation, the exponential integral behaves for large arguments as

$$\mathcal{E}_{q+1}(z) \sim e^{-z}/z \tag{2.71}$$

which leads to the expression $\exp(\frac{\alpha_n^2}{4E^2})$ for large values of n. The optimum splitting parameter, E_0, can be found by setting the rates of decay equal to each other, which means

that $\alpha_n^2 = -4R_n^2 E_0^4$, so that

$$\begin{aligned} E_0^4 &= -\frac{\alpha_n^2}{4R_n^2} \\ &= -\frac{k^2 - \left(\frac{2\pi n}{d_z}\right)^2}{4(\rho^2 + (z - nd_z)^2)} \\ &= \frac{\left(\frac{n\pi}{d_z}\right)^2 - \frac{k^2}{4}}{\rho^2 + (z - nd_z)^2} \\ &= \frac{\frac{\pi^2}{d_z^2} n^2 - \frac{k^2}{4}}{d_z^2 n^2 - 2(zd_z)n + \rho^2 + z^2} \\ &= \frac{\frac{\pi^2}{d_z^2}}{d_z^2} = \frac{\pi^2}{d_z^4} \qquad \text{as} \quad n \to \infty \end{aligned} \tag{2.72}$$

and this gives

$$E_0 = \frac{\sqrt{\pi}}{d_z}. \tag{2.73}$$

At high frequencies, some of the terms in the Ewald formulation, i.e. those that arise from the complementary error functions and the exponential integral in (2.57) and (2.64), can become very large. These terms are primarily due to the propagating terms, such as $n = 0$ in the spatial sum G_{spatial} in Eq. (2.57). Also the exponential integrals can lead to numerical instabilities when they have very large arguments. The large terms in the Ewald representation almost cancel each other, which causes loss of accuracy and overflow errors. This numerical instability at high frequencies or large inter-element spacings d_z leads to another choice of the Ewald splitting parameter, rather than the optimum one given in (2.73). In [10] it is suggested to increase the splitting parameter for higher frequencies to improve the numerical inaccuracies. The presented algorithm in [10] is applied to periodic structures when the observation point is near the array of sources.

2.4 Shanks transformation

To compute the radiation from periodic structures, we could evaluate the spatial Green's function series in (2.29). However, this series alone is usually slowly convergent for large ρ and small d. This slow convergence would lead to long computation times when the method

of moments is applied. To reduce this time, we have to improve the convergence rate of the spatial Green's function series. The Shanks transformation is one of the accelerating method which is capable of improving the convergence of single or doubly periodic Green's functions considerably [14]. Although other methods have been proposed in [15] where the Shanks transformation is used in combination with Kummer's transformation or Poisson's transformation, repeated application of Shanks transformation alone can already have great effect in reducing the Green's function evaluation time (note that Poisson's summation formula is discussed in more detail in Appendix A).

Considering the following summation to be evaluated

$$S = \sum_{m=-\infty}^{\infty} f(m) \tag{2.74}$$

and defining the partial sum S_n as

$$S_n = \sum_{m=-n}^{n} f(m) \tag{2.75}$$

a new sequence is formed as $\{S_n\}_{n\in\mathbb{N}}$ which approaches to S when $n \to \infty$. The motivation of the Shanks transformation is based on the assumption that the partial sum S_n, for large values of n, behaves as

$$S_n = S + \alpha q^n \tag{2.76}$$

where $|q| < 1$ causes the sequence to converge to S when $n \to \infty$. Based on Eq. (2.76) the partial sums for $n-1$, n, and $n+1$, for large n are

$$S_{n-1} = S + \alpha q^{n-1}, \quad S_n = S + \alpha q^n \quad \text{and} \quad S_{n+1} = S + \alpha q^{n+1}. \tag{2.77}$$

Solving these equation for the unknown S leads to the Shanks transformation T of the sequence S_n, which is computed as [16]

$$T(S_n) = \frac{S_{n+1}S_{n-1} - S_n^2}{S_{n+1} - 2S_n + S_{n-1}}. \tag{2.78}$$

The new sequence of $T(S_n)$ converges faster than the original sequence S_n. To realize an even faster convergence, repeated application of the Shanks transform can be applied, that is, $T^2(S_n) = T(T(S_n))$. Also, it is shown that the Shanks transformation can be implemented by the recursion relation [17]

$$e_{s+1}(S_n) = e_{s-1}(S_{n+1}) + \frac{1}{e_s(S_{n+1}) - e_s(S_n)} \qquad s = 1, 2, 3, ... \tag{2.79}$$

where

$$e_0(S_n) = S_n \quad \text{and} \quad e_1(S_n) = \frac{1}{e_0\left(S_{n+1}\right) - e_0(S_n)}. \tag{2.80}$$

The even order terms $e_{2p}(S_n)$ are equal to the result of the pth application of the Shanks transformation of the partial sum S_n approximating the sum S. To terminate the Shanks transformation, a condition can be defined as

$$\left| \frac{e_{2p+2}(S_{n-1}) - e_{2p}(S_n)}{e_{2p+2}(S_{n-1})} \right| \leqslant \epsilon_c. \tag{2.81}$$

Here, ϵ_c is the convergence factor. The criterion in (2.81) has to be satisfied for three successive values of n for the Shanks transformation to terminate.

2.5 Conclusions

In this chapter different approaches for the fast computation of the dyadic parallel-plate Green's function have been described. We derived the Green's function formulation for an infinitely large parallel plate structure in the spatial domain by considering a point source within the parallel plate region after which the image principle was invoked to obtain an infinite 1-D array of point sources in free space. The obtained formulation in the spatial domain is then transformed to the spectral domain by application of the Poisson summation formula, which is useful for large observation and small plate separation distances. Also, to increase the convergence rate of the series summation in the near field of the point source, the Ewald method is presented which decomposes the spatial Green's function series into the two parts G_{spectral} and G_{spatial}, which are both dependent on a splitting parameter E, used to control the convergence rate. This splitting parameter has been extracted by equating the asymptotic convergence rates of both G_{spectral} and G_{spatial} in the Ewald summation. Finally, the Shanks transformation is described to increase the convergence rate of the spatial summation in order to reduce the evaluation time of the infinite Green's function series summation. Also, for the spectral summation, the Hankel function is replaced by its asymptotic form when the argument of the Hankel function becomes large. It is pointed out that the latter form of acceleration is applicable in the spectral summation method, while the Shanks transformation is mostly applied to accelerate the slowly convergent spatial domain series.

Chapter 3

Green's Function Analysis Results

In this chapter, the computational methods described in Chapter 2 for the numerical evaluation of the dyadic parallel-plate Green's function are examined in more detail. Results are provided showing the convergence rate and evaluation time for each of the methods. These results are useful for the appropriate selection of a specific summation method in order to increase the computational efficiency of the parallel-plate Green's function evaluation.

3.1 Introduction

In the previous chapter we described the dyadic parallel-plate Green's function for a line array of point sources. Several computational methods have been described in order to evaluate the resulting Green's function in an efficient manner. Starting from the spatial domain representation, the Green's function has been transformed to the spectral domain. The former is efficient for observation distances near the source point and for large plate separation distances, while the latter spectral approach converges rapidly for far observation points and small plate separation distances. Furthermore, the Ewald method is described as an alternative way to represent the Green's function summation in the near-field region. The Shanks transformation and the asymptotic form of the Hankel function can be applied to accelerate the spatial and spectral Green's function evaluation, respectively.

Given a desired specified error, element spacing, and distance to the line array to evaluate

the Green's function, our objective is to find the number of required summation terms and the corresponding evaluation time for the different methods alluded to above. A quantitative comparison regarding the efficiency of the methods can be performed with relative ease for the spatial and spectral summation method, however, for the Ewald summation more parameters have to be considered, such as the optimal Ewald splitting parameter in (2.73), which is itself dependent upon the element spacing. Below we examine the differences in accuracy, evaluation time and the minimum number of terms for computing the dyadic Green's function for several positions of the observation points to the line array of sources, as well as for different inter-element spacings.

3.2 Numerical Examples

The numerical examples that are presented in this chapter have been computed in Matlab (operating system: Windows Vista Business). The computations have been carried out by a 2.3 GHZ AMD Athlon(tm) 64 X2 Dual Core Processor 4400+, equipped with 4 GB of RAM memory.

3.2.1 Evaluation of the spatial and spectral summation

The minimum number of required terms needed in the spatial and spectral summations to achieve convergence can be examined with the aid of Fig. 3.1. The total number of terms N is increased, while the dipole separation distance is fixed at $d_z = 3/8\lambda$. Clearly, the spectral summation has (visually) converged already for $N = 3$, while the spatial summation needs at least 201 terms to achieve a similar result. If the observation point approaches the line array, the accuracy of the spatial summation increases, as expected. These qualitative observations are in agreement with the physics-based reasoning performed earlier for Fig. 2.4.

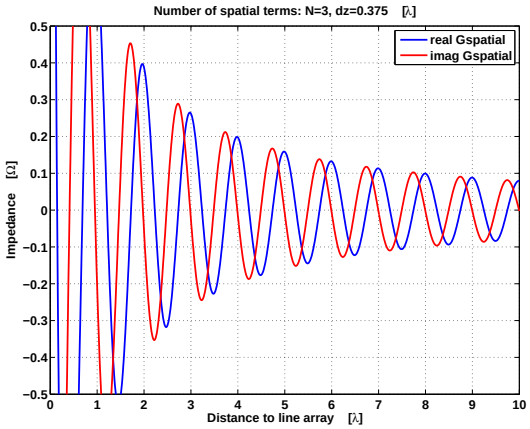

(a)

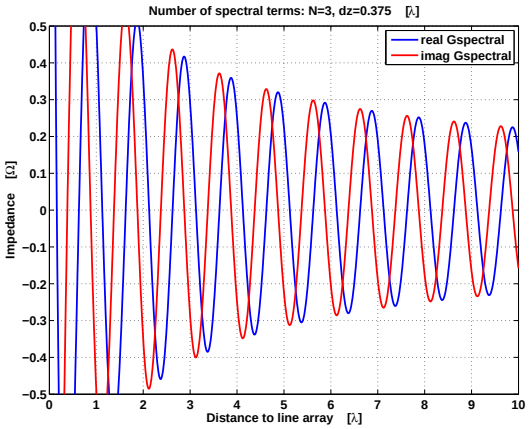

(b)

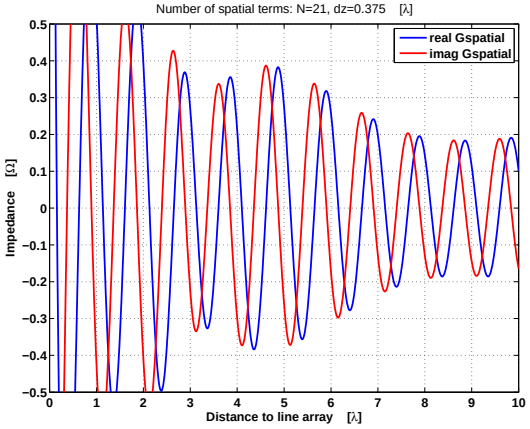

(c)

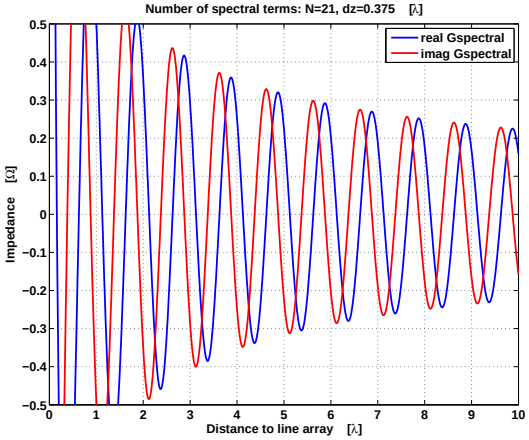

(d)

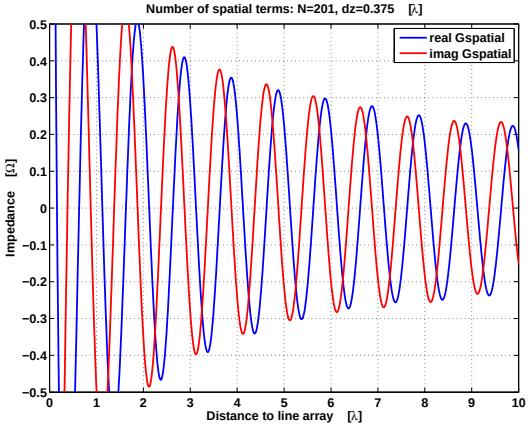

(e)

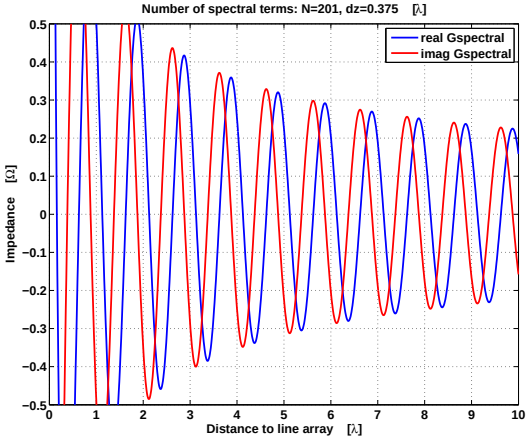

(f)

Figure 3.1: On the left: evaluation of the spatial summation, Eq. (2.29). On the right: evaluation of the spectral summation, Eq. (2.39). The number of the terms N is increased, $d_z = 3/8\lambda$.

3.2.2 Relative spectral summation error as a function of element spacing d_z, and radial observation distance ρ

The convergence rate of the spectral summation can be examined through the relative error defined as

$$\text{Error} = \sqrt{\frac{|G^{\text{exact}} - G^{\text{spectral}}|^2}{|G^{\text{exact}}|^2}} \times 100\% \tag{3.1}$$

where G^{exact} constitutes the reference solution, which is taken to be the spectral or spatial Green's function, evaluated for a sufficiently large number of terms. In Fig. 3.2 one can observe that the relative error for the spectral summation is increasing for a larger plate distance d_z, while it is decreasing for larger ρ. This is in agreement with the physical interpretation given earlier for Fig. 2.4. Also, for small values of ρ, i.e. when it tends to zero, one encounters a singularity in the Hankel function, which clearly exacerbates the convergence rate.

To have a more quantitative comparison of the different methods, the minimum required series evaluation time is also computed to reach a specified accuracy for different values of d_z and ρ. Considering T_0^{Spectral} as the required time to evaluate a single series term in the spectral summation, and N^{Spectral} as the number of spectral terms needed to reach the relative accuracy ϵ, the total evaluation time can be written as

$$T^{\text{Spectral}} = T_0^{\text{Spectral}} N^{\text{Spectral}}(\epsilon, d_z, \rho). \tag{3.2}$$

The results for the total evaluation time, T^{Spectral}, are also visualized in Fig. 3.2, where $T_0^{\text{Spectral}} = 0.14882$ sec.

3.2.3 Relative spatial summation and Shanks transformation error as a function of element spacing d_z, and radial observation distance ρ

The relative error and the total evaluation time of the Shanks-accelerated spatial summation is computed in an analogous manner as done for the spectral summation. As is shown in Fig. 3.3, the change in the relative error for different values of d_z is not very large as compared to the change in case of the spectral summation, but we can observe that the

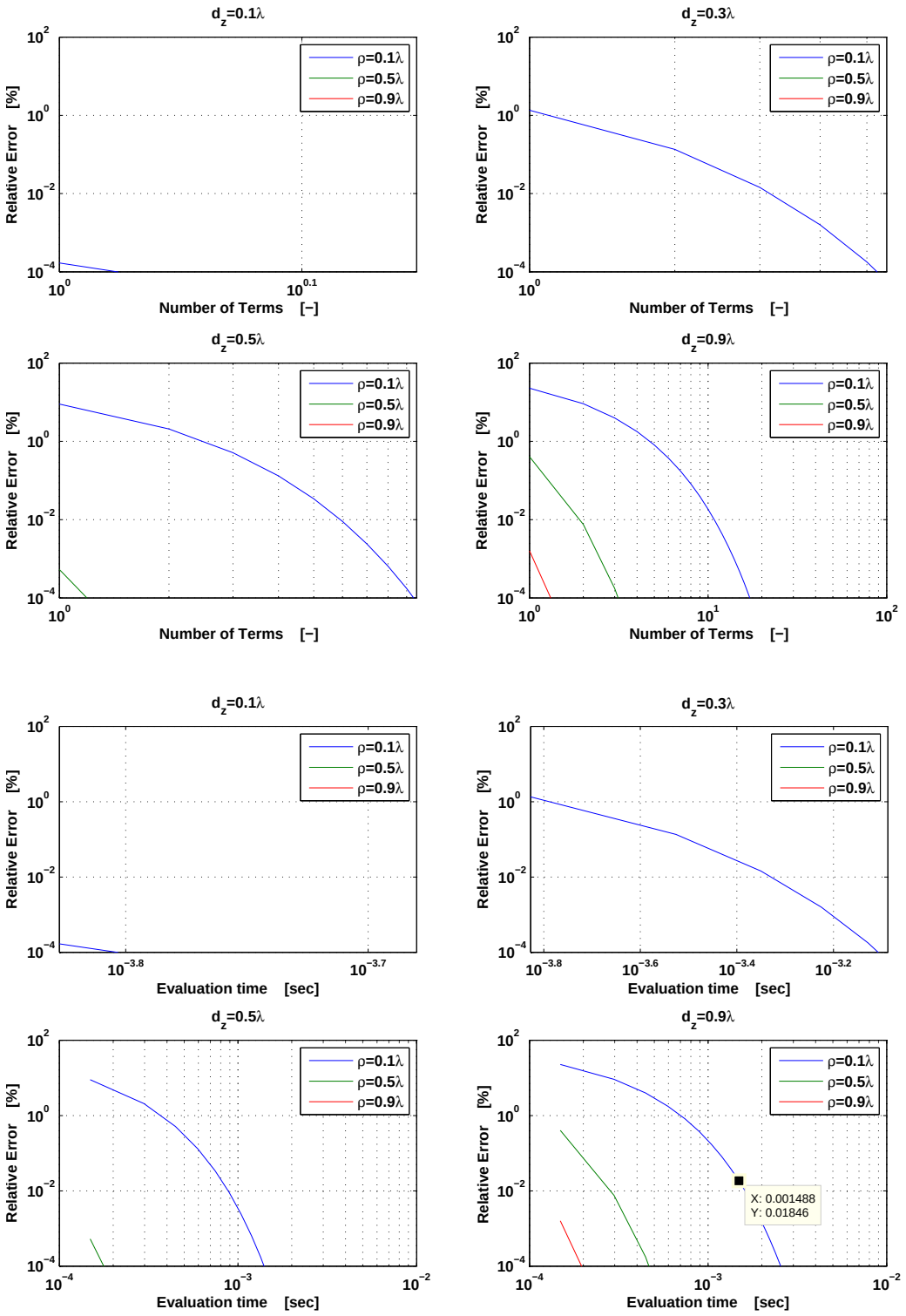

Figure 3.2: Relative error for the spectral summation as a function of the number of terms and evaluation time.

relative error for both the spatial and Shanks-accelerated spatial summation is increasing for larger ρ. It is clear from Fig. 3.3 that the application of the Shanks transformation relative to a straightforward spatial summation leads to a lower number of series terms to reach a specified error. This effect is enhanced after repeated application of the Shanks transformation. The total series evaluation time for the spatial summation is computed as in (3.2), albeit that for the Shanks accelerated spatial summation the following relation applies:

$$T^{\text{Shanks},n} = T_0^{\text{Spatial}}[N^{\text{Shanks},n}(\epsilon, d_z, \rho) - n] + T_{\text{e}}^{\text{Shanks},n} \tag{3.3}$$

where $T_{\text{e}}^{\text{Shanks,n}}$ is the infinite-sum extrapolation time needed after summing $N - n$ spatial terms. Fig. 3.3 depicts the variation of the relative error versus the evaluation time for the Shanks transformations of order 1 to 4, together with the spatial summation for $\rho = .1\lambda$ and $\rho = .5\lambda$. It should be noted that the evaluation time for different order of Shanks transformations depends on the required accuracy. For example, for the desired accuracy of 0.01 percent, the evaluation time for the Shanks transformation of order 2 and 3 is less than the Shanks transformation of order 4.

3.2.4 Relative Ewald summation error as a function of element spacing d_z, and radial observation distance ρ

The convergence error of the Ewald sum is evaluated in the same way as mentioned in (3.1), where G^{exact} is the spectral summation evaluated for a sufficiently large number of terms to reach the required accuracy (i.e. the reference solution). The relative error as a function of the required number of terms is shown in Fig. 3.4, where the splitting parameter is the optimum one as derived in (2.73), i.e. $E_0 = \frac{\sqrt{\pi}}{d_z}$, for four element spacings ranging from 0 to λ. As it is mentioned in Sec.2.3.3, this choice of Ewald splitting parameter does generally not lead to a stable scheme as we may encounter accuracy problems for larger element spacings and at high frequencies. The number of q terms in (2.64) is set to $Q = 20$ which is large enough, so that the convergence rate is only related to the number of terms N. One observes in Fig. 3.4 that the relative error is not further decreased by increasing the number of terms N, primarily due to the finite numerical accuracy with which the exponential integral $E_1(z)$ and error functions in G_{spectral} and G_{spatial} can be evaluated, respectively. The other factor we can compute for the Ewald summation is the evaluation time for one term, $T_0^{\text{Ewald}} = 2.5144$ sec, which is much larger than $T_0^{\text{spectral}} = 0.14882$ sec.

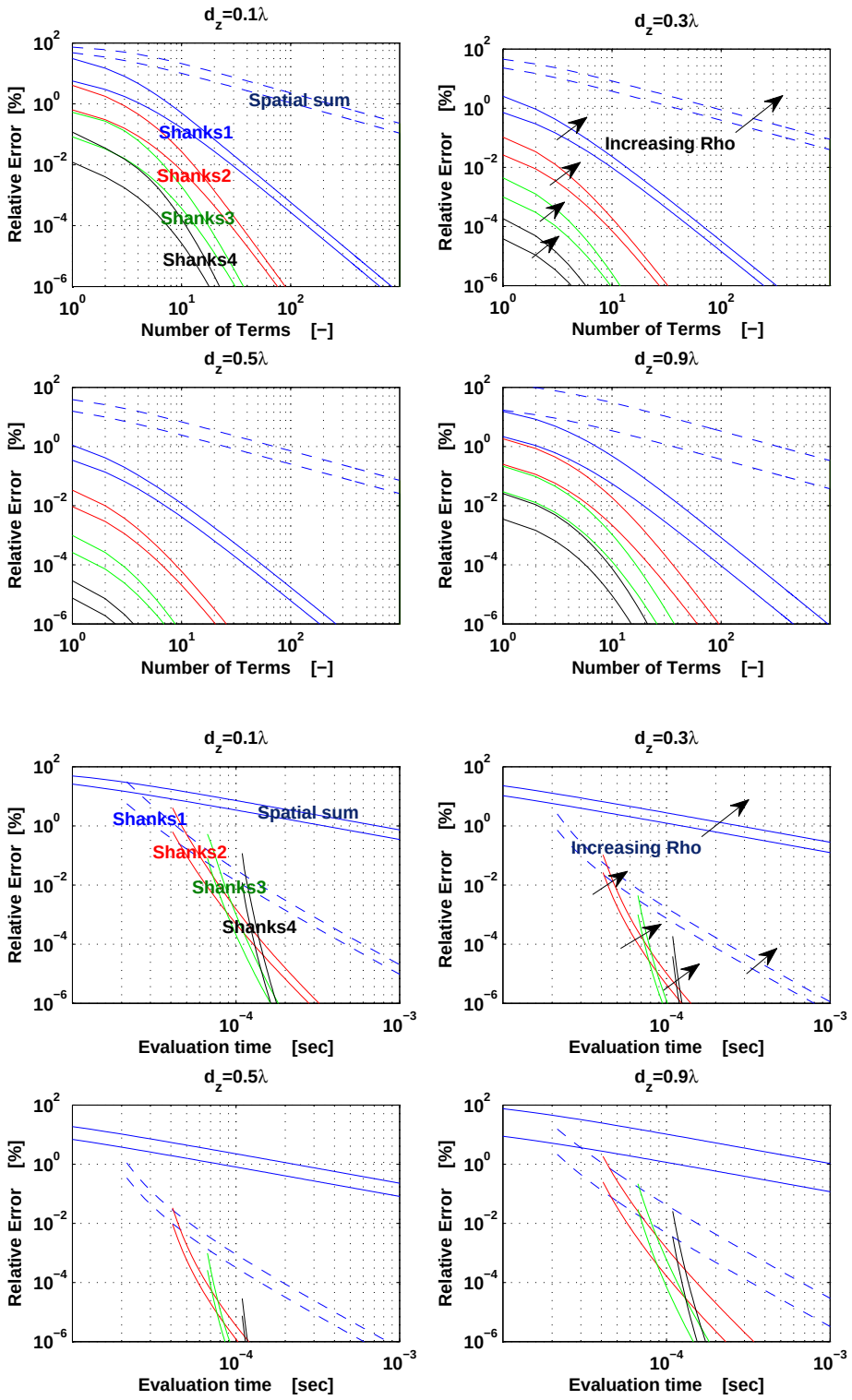

Figure 3.3: Relative error for the spatial summation and the Shanks transformation as a function of the number of terms and the total series evaluation time.

Also, an acceptable relative error is obtained for different plate distances when the observation points are at $\rho = 0.01\lambda$, or 0.1λ, while for the observation points $\rho = 0.001\lambda$, and 0.5λ the obtained result is either unstable or does not reach the desired accuracy level. To avoid the stability problem of Ewald's method, another method is considered based on Kummer's transformation in [18].

With reference to the series evaluation time for a single term in (3.2) and (3.3), the computation times for evaluating only one spatial, spectral, or Ewald term are shown in table 3.1. To minimize estimation error, we have computed the *average* evaluation time for a sufficiently large number of realizations.

Table 3.1: Series evaluation time for a single term as used in (3.2) and (3.3).

T_0^{spatial} [sec]	T_0^{spectral} [sec]	T_0^{Ewald} [sec]
3.1843×10^{-6}	1.4882×10^{-4}	2.5144×10^{-3}

3.2.5 Asymptotic form of the Hankel function for large arguments $|\rho\alpha_n|$

The asymptotic expansion for the Hankel function of the second kind, when ν is 0 and $|z| \to \infty$, has the following analytical form [12, pp.364]

$$H_0^2(z) \sim \left(\frac{2}{\pi z}\right)^{1/2} e^{-j(z-\frac{\pi}{4})} \qquad (-2\pi < \arg(z) < \pi)\,. \tag{3.4}$$

It is pointed out that the Hankel function argument $\alpha_n\rho$, is always real or negative imaginary for lossless media otherwise. Considering the relative error between the actual Hankel function and its asymptotic expansion (as shown in Fig. 3.5; top), it can be verified that the maximum of the relative error occurs when the argument of the Hankel function is completely real. An approximate analytical function for the relative error between the asymptotic expansion of the Hankel function and the actual Hankel function can then be found. By synthesizing the worst-case approximation error with a 6th order polynomial, a good empirical approximation of this relative error ϵ (in decibels) is then found to be

$$\begin{aligned}\epsilon(|z|) = {} & 0.0001 \times |z|^6 - 0.0022 \times |z|^5 + 0.0295 \times |z|^4 - 0.1939 \times |z|^3 \\ & + 0.6754 \times |z|^2 - 1.3173 \times |z| - 0.1685 + .05 \quad \text{for} \quad 0 \le |z| \le 10.\end{aligned} \tag{3.5}$$

If the approximation error computed by our approximate function exceeds a maximum specified error level, then the regular Hankel function should be applied, instead of its asymptotically expanded form.

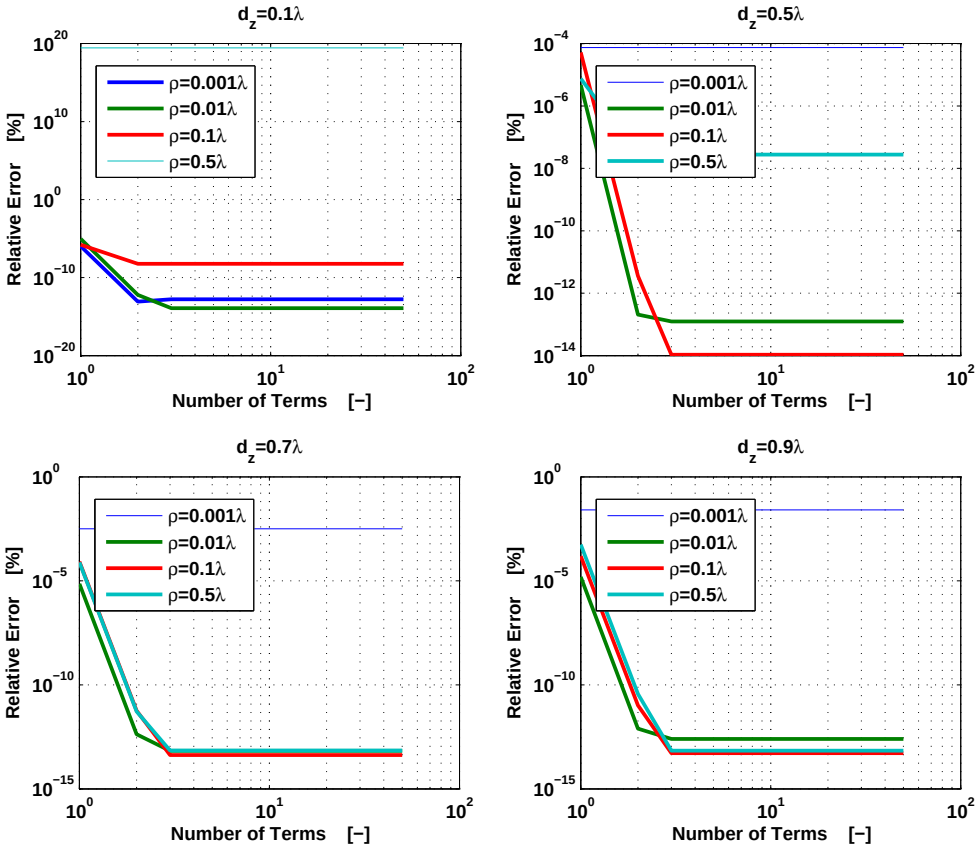

Figure 3.4: Relative error of the Ewald summation as a function of the number of terms.

3.3 Conclusions

In this chapter we examined the convergence properties of different acceleration methods introduced before in Chapter 2. Starting from the spatial domain method, we then considered the dyadic Green's function in the spectral domain which consists of a Hankel function of zero order and second kind. Since the Hankel function for large arguments is vanishing faster, the spectral domain summation is converging faster on account of the

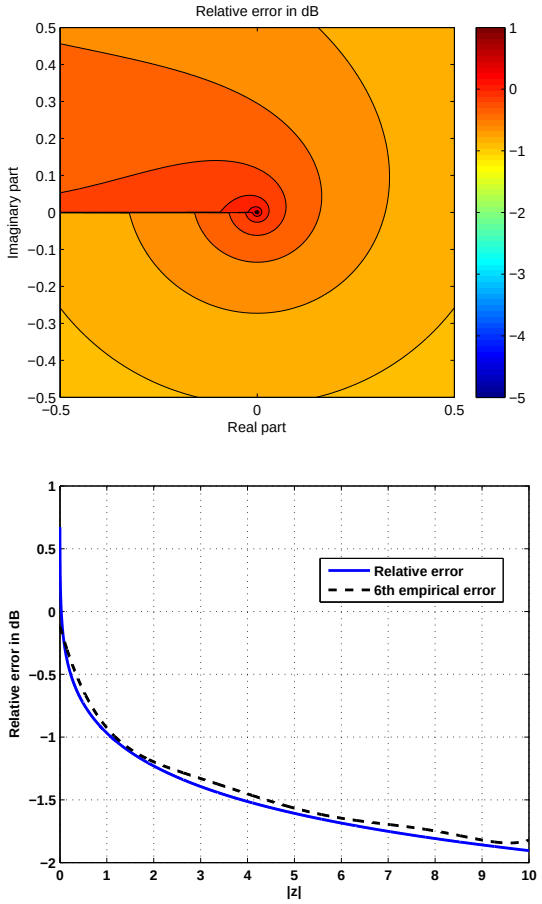

Figure 3.5: On the top: contour plot of the relative error between the Hankel function and its asymptotic form. At the bottom: 6th order polynomial approximation of the relative function evaluation error.

Hankel function argument which depends on the plate distance d_z, the modal index n, and the distance from the line array ρ. In other words, we conclude that for a larger distance to the line array of sources, the higher-order modes are small enough so that only a few modal terms contribute to the spectral summation.

From the spatial summation evaluation of the dyadic Green's function, it is shown that the relative error is increased for a larger distance to the line array for a given parallel plate distance. Also, we observed that the relative error dependence on d_z is negligible, while in the spectral summation this dependence can be recognized easily due to the Hankel function argument $\alpha_n\rho$.

We also made a comparison of the spatial summation convergence rate after applying the Shanks transformation. It is concluded that for a repeated application of the Shanks transformation, we can achieve a larger convergence rate (i.e. less number of terms) as compared to the spatial summation alone.

The Ewald method has been examined for different values of d_z and ρ, where we encountered a large relative error when the parameter ρ exceeds one wavelength.

Finally, an empirical model to approximate the relative error between the Hankel function and its asymptotic form for large arguments has been developed. This polynomial can be used to decide for which arguments of the Hankel function the asymptotic form of the Hankel function should be used to reduce the evaluation time of the spectral summation.

Chapter 4

The Method of Moments

In this chapter we discretize and solve the Electric Field Integral Equation (EFIE) which was developed in Chapter 2. Toward this end, we describe the selection process of a set of suitable basis and test functions. The computation of the moment matrix elements, the singularity problem arising in potential integrals, and the solution of the moment matrix equation are described briefly afterwards. Finally, the method of moments is applied to a structure consisting of two monopole antennas that are isolated by a row of pins in a parallel-plate waveguiding region.

4.1 Introduction

The method of moments (MoM) is a widely-used numerical method to compute the impedance, radiation and propagation characteristics of electromagnetic structures such as antennas, scatterers, and waveguides [19]. In this method, a continuous operator equation with limited spatial domain, which is here the EFIE, is transformed into a matrix equation. This discretization is realized by choosing a suitable set of basis functions for the unknown current distributions. That is, the total (equivalent) currents are expressed in terms of a linear combination of basis functions. In addition, the operator equation must be tested through a suitable set of weighting functions to arrive at a matrix equation that can be solved for the unknown expansion coefficients for the current [20].

4.2 Electric Field Integral Equation

In the previous section, the free space electromagnetic fields which exist outside the source area have been determined through evaluation of the $\boldsymbol{A}$ and ϕ potentials. In this section, an integral equation is developed for the equivalent electric current through imposing the electric field boundary condition at the support region of this source current.

Consider an electromagnetic field $\{\boldsymbol{E}^{\mathrm{i}}, \boldsymbol{H}^{\mathrm{i}}\}$ and an impedance sheet which is illuminated by this field in free space. The treatment of the parallel-plate Green's function is discussed in Sec.4.5. The incident field on the impedance sheet induces a current which gives rise to the scattered field $\{\boldsymbol{E}^{\mathrm{s}}, \boldsymbol{H}^{\mathrm{s}}\}$. Using the linearity of Maxwell's equations, the total resultant electric field is

$$\boldsymbol{E} = \boldsymbol{E}^{\mathrm{i}}(\boldsymbol{r}) + \boldsymbol{E}^{\mathrm{s}}(\boldsymbol{J}_{\mathcal{S}}, \boldsymbol{r}) \qquad \text{for} \quad \boldsymbol{r} \in \mathbb{R}^3 \tag{4.1}$$

where the scattered field $\boldsymbol{E}^{\mathrm{s}}(\boldsymbol{J}_{\mathcal{S}})$ is assumed to be generated by the current density $\boldsymbol{J}_{\mathcal{S}}$. If $\boldsymbol{J}_{\mathcal{S}}$ is the equivalent induced current on a conductor surface with an equivalent sheet impedance $Z_{\mathcal{S}}$, the electric field must satisfy the impedance boundary condition [6]

$$\left[\boldsymbol{E}^{\mathrm{i}}(\boldsymbol{r}) + \boldsymbol{E}^{\mathrm{s}}(\boldsymbol{J}_{\mathcal{S}}, \boldsymbol{r})\right]_{\tan} = Z_{\mathcal{S}} \boldsymbol{J}_{\mathcal{S}}. \tag{4.2}$$

Substituting (2.9) and (2.12) in (2.3), the scattered field $\boldsymbol{E}^{\mathrm{s}}$ is found to be given as

$$\begin{aligned} \boldsymbol{E}^{\mathrm{s}} &= -j\omega\mu_0 \boldsymbol{A} - \boldsymbol{\nabla}\phi \\ &= -j\omega\mu_0 \iint_{\mathcal{S}} G(\boldsymbol{r} - \boldsymbol{r}') \boldsymbol{J}_{\mathcal{S}}(\boldsymbol{r}') \,\mathrm{d}S' + \frac{1}{j\omega\varepsilon_0} \boldsymbol{\nabla} \left(\iint_{\mathcal{S}} G(\boldsymbol{r} - \boldsymbol{r}') \boldsymbol{\nabla}' \cdot \boldsymbol{J}_{\mathcal{S}}(\boldsymbol{r}') \,\mathrm{d}S' \right) \end{aligned} \tag{4.3}$$

where the free-space Green's function G is defined as

$$G(\boldsymbol{r} - \boldsymbol{r}') = \frac{e^{-jk_0|\boldsymbol{r} - \boldsymbol{r}'|}}{4\pi |\boldsymbol{r} - \boldsymbol{r}'|}. \tag{4.4}$$

Finally, substituting (4.3) in (4.2) yields, in terms of potentials, the equation

$$-\boldsymbol{E}^{\mathrm{i}}_{\tan} = (-j\omega\mu_0 \boldsymbol{A} - \boldsymbol{\nabla}\phi)_{\tan} - Z_{\mathcal{S}} \boldsymbol{J}_{\mathcal{S}} \tag{4.5}$$

which is known as the Electric Field Integral Equation (EFIE). The EFIE can be solved for the unknown current density $\boldsymbol{J}_{\mathcal{S}}$ through the method of moments as described below.

4.3 Discretization of the EFIE

To discretize and solve the EFIE in (4.5), we first expand the surface current $\boldsymbol{J}_{\mathcal{S}}$ in terms of N basis functions, i.e.,

$$\boldsymbol{J}_{\mathcal{S}}(\boldsymbol{r}') = \sum_{n=1}^{N} I_n \boldsymbol{f}_n(\boldsymbol{r}') \tag{4.6}$$

where I_n are the unknown expansion coefficients and $\{\boldsymbol{f}_n\}$ is the set of basis functions, yet to be specified (see Sec. 4.4). The substitution of the expansion for the current in (2.9) and (2.12) yields

$$\boldsymbol{A}(\boldsymbol{r}) = \sum_{n=1}^{N} I_n \iint_{\mathcal{S}_n} G(\boldsymbol{r}-\boldsymbol{r}')\, \boldsymbol{f}_n(\boldsymbol{r}')\, \mathrm{d}S' \tag{4.7a}$$

$$\Phi(\boldsymbol{r}) = \frac{-1}{j\omega\varepsilon_0} \sum_{n=1}^{N} I_n \iint_{\mathcal{S}_n} G(\boldsymbol{r}-\boldsymbol{r}')\, \boldsymbol{\nabla}'_t \cdot \boldsymbol{f}_n(\boldsymbol{r}')\, \mathrm{d}S'. \tag{4.7b}$$

Here, $\boldsymbol{\nabla}'_t = \boldsymbol{\nabla}' - \partial_n \hat{\boldsymbol{n}}$ is the surface divergence operator with respect to the primed coordinates, and $\mathcal{S}_n$ is the support of basis function $\boldsymbol{f}_n$ defined as the spatial region where the basis function attains a nonzero value. The EFIE in (4.2) can be written in the abstract operator form

$$-\boldsymbol{E}^{\mathrm{i}}_{\tan}(\boldsymbol{r}) = L\{\boldsymbol{J}_S(\boldsymbol{r})\} \tag{4.8}$$

where L is the EFIE operator. Next, substituting (4.6) in (4.8) yields

$$-\boldsymbol{E}^{\mathrm{i}}_{\tan} \approx \sum_{n=1}^{N} I_n L\{\boldsymbol{f}_n(\boldsymbol{r}')\}. \tag{4.9}$$

Now we define a field approximation error – or residual field function – $\boldsymbol{R}$ as

$$\boldsymbol{R}(\boldsymbol{r}) = \boldsymbol{E}^{\mathrm{i}}_{\tan} + \sum_{n=1}^{N} I_n L\{\boldsymbol{f}_n(\boldsymbol{r}')\} \tag{4.10}$$

The objective is to minimize $\boldsymbol{R}$ at the points on the surface $\mathcal{S}$ which have considerably large field intensities. There exists a specific form of testing called point matching, in which $\boldsymbol{R}$ is enforced $\boldsymbol{0}$ at N distinct points [19]. The alternative and more general (weak)

form of testing can be achieved through multiplying the residual functions by N weighting functions, i.e.,

$$\langle \boldsymbol{R}, \boldsymbol{w}_m \rangle = \iint\limits_{\mathcal{S}_m} \boldsymbol{R}(\boldsymbol{r}) \cdot \boldsymbol{w}_m(\boldsymbol{r}) \mathrm{d}S = 0 \quad \text{for} \quad m = 1, 2, ..., N, \tag{4.11}$$

where $\mathcal{S}_m$ is the mth support of the mth weighting function $\boldsymbol{w}_m$, and $\langle \cdot, \cdot \rangle$ denotes the symmetric product. The weighting functions in the point-matching method are real-valued and chosen as $\boldsymbol{w}_m(\boldsymbol{r}) = \hat{\boldsymbol{p}}_m \delta(\boldsymbol{r} - \boldsymbol{r}_m)$, where $\hat{\boldsymbol{p}}_m$ is the polarization vector at the mth test point $\boldsymbol{r}_m$. In Galerkin's method, which is the method that will be used in this thesis, the weighting functions are selected to be equal to the basis functions, i.e., $\boldsymbol{w}_m = \boldsymbol{f}_m$ for all values of m. Using Galerkin's method, Eq. (4.10) is converted into the matrix equation

$$\sum_{n=1}^{N} Z_{mn} I_n = V_m \quad \text{for} \quad m = 1, 2, ..., N \tag{4.12}$$

where

$$Z_{mn} = \langle L \{ \boldsymbol{f}_n \}, \boldsymbol{f}_m \rangle \quad \text{and} \quad V_m = -\langle \boldsymbol{E}^{\mathrm{i}}, \boldsymbol{f}_m \rangle. \tag{4.13}$$

The matrix element Z_{mn} represents the reaction integral between the electric field radiated by $\boldsymbol{f}_n$ which is tested by $\boldsymbol{f}_m$. It is pointed out that the numerical evaluation of Z_{mn} would be more difficult if $\boldsymbol{f}_n$ and $\boldsymbol{f}_m$ overlap due to the singularity encountered in the Green's function, i.e. when the source and observation points coincide (see Sec. 4.5.3). When applying Galerkin's method to discretize the EFIE using real-valued basis and test functions, there exists a symmetry in the $\mathbf{Z}$ matrix, i.e. $Z_{mn} = Z_{nm}$ for all m and n values. Also, to obtain a unique solution for the I_n coefficients, we need at least N test functions and the matrix $\mathbf{Z}$ has to be a full-rank matrix.

4.4 Choice of Basis and Test Functions

In the process of selecting basis an test functions, both the mathematical and computational aspects should be considered. Basis functions can be of the entire and/or sub-sectional domain type, where the entire-domain basis functions are supported by the entire surface, while the sub-sectional type is supported by different and smaller parts of the surface. Commonly, the matrix elements for sub-sectional basis functions, each of which is of low

order, are easier to evaluate than for entire-domain ones, although the size of the moment matrix may become larger. In the following we will apply Galerkin's method and employ real-valued subsectional type of basis functions, not to only model the currents on arbitrarily shaped structures, but to ease the discretization of the EFIE operator as well. Upon considering the EFIE in (4.5), and by expanding the current $\boldsymbol{J}_S$ in accordance with (4.6), we obtain

$$-j\omega\mu_0\langle \boldsymbol{A}, \boldsymbol{f}_m\rangle - \langle \boldsymbol{\nabla}\Phi, \boldsymbol{f}_m\rangle - \sum_{n=1}^{N} I_n\langle Z_{\mathcal{S}}\boldsymbol{f}_n, \boldsymbol{f}_m\rangle = -\langle \boldsymbol{E}^{\mathrm{i}}, \boldsymbol{f}_m\rangle \tag{4.14}$$

where $m = 1, 2, ..., N$. The potentials $\boldsymbol{A}$ and ϕ are given in (4.7a) and (4.7b), respectively.

Upon defining the outward pointing unit vector $\hat{\boldsymbol{\nu}}$ normal to the edge of the basis function support, and by applying Gauss' surface divergence theorem, it is concluded that it is beneficial to require that $\boldsymbol{f}_m \cdot \hat{\boldsymbol{\nu}}_m = 0$ along the surface boundary $\mathcal{S}_m$. In fact, this requirement means that the basis function current vector is parallel to the edges of its support surface, so that we can write (4.14) as

$$-j\omega\mu_0\langle \boldsymbol{A}, \boldsymbol{f}_m\rangle - \langle \Phi, \boldsymbol{\nabla}_t \cdot \boldsymbol{f}_m\rangle - \sum_{n=1}^{N} I_n\langle Z_{\mathcal{S}}\boldsymbol{f}_n, \boldsymbol{f}_m\rangle = -\langle \boldsymbol{E}^{\mathrm{i}}, \boldsymbol{f}_m\rangle. \tag{4.15}$$

To be able to satisfy the boundary condition for the electric field on the surface of the current sheet, the basis functions should be selected in a way that the resulting radiating electromagnetic fields (after applying the EFIE operator) are functions of finite energy. The low-order Rao-Wilton-Glisson (RWG) type of basis functions [21] is an appropriate choice to satisfy the required finite energy conditions and leads to an easy evaluation of the moment matrix elements. Assuming that the support of the nth RWG basis function $\boldsymbol{f}_n$ is made of two planar triangles, T_n^+ and T_n^-, which have a common edge length l_n as shown in Fig. 4.1, the surface current density at position $\boldsymbol{r}$ within the triangles is defined as

$$\boldsymbol{f}_n(\boldsymbol{r}) = \begin{cases} \frac{l_n}{2A_n^+}\boldsymbol{\rho}_n^+ & \boldsymbol{r} \in T_n^+ \\ \frac{l_n}{2A_n^-}\boldsymbol{\rho}_n^- & \boldsymbol{r} \in T_n^- \\ \mathbf{0} & \text{otherwise} \end{cases} \quad \text{so that} \quad \boldsymbol{\nabla}_t \cdot \boldsymbol{f}_n(\boldsymbol{r}) = \begin{cases} +\frac{l_n}{A_n^+} & \boldsymbol{r} \in T_n^+ \\ -\frac{l_n}{A_n^-} & \boldsymbol{r} \in T_n^- \\ \mathbf{0} & \text{otherwise} \end{cases} \tag{4.16}$$

where $\boldsymbol{\rho}_n^{\pm} = \pm(\boldsymbol{r} - \boldsymbol{r}_n^{\pm})$, with $\boldsymbol{r}_n^{\pm}$ the corner vertices as indicated in Fig. 4.1(a), and $A_n^{\pm}$ are the triangle surface areas. These RWG basis functions can be allocated once the conductor surface has been triangulated. It is preferred that the edges of the mesh have equal lengths (equilateral mesh) to increase the solution accuracy and to obtain a moment matrix with a good (low) condition number [22].

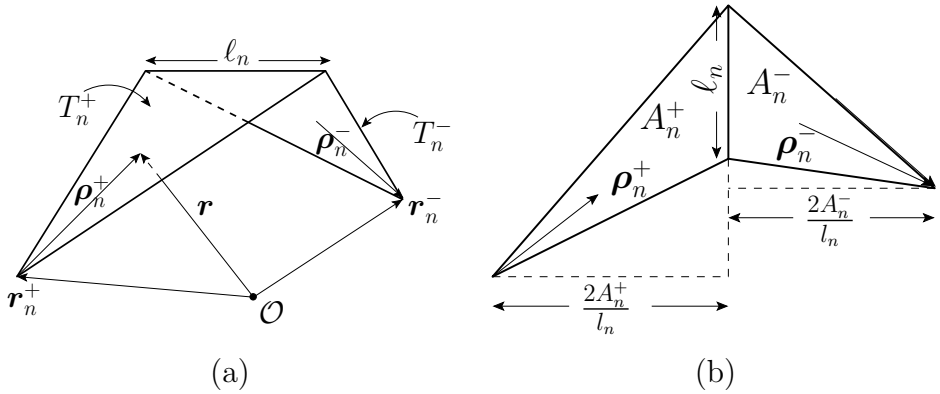

(a) (b)

Figure 4.1: RWG basis function parameters.

4.5 Moment Matrix Computation

4.5.1 Free Space Green's Function

As described in the previous sections, the element Z_{mn} of the moment matrix for a perfect electric conductor (PEC) is computed as

$$Z_{mn} = \iint\limits_{\mathcal{S}_m} \boldsymbol{E}^{\mathrm{s}}\left(\boldsymbol{f}_n\right) \cdot \boldsymbol{f}_m \mathrm{d}S. \tag{4.17}$$

This reaction integral can be computed accurately through standard Gaussian quadrature rules for triangular surfaces of sufficiently high order, whenever the scattered electric field can be well-approximated by polynomial functions [22]. The minimum size of the mesh density for an accurate phase representation of the surface current is typically about $10/\lambda$, except near conductor edges where the tangential component of the current tends to infinity and therefore requires a higher mesh density.

Considering the discredited EFIE in (4.15), each of the moment matrix elements corresponding to non-overlapping basis functions can be evaluated numerically through Gaussian quadrature rules for triangles. For RWG test functions, the second term in (4.15) is then evaluated numerically as

$$\langle \Phi, \boldsymbol{\nabla}_t \cdot \boldsymbol{f}_m \rangle \approx l_m \sum_{p=1}^{P} w_p \left[\Phi\left(\boldsymbol{r}_{m;p}^+\right) - \Phi\left(\boldsymbol{r}_{m;p}^-\right) \right] \tag{4.18}$$

where $\boldsymbol{r}_{m;p}^{\pm}$ is the pth location/quadrature point inside the triangle of the mth RWG test function, l_m is the common edge of the two triangles $T_m^{\pm}$ in the mth RWG, and w_p is the pth

weighting coefficient. Following the same numerical integration approach, the first term of (4.15) is evaluated as

$$\langle \boldsymbol{A}, \boldsymbol{f}_m \rangle \approx \frac{l_m}{2} \sum_{p=1}^{P} w_p \left[\boldsymbol{A}\left(\boldsymbol{r}_{m;p}^{+}\right) \cdot \boldsymbol{\rho}_{m;p}^{+} + \boldsymbol{A}\left(\boldsymbol{r}_{m;p}^{-}\right) \cdot \boldsymbol{\rho}_{m;p}^{-} \right] \tag{4.19}$$

where $\boldsymbol{\rho}_{m;p}^{\pm} = \pm(\boldsymbol{r} - \boldsymbol{r}_{m;p}^{\pm})$. The expression involving the incident field $\boldsymbol{E}^{\mathrm{i}}$ can be obtained in a form similar to (4.19). The surface impedance term in Eq. (4.15) is computed as

$$\sum_{n=1}^{N} I_n \langle Z_{\mathcal{S}} \boldsymbol{f}_n, \boldsymbol{f}_m \rangle = \sum_{n=1}^{N} I_n Z_{mn}^{\mathrm{IBC}} \tag{4.20}$$

where, if $Z_{\mathcal{S}}$ is selected as a constant value, the matrix $\mathbf{Z}^{\mathrm{IBC}}$ can be written as the product of $Z_{\mathcal{S}}$ with the Gram matrix of the basis functions [22]. Substituting Eqs. (4.18)-(4.20) in (4.15), and replacing $\boldsymbol{A}$ and ϕ in (4.7) with their discredited approximations, a series of linear equations is obtained of the form $\mathbf{ZI} = \mathbf{V}$. The element Z_{mn} of the matrix $\mathbf{Z}$ is computed as

$$Z_{mn} = Z_{mn}^{\mathrm{PEC}} - Z_{mn}^{\mathrm{IBC}} = \langle \boldsymbol{E}^{\mathrm{s}}\left(\boldsymbol{f}_n\right), \boldsymbol{f}_m \rangle - \langle Z_{\mathcal{S}} \boldsymbol{f}_n, \boldsymbol{f}_m \rangle \tag{4.21}$$

where the symmetric product of the basis functions $\boldsymbol{f}_n$ and $\boldsymbol{f}_m$ on the triangle T can be given in terms of its area A, triangle's vertices $\left\{\boldsymbol{r}_1^{[T]}, \boldsymbol{r}_2^{[T]}, \boldsymbol{r}_3^{[T]}\right\}$, and the orientation of the current for $\boldsymbol{f}_n$ and $\boldsymbol{f}_m$ in that triangle [22]. Also, for the elements of the excitation vector we have that

$$V_m = -\langle \boldsymbol{E}^{\mathrm{i}}, \boldsymbol{f}_m \rangle. \tag{4.22}$$

Next, upon using the basis function description in (4.16), and by the application of Gaussian quadrature rules, we numerically evaluate the potential integrals as

$$\boldsymbol{A}_{mn;p}^{\pm} \approx \pm \frac{l_n}{2} \sum_{q=1}^{P} w_q [G(\boldsymbol{r}_{m;p}^{\pm} - \boldsymbol{r}_{n;q}^{+}) \boldsymbol{\rho}_{n;q}^{+} + G(\boldsymbol{r}_{m;p}^{\pm} - \boldsymbol{r}_{n;q}^{-}) \boldsymbol{\rho}_{n;q}^{-}] \tag{4.23a}$$

$$\Phi_{mn;p}^{\pm} \approx \mp \frac{l_n}{j\omega\varepsilon_0} \sum_{q=1}^{P} w_q [G(\boldsymbol{r}_{m;p}^{\pm} - \boldsymbol{r}_{n;q}^{+}) - G(\boldsymbol{r}_{m;p}^{\pm} - \boldsymbol{r}_{n;q}^{-})] \tag{4.23b}$$

where G is the free space Green's function defined as

$$G\left(\boldsymbol{r}_{m;p}^{\pm} - \boldsymbol{r}_{n;q}^{\pm}\right) = \frac{e^{-jk_0 \left|\boldsymbol{r}_{m;p}^{\pm} - \boldsymbol{r}_{n;q}^{\pm}\right|}}{4\pi \left|\boldsymbol{r}_{m;p}^{\pm} - \boldsymbol{r}_{n;q}^{\pm}\right|}. \tag{4.24}$$

In both the expressions for computing the elements of $\mathbf{Z}$ and $\mathbf{V}$, the Gaussian quadrature rule is chosen to be of the same order as the one used to test the electric field.

4.5.2 Parallel-Plate Green's Function

In the previous section, discretized expressions for the magnetic vector and electric scalar potentials, $\boldsymbol{A}$ and ϕ, have been derived [see Eq. (4.7)], where the free-space Green's function has been applied. Below we derive the discretized form of these potentials for the parallel-plate Green's function. With reference to (4.7a), and by the application of the Gaussian quadrature rules, the magnetic vector potential is discretized as

$$\boldsymbol{A}^{\pm}_{mn;p} \approx \pm\frac{l_n}{2}\sum_{q=1}^{P} w_q[\mathbf{G}(\boldsymbol{r}^{\pm}_{m;p}-\boldsymbol{r}^{+}_{n;q})\boldsymbol{\rho}^{+}_{n;q}+\mathbf{G}(\boldsymbol{r}^{\pm}_{m;p}-\boldsymbol{r}^{-}_{n;q})\boldsymbol{\rho}^{-}_{n;q}] \tag{4.25}$$

where $\mathbf{G}$ is the dyadic parallel-plate Green's function as defined in (2.13) and (2.19). That is, the diagonal matrix elements of $\mathbf{G}$, which are G_{xx}, G_{yy} and G_{zz}, are computed as

$$\begin{aligned}
G_{xx} &= \sum_{i=-I}^{I}\frac{e^{-jk_0\left|\boldsymbol{r}^{\pm}_{m;p}-\boldsymbol{r}^{\pm}_{n;q}+2id\hat{\boldsymbol{z}}\right|}}{4\pi\left|\boldsymbol{r}^{\pm}_{m;p}-\boldsymbol{r}^{\pm}_{n;q}+2id\hat{\boldsymbol{z}}\right|}-\sum_{i=-I}^{I}\frac{e^{-jk_0\left|\boldsymbol{r}^{\pm}_{m;p}-\boldsymbol{r}^{\pm}_{n;q}+(2id-2(d-z^{\pm}_{n;q}))\hat{\boldsymbol{z}}\right|}}{4\pi\left|\boldsymbol{r}^{\pm}_{m;p}-\boldsymbol{r}^{\pm}_{n;q}+(2id-2(d-z^{\pm}_{n;q}))\hat{\boldsymbol{z}}\right|}\\
G_{yy} &= G_{xx}\\
G_{zz} &= \sum_{i=-I}^{I}\frac{e^{-jk_0\left|\boldsymbol{r}^{\pm}_{m;p}-\boldsymbol{r}^{\pm}_{n;q}+2id\hat{\boldsymbol{z}}\right|}}{4\pi\left|\boldsymbol{r}^{\pm}_{m;p}-\boldsymbol{r}^{\pm}_{n;q}+2id\hat{\boldsymbol{z}}\right|}+\sum_{i=-I}^{I}\frac{e^{-jk_0\left|\boldsymbol{r}^{\pm}_{m;p}-\boldsymbol{r}^{\pm}_{n;q}+(2id-2(d-z^{\pm}_{n;q}))\hat{\boldsymbol{z}}\right|}}{4\pi\left|\boldsymbol{r}^{\pm}_{m;p}-\boldsymbol{r}^{\pm}_{n;q}+(2id-2(d-z^{\pm}_{n;q}))\hat{\boldsymbol{z}}\right|}\\
&\text{for}\quad I\to\infty.
\end{aligned} \tag{4.26}$$

By evaluating G_{xx} as $T(G_{xx})$, where T is the Shanks transformation defined in (2.78), the convergence rate of this partial summation can be improved considerably.

Likewise, the discretized version of the electric scalar potential (2.26) becomes

$$\Phi^{\pm}_{mn;p} \approx \mp\frac{l_n}{j\omega\varepsilon_0}\sum_{q=1}^{P} w_q[G_{xx}(\boldsymbol{r}^{\pm}_{m;p}-\boldsymbol{r}^{+}_{n;q})-G_{xx}(\boldsymbol{r}^{\pm}_{m;p}-\boldsymbol{r}^{-}_{n;q})]. \tag{4.27}$$

4.5.3 Singularity treatment in Potential Integrals

As mentioned in Sec. 4.5.1, the reaction integrals between distant sources and observation basis functions can be computed using Gaussian quadrature rules. However, the potential integrals have a singular kernel when the source and the observation basis functions share a common edge, a single vertex, or coincide completely with each other. Considering the potential formulations as in (4.7), the singularity is of the type $1/R$ and occurs if $\boldsymbol{r}=\boldsymbol{r}'$.

Hence, without regularizing the kernel of the integral equation, Gaussian quadrature rules cannot be used for the numerical evaluation of self reaction integrals.

In computing the reaction integrals for a pair of source and observation triangles, 4-D integrals (2D for computing the potentials and 2D for computing the reaction integral) need to be evaluated [22]. Different numerical and analytical approximations for these integrals have been given for different types of source and basis functions [23]. Herein, we apply the singularity subtraction method to the 2-D inner integral (i.e. the evaluation of the potential integrals) for sources with linear variation over their triangular support. In this method we subtract the static potential from the time harmonic one as follows

$$\iint\limits_{T_n} \frac{e^{-jk_0R}}{R}\mathrm{d}S' = \iint\limits_{T_n} \left(\frac{e^{-jk_0R}-1}{R}\right)\mathrm{d}S' + \iint\limits_{T_n} \frac{1}{R}\mathrm{d}S' \tag{4.28a}$$

$$\iint\limits_{T_n} \boldsymbol{\rho}_n^{i'}(\boldsymbol{r}')\frac{e^{-jk_0R}}{R}\mathrm{d}S' = \iint\limits_{T_n} \boldsymbol{\rho}_n^{i'}(\boldsymbol{r}')\left(\frac{e^{-jk_0R}-1}{R}\right)\mathrm{d}S' + \iint\limits_{T_n} \frac{\boldsymbol{\rho}_n^{i'}(\boldsymbol{r}')}{R}\mathrm{d}S' \tag{4.28b}$$

where $i' \in \{1,2,3\}$. Note that the static $1/R$ potential has been extracted from the time-harmonic potential.

The method applied here to extract the Green's function singularity is described in [24], where a residual function with enough regularity has been retained. This methodology can be applied to perform a semi-analytical evaluation of the electric potential integral for a linear-varying current defined on the source triangle T_n whose electric field is observed at the pth quadrature point on the triangle $T_m^{\pm}$ of the mth observation RWG. Accordingly, the following terms are extracted and added to the Green's function:

$$\begin{aligned}
\Phi_{mn;p}^{\pm} &= \mp\frac{l_n}{4\pi A_n j\omega\varepsilon_0}\iint\limits_{T_n}\frac{e^{-jk_0R}}{R}\mathrm{d}S' \\
&= \mp\frac{l_n}{4\pi A_n j\omega\varepsilon_0}\iint\limits_{T_n}\left(\frac{e^{-jk_0R}-1}{R}+\frac{k_0^2}{2}R\right)\mathrm{d}S' \\
&\quad \mp\frac{l_n}{4\pi A_n j\omega\varepsilon_0}\iint\limits_{T_n}\left(\frac{1}{R}-\frac{k_0^2}{2}R\right)\mathrm{d}S'
\end{aligned} \tag{4.29}$$

where $R = |\boldsymbol{r}^{\pm}_{m;p} - \boldsymbol{r}'|$. Similarly, the magnetic vector potential is written as

$$\begin{aligned}\boldsymbol{A}^{\pm}_{mn;p} &= \pm\frac{l_n}{8\pi A_n}\iint\limits_{T_n}\boldsymbol{\rho}'_n\frac{e^{-jk_0R}}{R}\mathrm{d}S' \\ &= \pm\frac{l_n}{8\pi A_n}\iint\limits_{T_n}\boldsymbol{\rho}'_n\left(\frac{e^{-jk_0R}-1}{R}+\frac{k_0^2}{2}R\right)\mathrm{d}S' \\ &\pm\frac{l_n}{8\pi A_n}\iint\limits_{T_n}\boldsymbol{\rho}'_n\left(\frac{1}{R}-\frac{k_0^2}{2}R\right)\mathrm{d}S'. \end{aligned} \tag{4.30}$$

Note that, in case the pth observation quadrature point $\boldsymbol{r}^{\pm}_{m;p}$ coincides with the qth source quadrature point $\boldsymbol{r}_{n;q}$, we should use that

$$\lim_{R\to 0}\left\{\frac{e^{-jk_0R}-1}{R}\right\} = -jk_0. \tag{4.31}$$

The residual parts in (4.29) and (4.30) are evaluated numerically, while the remaining integral terms can be evaluated in closed-form. The terms that can be evaluated analytically are of the type

$$K_1^{\alpha} = \iint\limits_{T_n} R^{\alpha}\mathrm{d}S' \tag{4.32a}$$

$$\boldsymbol{K}_2^{\alpha} = \iint\limits_{T_n} R^{\alpha}(\boldsymbol{r}'-\boldsymbol{q})\mathrm{d}S' \tag{4.32b}$$

where $\alpha = -1, 1, 3, ...,$ $R^{\alpha} = |\boldsymbol{r}-\boldsymbol{r}'|^{\alpha}$ for any observation point $\boldsymbol{r}$, and $\boldsymbol{q}$ is a corner vertex of triangle T_n from which the current originates. These integrals can be evaluated analytically using the relations given in Appendix B.

4.6 Matrix solution

After discretizing the EFIE, we can consider the solution of the matrix equation $\mathbf{ZI} = \mathbf{V}$, where $\mathbf{Z}$ is a symmetric, square and complex matrix of size $N \times N$. The expansion coefficient vector $\mathbf{I}$, which is of size $N \times 1$, can be determined through the application of a standard Gaussian elimination method, that is, factorizing the matrix $\mathbf{Z}$ to obtain the matrix equation

$$\mathbf{LUI} = \mathbf{V}. \tag{4.33}$$

It is assumed that the matrix $\mathbf{Z}$ is an invertible matrix, which means it has rank N. The singularity-free characteristics of the matrix $\mathbf{Z}$ can be assured by its condition number, which can be determined through the Singular Value Decomposition (SVD) method. Using the SVD method, a matrix $\mathbf{A} \in \mathbb{C}^{M\times N}$ is factorized as

$$\mathbf{A} = \mathbf{U}\mathbf{D}\mathbf{Q}^H \tag{4.34}$$

where $\mathbf{U}$ and $\mathbf{Q}$ are unitary matrices, which means $\mathbf{U}^{-1} = \mathbf{U}^H$ and $\mathbf{Q}^{-1} = \mathbf{Q}^H$, where the superscript H denotes the complex conjugate transpose and $\mathbf{D} = \mathrm{diag}(\sigma_1, \sigma_2, ..., \sigma_N)$ is a diagonal matrix holding the singular values. Application of the SVD method to $\mathbf{Z}\mathbf{I} = \mathbf{V}$, and solving for $\mathbf{I}$, yields

$$\mathbf{I} = \mathbf{Q}\mathbf{D}^{-1}\mathbf{U}^H\mathbf{V} = \sum_{n=1}^{N} \frac{1}{\sigma_n} \left(\mathbf{u}_n^* \cdot \mathbf{V}\right) \mathbf{q}_n \tag{4.35}$$

where $\mathbf{u}_n$ and $\mathbf{q}_n$ are the left-singular and the right-singular vectors of the matrix $\mathbf{A}$, respectively. The stability of the solution vector $\mathbf{I}$ for small changes in $\mathbf{Z}$, can be measured by the condition number of the matrix $\mathbf{Z}$, which is defined through the 2-norm as

$$\kappa(\mathbf{Z}) = |\mathbf{Z}||\mathbf{Z}^{-1}| = \frac{\sigma_{\max}(\mathbf{Z})}{\sigma_{\min}(\mathbf{Z})}. \tag{4.36}$$

4.7 Numerical Results

In this section we describe the simulation results of the antenna structure as shown in Fig. 4.2. The accuracy of the moment method as described in this chapter has been assessed through using the in-house developed CAESAR software. The CAESAR software is a combination of an electromagnetic solver and a microwave circuit simulator which is based on the method of moments [25]. Since CAESAR employs only the Shanks transformation for the fast computation of the dyadic Green's function, the primary objective of the numerical simulations is to study the accuracy of the Shanks transformation for different number of summation terms and orders on the computed S-parameters.

The parallel-plate waveguide structure in Fig. 4.2(a) consists of two monopole antennas and a row of pins to minimize the electromagnetic coupling between the monopoles (parallel-plate waveguide not shown). The sizes of the pins have been designed for a groove gap waveguide with a parallel plate distance of 7.25 millimeter and for a central operating

frequency of 14 GHz [26]. In this work, two kind of source excitations have been considered for exciting the antenna structure: (i) the voltage-gap excitation and; (ii) the coaxial probe excitation. In Fig. 4.2 and Fig. 4.3 the analyzed antenna structure with voltage-gap and coaxial probe excitation along with the magnitude of the average current distribution on the pins and monopoles are shown. As shown in Fig. 4.3(a), given the dimensions of the air coaxial probe, its characteristic impedance is given for TEM-mode propagation as [27]

$$Z_0 = \frac{1}{2\pi}\sqrt{\frac{\mu_0}{\varepsilon_0}}\ln\left(\frac{b}{a}\right) \tag{4.37}$$

which is $Z_0 = 49.9745\Omega$ in our case.

In Fig. 4.4 it is confirmed that for a Shanks transformation of order 2, using only 5 terms, higher accuracy is achieved for the input reflection coefficient of the antenna structure, both for a voltage-gap and coaxial probe excitation, as opposed to a zeroth-order Shanks transformation. The antenna analysis has also been carried out using the HFSS software [28] and been compared to the results obtained with CAESAR. While the RWG basis functions are used in the application of the moment method in the CAESAR software, in the HFSS simulations, the Finite Element Method (FEM) is employed where the whole structure is subdivided into several smaller regions and a local function is used to model the field in each sub region. These smaller regions are called tetrahedra, where a single tetrahedron is basically a four-sided pyramid. The simulated results for the S_{11} and S_{22} parameters are shown in Fig. 4.5. As shown in Fig. 4.5, there is a good agreement between the results obtained with CAESAR and those simulated in the HFSS software.

The effects of the row of pins on the mutual coupling between the two monopole antennas for the voltage-gap and coaxial probe excitation has been simulated both in CAESAR and the HFSS software. In Fig. 4.6 we observe that there is at least 10 dB loss in the S_{21} parameter for both types of ports, which is due to the field blockage caused by the row of pins. We also examined the field blockage effect due to the row of pins when the top lid is removed. In Fig. 4.7 there is no obvious difference in field blockage level when there is no top lid, specifically at the operation frequency of 14 GHz.

4.8 Conclusion

In this chapter a detailed description of the method of moments is presented which provides a deeper insight in the steps that are required to discretize the EFIE operator and to solve dielectric-free waveguide and antenna structures. The application of this numerical method to a parallel-plate waveguide structure, excited by a pair of monopole antennas that are separated by a row of pins, has been examined through the CAESAR and HFSS simulators. From the obtained results, we can see how the order and number of terms in the Shanks transformation affect the accuracy of the computed S-parameters. Also, it is observed that there exists a closer match between the HFSS and CAESAR results when the coaxial probe is used as the excitation source, compared to the voltage-gap generator.

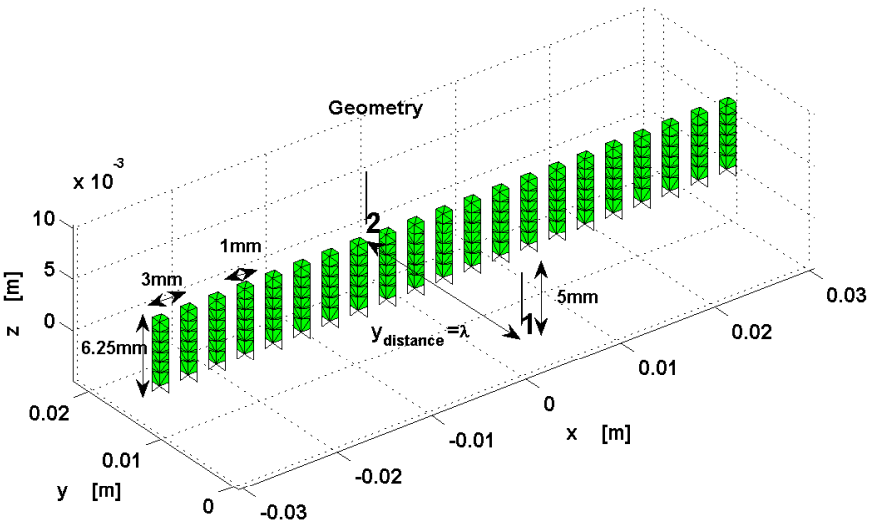

(a)

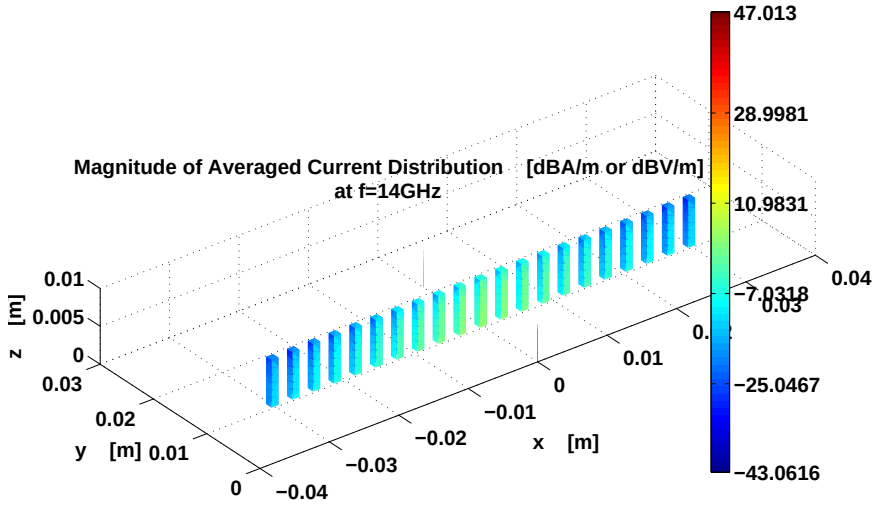

(b)

Figure 4.2: Geometrical dimensions and magnitude of the current of two monopole-antennas with voltage-gap excitations.

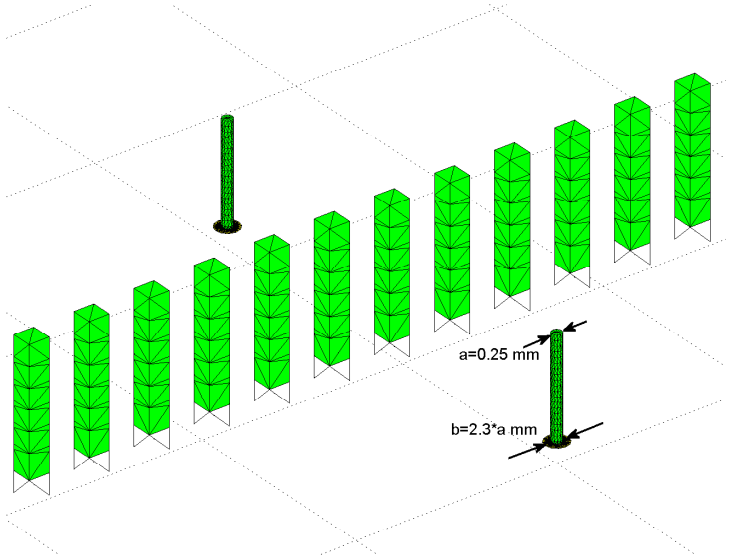

(a)

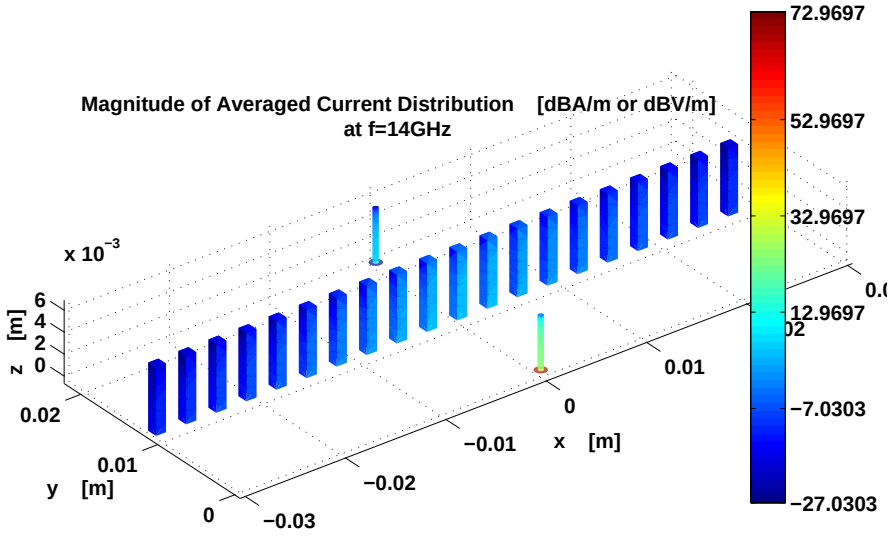

(b)

Figure 4.3: Geometrical dimensions and magnitude of the current of two monopole-antennas with coaxial excitations.

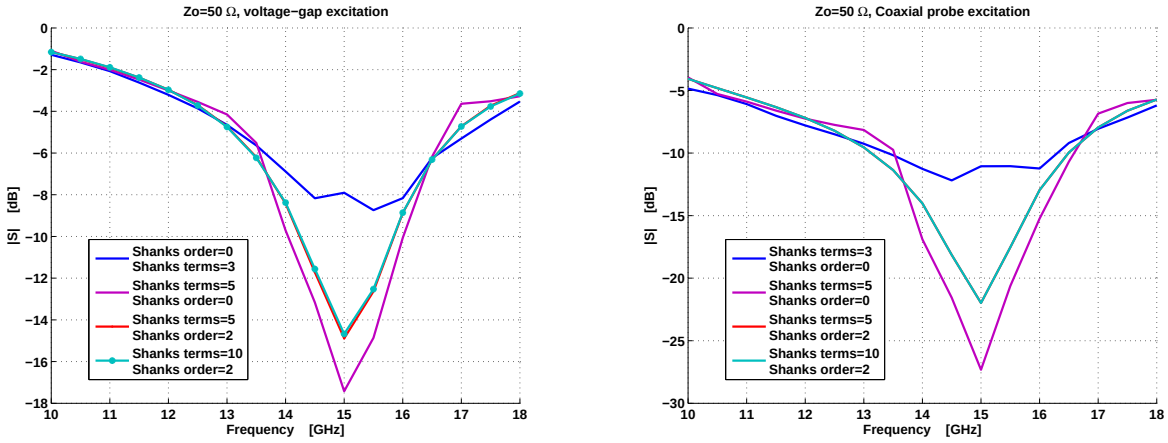

(a) (b)

Figure 4.4: Input reflection coefficient of the two monopole-antenna structure for different Shanks terms and orders, with voltage-gap and coaxial probe excitation.

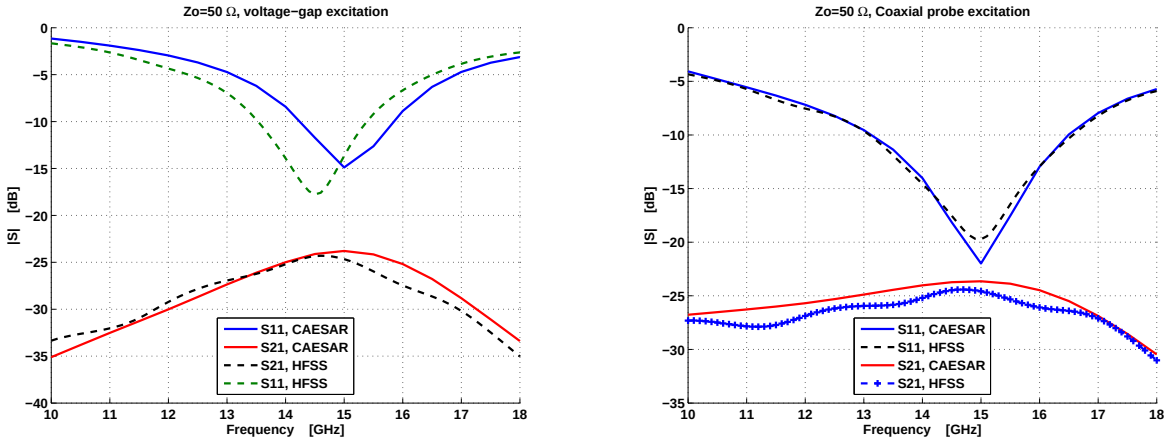

(a) (b)

Figure 4.5: S_{11} and S_{21} parameter of the two monopole antenna structures with (a) voltage-gap and (b) coaxial probe excitation, simulated in CAESAR and HFSS.

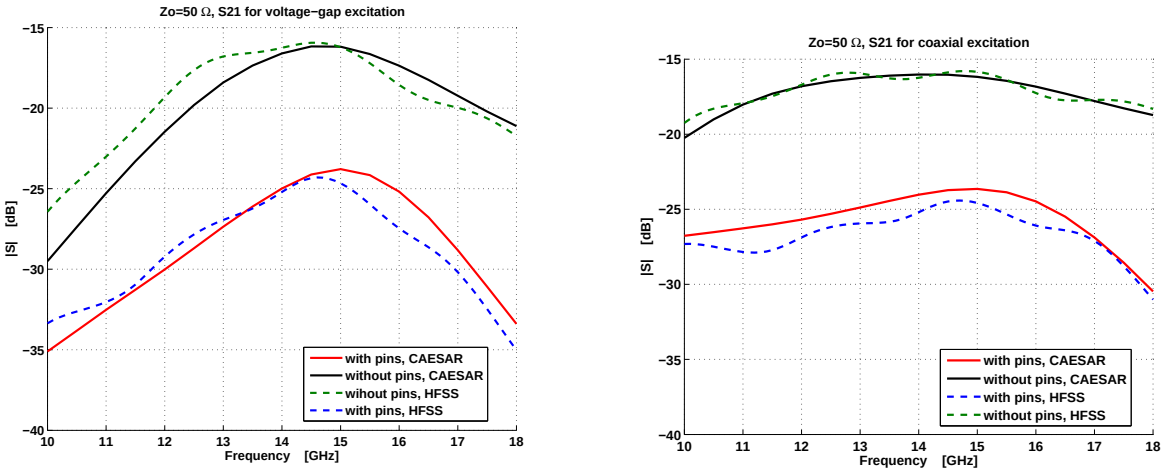

Figure 4.6: Field blockage effect due to the pins; S_{21} parameter.

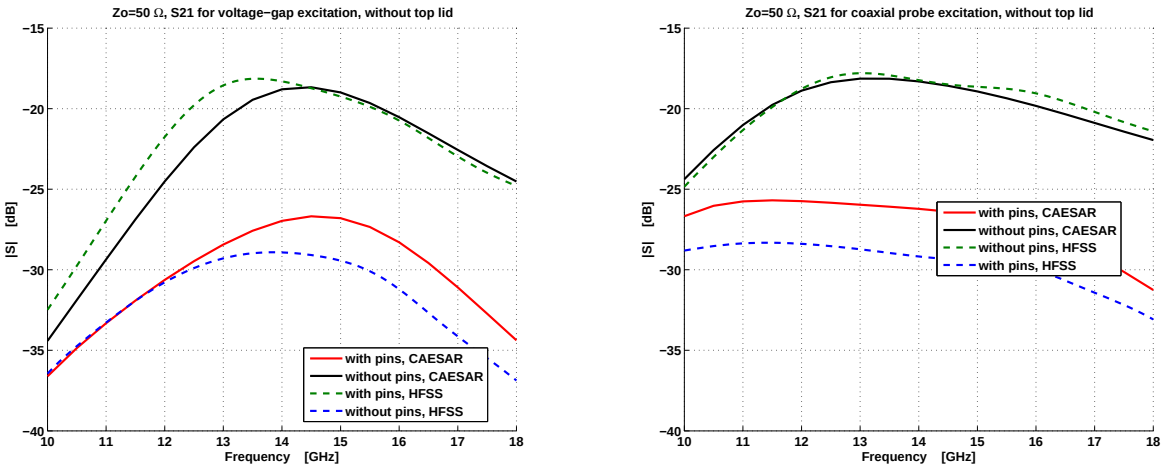

Figure 4.7: Field blockage effect due to the pins when the top lid is removed; S_{21} parameter.

Chapter 5

Padé Adaptive Frequency Sampling Method

In this chapter we introduce the Padé rational function fitting technique to interpolate the input impedance of antenna and waveguide structures in the frequency domain. An adaptive frequency sampling method is proposed to determine a few coefficients that can be used to accurately reconstruct the input impedance matrix at any frequency within the modeled frequency range. The method is applied to a parallel-plate waveguiding structure of two monopoles in order to predict the input impedance matrix over a frequency range of $10 - 60$ *GHz. Finally, the performance of the adaptive frequency sampling method is studied.*

5.1 Introduction

In Chapter 2 and 3 we described and applied different computational methods to increase the computational efficiency for the evaluation of the dyadic parallel-plate Green's function. In the following, we propose another method to speed-up the numerical computations for wide-band antenna and waveguide systems. The objective is to minimize the number of frequency samples needed to predict the port input impedance characteristics over a large bandwidth. For this purpose we propose to use the Padé rational function fitting model, which is commonly used for model-based parameter estimation (MBPE) in the

frequency domain [29]. The MBPE technique is used to avoid obtaining all the samples of the measured data by performing a coarse sampling of the data while using interpolation functions to predict remaining samples. These fitting models can be handled analytically and are more appropriate for optimization purposes as opposed to the numerical data.

The Padé rational functions, can be used to represent complicated pole-zero functional forms. Since the spectral input impedance characteristics exhibit this pole-zero behavior, the Padé approximation seems a logical choice for the interpolation of frequency dependent data. Starting with a rational function pole-zero fitting model to interpolate the input impedance data, we will see that a single set of polynomial coefficients in the numerator and denominator can be used to reconstruct the entire input impedance at any frequency within the range of the corresponding fitting model [30].

5.2 Equivalent Circuit Model of a Dipole Antenna

As it is mentioned in the introduction, input impedance characteristics typically exhibit a pole-zero functional form. To justify the use of the Padé rational function fitting model for this type of sampled data, we start with a simple example of a dipole antenna with arbitrary length and will derive the equivalent circuit of this dipole antenna as a function of the frequency f, or as the total length to wavelength ratio $2h/\lambda$ [31].

The input impedance, Z_{in}, is a function of frequency and can be expressed as the ratio of two polynomials, where the zeros of the numerator are the zeros of the impedance function and the zeros of the denominator are its poles. It can be understood from the typical frequency behavior of Z_{in} of a dipole antenna, that there exist a pole at $f = 0$ which can be modeled by a capacitor C_0. At higher frequencies, this capacitor will be short-circuited and a series inductor, L_0, can be considered instead. In fact, up to the first resonance, the graph of the input impedance looks very similar to a cascaded network of RLC resonant circuits, where R is the radiation resistance. Considering the length of the dipole antenna in the range of $0 < 2h/\lambda < 2$, our equivalent circuit consists of three series impedances,

Z_0, Z_1 and Z_2, which is shown in Fig. 5.1. So the input impedance Z_{in} can be written as:

$$Z_{\text{in}} = Z_0 + Z_1 + Z_2 \tag{5.1a}$$

$$Z_0 = \frac{1}{j\omega C_0} + j\omega L_0 \tag{5.1b}$$

$$Z_1 = \frac{j\omega R_1 L_1}{j\omega L_1 + R_1(1 - \omega^2 L_1 C_1)} \tag{5.1c}$$

$$Z_2 = \frac{j\omega R_2 L_2}{j\omega L_2 + R_2(1 - \omega^2 L_2 C_2)}. \tag{5.1d}$$

Fig. 5.2 shows the input impedance Z_{in} versus f for a center-fed cylindrical dipole with $2h/a = 1808$, where a is the radius of the antenna wire. Depending on the length of the dipole in wavelengths, the number of parallel RLC networks can be determined and is related to the number of resonances [31].

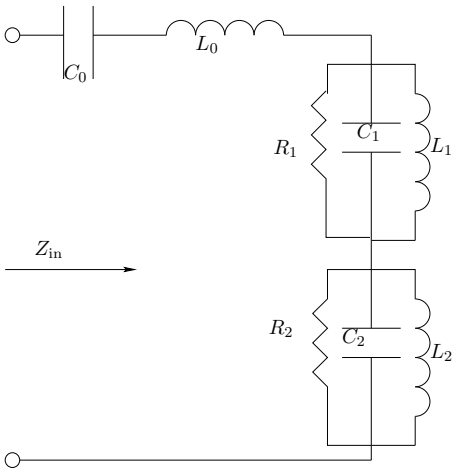

Figure 5.1: Input impedance of a center-fed dipole antenna for $0 < 2h/\lambda < 2$ [31].

5.3 Padé Approximation Theory

As shown in the previous section, the input impedance $Z_{\text{in}}(f)$ of a dipole antenna can be written as a ratio of two polynomials. Based on this knowledge, we can use the Padé rational function fitting model as a natural curve fitting technique exploiting the physics of the problem [30]. This technique employs two low-order analytical formulas as fitting models, while the coefficients of these fitting models are obtained numerically by matching

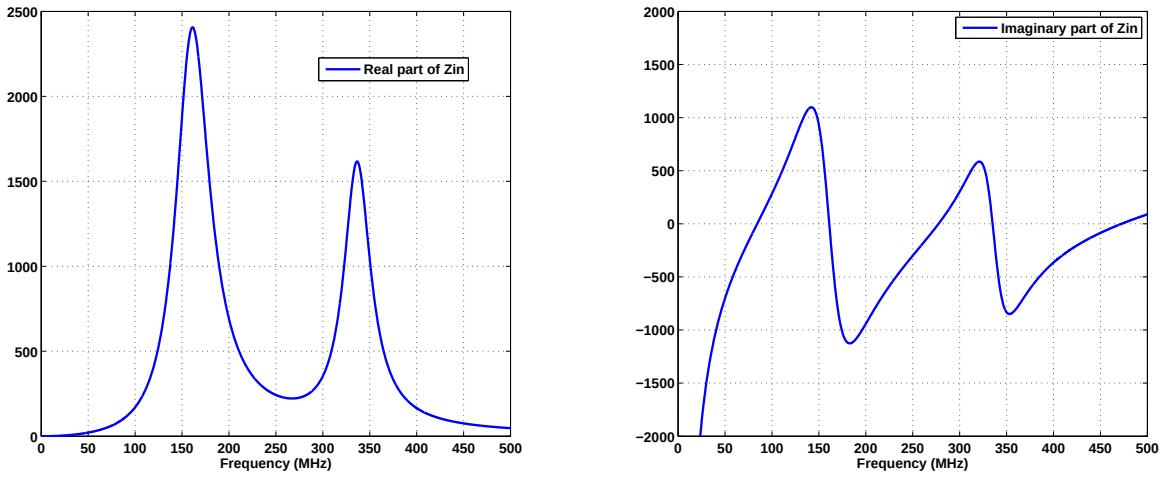

Figure 5.2: Input impedance model of a center-fed dipole antenna for $0 < 2h/\lambda < 2$, $L_0 = 0.196$ μH, $C_0 = 3.149$ pF, $R_1 = 2400$ Ω, $L_1 = 0.645$ μH, $C_1 = 1.51$ pF, $R_2 = 1550$ Ω, $L_2 = 0.0752$ μH, $C_2 = 2.972$ pF.

them to the sampled values. One form of these fitting models used by the MBPE is represented by:

$$F(f) = \frac{N(f)}{D(f)} = \frac{N_0 + N_1 f^1 + N_2 f^2 + ... + N_n f^n}{D_0 + D_1 f^1 + D_2 f^2 + ... + D_{d-1} f^{d-1} + f^d}. \tag{5.2}$$

Here, $F(f)$ represents a fitting model in the spectral-domain which is suitable for interpolation of complex data sets. This function has $n+d+1$ unknown complex-valued coefficients. If $F(f)$ is sampled at N_f frequencies, a matrix equation can be obtained as

$$\mathbf{A}\mathbf{x} = \mathbf{b} \tag{5.3}$$

where $\mathbf{A}$, $\mathbf{x}$ and $\mathbf{b}$ are given as

$$\mathbf{b} = \begin{bmatrix} F(f_1)f_1^d & F(f_2)f_2^d & \cdots & F(f_{N_f})f_{N_f}^d \end{bmatrix}^T \tag{5.4a}$$

$$\mathbf{A} = \begin{bmatrix} 1 & f_1 & \cdots & f_1^n & -F(f_1) & -F(f_1)f_1 & \cdots & -F(f_1)f_1^{d-1} \\ 1 & f_2 & \cdots & f_2^n & -F(f_2) & -F(f_2)f_2 & \cdots & -F(f_2)f_2^{d-1} \\ \vdots & \vdots & \vdots & \vdots & \vdots & \vdots & \vdots & \vdots \\ 1 & f_{N_f} & \cdots & f_{N_f}^n & -F(f_{N_f}) & -F(f_{N_f})f_{N_f} & \cdots & -F(f_{N_f})f_{N_f}^{d-1} \end{bmatrix} \tag{5.4b}$$

and the matrix of unknown coefficients is given as

$$\mathbf{x} = \begin{bmatrix} N_0 & N_1 & \ldots & N_n & D_0 & D_1 & \ldots & D_{d-1} \end{bmatrix}^T. \tag{5.5}$$

After solving $\mathbf{x}$, (5.2) can be used to interpolate the input impedance at any other frequency within the modeled frequency interval.

5.3.1 Numerical Results

In this section the Padé approximation method is applied to the structure of two monopole antennas with a row of pins in between. This is the same structure analyzed before in Chapter 4 using the method of moments. The 2×2 input impedance matrix of this structure can be computed using the numerical method of moments (MoM) as implemented in the CAESAR software. Here, we experimented with different values for the denominator order, d, and the number of sampling points, N_f, over the frequency range of 10–60 GHz to observe the performance of the rational function fitting model. Toward this end, we first studied the condition number of the matrix $\mathbf{A}$ as computed through the Padé rational function method. The condition number can be considered as a measure for the rate at which the solution $\mathbf{x}$ will change relative to a change in $\mathbf{b}$. It means that for a large condition number, a small error in $\mathbf{b}$ may lead to a large error in $\mathbf{x}$.

In Fig. 5.3, we can see that the condition number of the matrix $\mathbf{A}$ is increasing for a larger number of sampling points, while the model is better fit for higher N_f. In fact, in Fig. 5.4, it can be seen that the best fitting model is achieved for the largest number of frequency samples, when compared to the reference data obtained from our numerical MoM code.

5.4 Adaptive Frequency Sampling

One important aim of most numerical modeling methods is to minimize the computation time, while reaching a desired solution accuracy, for instance by minimizing the number of frequency samples needed to estimate the frequency response of a system. The adaptive estimation is used here in the context of computing the input impedance of a radiating structure. The particular goal is to minimize the number of required frequency samples while achieving an accurate representation of the input impedance characteristics.

The herein proposed adaptive frequency sampling approach makes use of the above-described model-based parameter estimation (MBPE). However, rather than sampling at regularly-

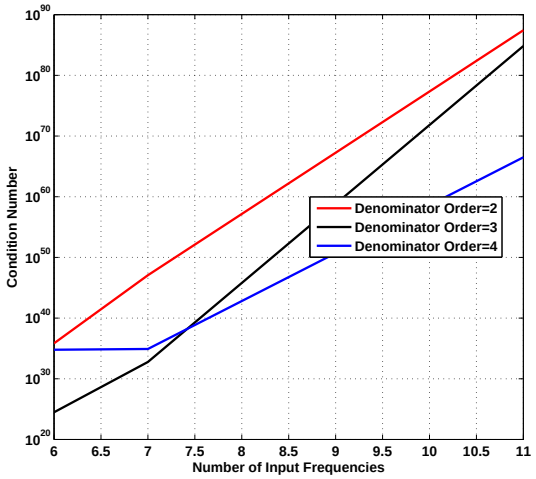

Figure 5.3: Condition number of the matrix **A** versus N_f, for denominator orders 2, 3 and 4.

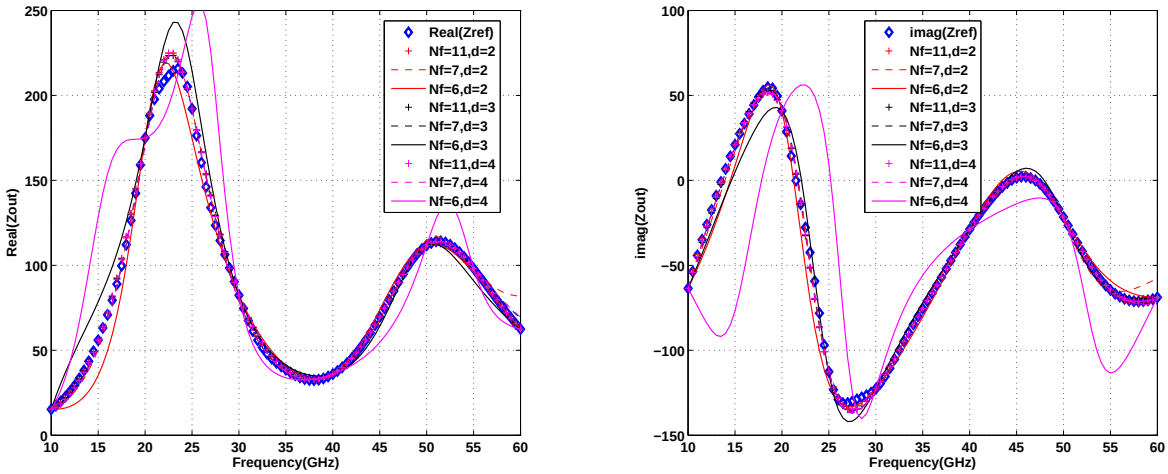

Figure 5.4: A Comparison of $\mathrm{Re}(Z_{\mathrm{in}})$ and $\mathrm{Im}(Z_{\mathrm{in}})$ for the structure of two monopole antennas in a waveguiding region computed using the MoM and a Padé approximation, for denominator orders 2, 3 and 4 and $N_f \in \{6, 7, 11\}$.

spaced frequency intervals, the sampling is performed adaptively to minimize the total number of required frequency samples [33]. The frequency sample to be selected next is determined through an iterative process as described below.

The adaptive process starts with two frequency samples in the desired bandwidth – typ-

ically the first and the last one – whose corresponding input impedances are computed beforehand. Since rational functions are suitable for approximating the impedance characteristics, we make use of the Padé approximation to model these characteristics based on the few input sampling points. Each time a new frequency point is added to the previous set of frequency points, the Padé approximation will find a rational function for modeling the impedance. Afterwards, the difference between this newly generated fitting model and the previous one is computed for all frequency points in our desired bandwidth. The frequency where the maximum of the relative difference is occurring, is considered as the new frequency point, provided it is not included in the list of already selected frequencies. This adaptive process continues until the norm of the error vector pertaining to all frequencies of interest, is less than a specified estimation error. Another goal that should be considered to terminate this adaptive frequency sampling process is the ill-conditioning of the matrix $\mathbf{A}$ which might occur in the generation of rational-function fitting models [34].

The generalization to input impedance matrices is straightforward, since the above-described MBPE methodology is applied successively and independently for all of the matrix elements, however, the next frequency to be selected follows from the largest change in matrix norms (involving all the matrix elements) of the estimated and previously estimated impedance matrix, so that the frequency sampling points are the same for all matrix elements.

5.4.1 Numerical Results

In this section we apply the adaptive MBPE method, first to the dipole antenna whose equivalent circuit parameters have been extracted in Sec. 5.2, over the frequency range of $0 - 600$ MHz. For the sake of comparison, we use the sampled data calculated from the equivalent circuit model in (5.1). The rational function used for the Padé approximation is of the same type as the one given in (5.2), which only depends on frequency. The initial two frequency points are selected as the first and the last points in the frequency range $0 - 600$ MHz. The third frequency point is selected in the middle of this range, after which the adaptive frequency sampling process continues until the maximum error between two successive rational-function fitting models is less than a specified estimation error, which is chosen to be 10^{-2} in this case. As a result, the final obtained rational function has a denominator of order $d = 6$ and a numerator of order $n = 5$, for a total number of

fitting frequencies $N_f = 12$ (see Fig. 5.5). The final obtained maximum relative error is 1.4203×10^{-4} and the final condition number of $\mathbf{A}$ is 3.1×10^{47}.

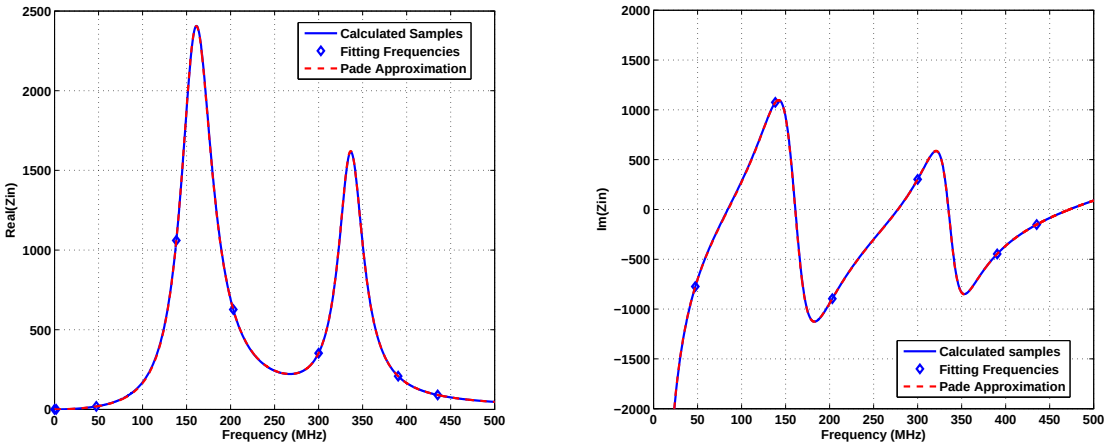

Figure 5.5: A comparison of $\mathrm{Re}(Z_{\mathrm{in}})$ and $\mathrm{Im}(Z_{\mathrm{in}})$ for the center-fed dipole antenna, computed using an equivalent circuit model and the Padé approximation. The sampled frequencies are shown in the plots by markers.

In the second example, we employ the adaptive frequency sampling for the analysis of two monopole antennas in a waveguide region through the CAESAR software (see Fig. 4.3). Since two radiators are present, a 2×2 input impedance matrix is computed for each frequency point. However, due to the symmetrical properties of the structure, one only needs two rational function fitting models in the adaptive sampling process, i.e. for the Z_{11} and Z_{12} elements over the frequency range of $10 - 60$ GHz. As observed above, the more is the number of output frequencies, the better is the accuracy of the models, but the higher is the matrix condition number for computing the polynomial coefficients of the rational functions. It is observed that a better fitting model is given by increasing the upper limit of the final condition number. The adaptive sampling process continues until the limit for the maximum condition number is reached.

Fig. 5.6 shows the case when the impedance is evaluated directly at 51 frequency sampling points, and when approximated by the Padé method using only $N_f = 11$ samples. The final condition number in the adaptive process is in the range of 10^{55}, and the total number of selected frequencies in the adaptive process is $N_f = 11$. For comparison, when the number of output frequencies is increased to 101, the final condition number is about 10^{78} and the total number of fitting frequencies is $N_f = 16$. The real and imaginary parts of the Z_{11}

and Z_{12} matrix elements for these two cases, which are estimated by the adaptive sampling process in conjunction with the MoM, are shown in Fig. 5.6 and 5.7.

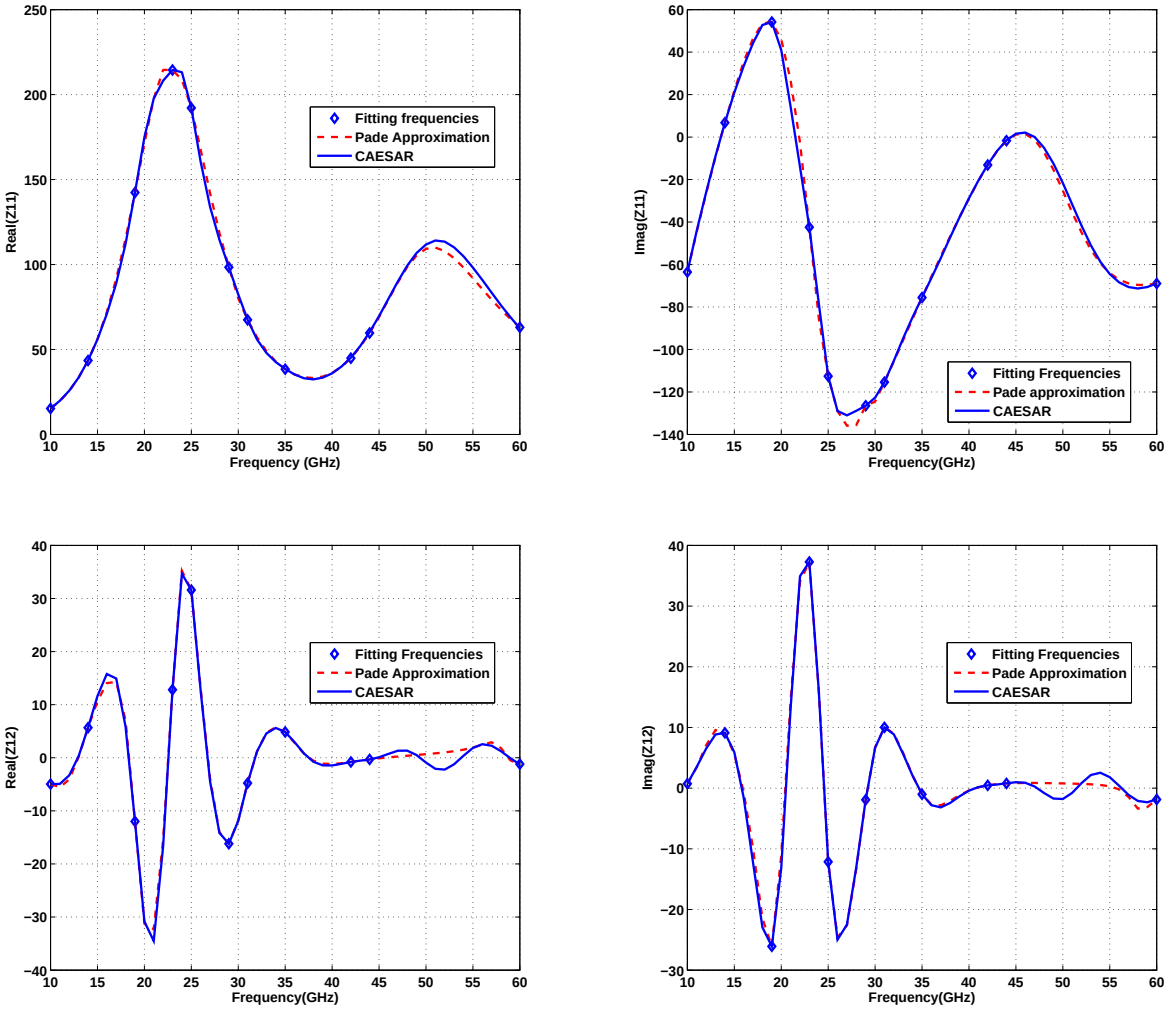

Figure 5.6: Adaptive frequency sampling approach for the Padé approximation of the impedance matrix elements of the two-monopole antenna structure in a waveguiding region (Fig. 4.3), the impedance is evaluated for 51 points, while 11 were used for the adaptive sampling.

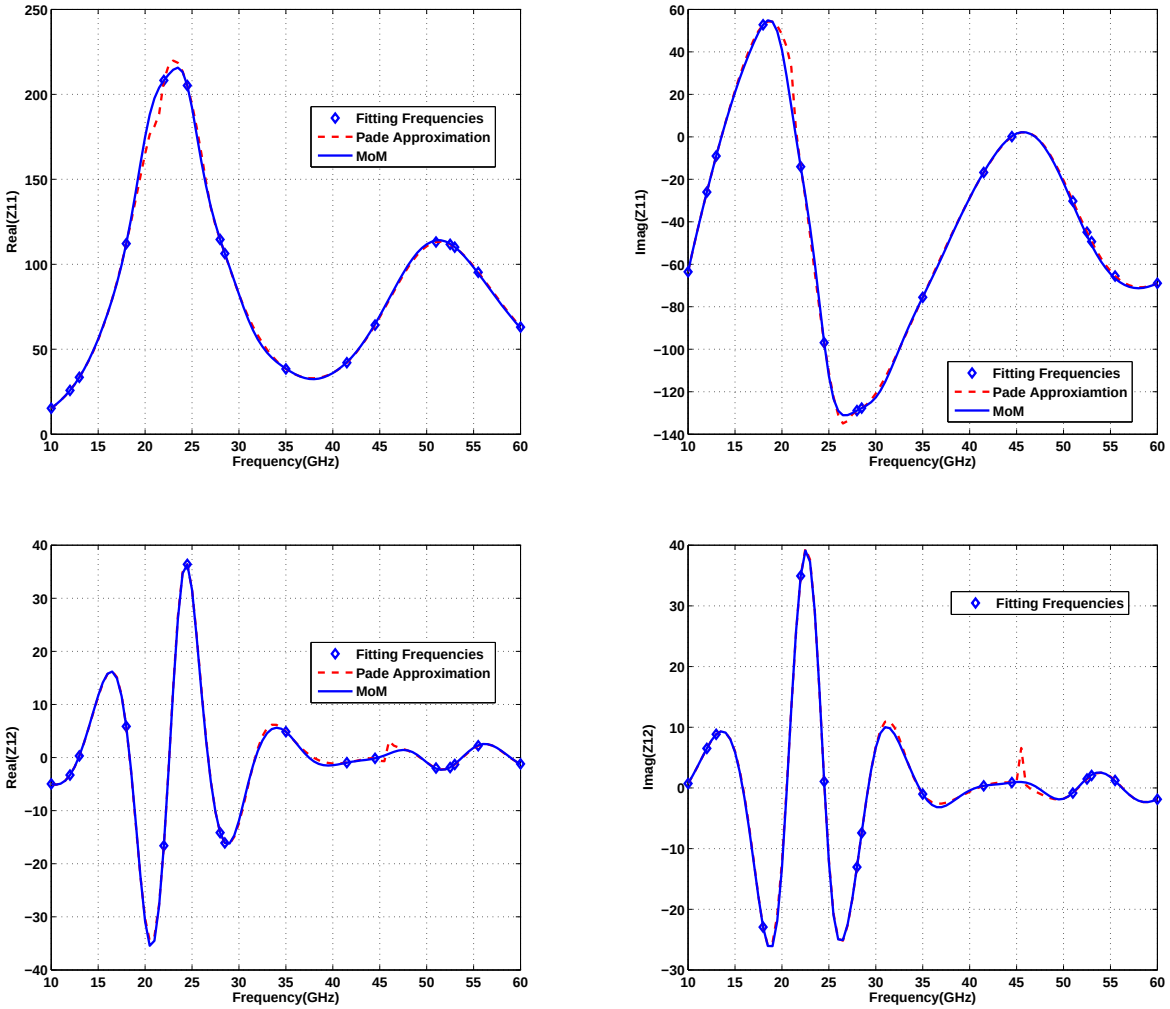

Figure 5.7: Adaptive frequency sampling approach for the Padé approximation of the impedance matrix elements of the two-monopole antenna structure in a waveguiding region (Fig. 4.3), the impedance is evaluated for 101 points, while 16 were used for the adaptive sampling.

5.5 Conclusion

In this chapter we studied the Padé rational function fitting model to predict the input impedance of an antenna at any given frequency within the modeled frequency bandwidth. The selection of this type of curve fitting approach is motivated by an analytical expression for the input impedance of a center-fed dipole antenna. Accordingly, the Padé approxima-

tion has been applied to a parallel-plate waveguiding structure of two monopole antennas, with a row of pins in between. In our study, different values for the frequency sampling points and orders of polynomial functions have been selected. Furthermore, the adaptive frequency sampling has been introduced for minimizing the number of samples required to represent the impedance characteristics by rational function for achieving a desired accuracy. Finally, the herein developed adaptive frequency-response estimation technique has been applied to a center-fed dipole antenna as well as the parallel-plate waveguiding structure excited by two monopoles.

Chapter 6

Characteristic Basis Function Method

In this chapter, we describe a numerically efficient technique to solve an electrically large groove gap waveguiding structure. This technique, which is called Characteristic Basis Function Method (CBFM), employs macro-domain basis functions that are herein referred to as Characteristic Basis Functions (CBFs). In this work, the CBFs are supported by a relatively large number of sub-domains that are discretized by triangular patches. The CBFM reduces the matrix size of conventional MoM approaches by $2-3$ orders. Furthermore, the CBFM has been hybridized with a technique called the Adaptive Cross Approximation algorithm (ACA), to shorten the fill-time of the resulting reduced matrix of equation.

6.1 Introduction

The electromagnetic analysis of large antennas and scattering problems has been an important research direction. Conventional integral equation solvers that are based on the method of moments (MoM) can handle electromagnetic problems of arbitrary shapes by employing subsectional basis functions supported on local subdomains. However, to obtain an accurate solution in the analysis of the large structures using these type of solvers, we need to discretize the object using basis function for the current of size $\lambda/10$ to $\lambda/20$, which in turn leads to a large matrix equation.

One solution to reduce the size of the matrix equation for large scale problems is to employ macro basis and test functions. These macro-domain functions can be expressed in terms of a fixed combination of subsectional basis functions to conform to the shape of arbitrarily shaped geometries. These types of macro basis functions have been applied before to arrays of disconnected patch antennas in [35], where the entire computational domain is subdivided into blocks, each of which supports a set of basis functions. This approach of breaking down the problem into smaller subproblems, has also been used in the recently proposed iterative-free methods for large scale problems, the Characteristic Basis Function Method (CBFM) [36], the Sub-Entire-Domain Basis Function Method (SED) [37], and the eigencurrent approach [38]. The aim of all these methods is to reduce the size of the matrix equation by utilizing macro basis functions for the electric or magnetic surface currents. In turn, this leads to significant savings in memory and computation time.

In the present description of CBFM we employ an overlapping domain decomposition method, since some subdomains can be electrically interconnected to each other. In these problems, the CBFs partially overlap to preserve the continuity of the surface current across interconnecting boundaries, thereby avoiding spurious radiation from artificial discontinuities by the current at common interfaces. More details on the subdomain selection and generation of partially-overlapping CBFs can be found in [22, Chapter. 4].

In this chapter, the CBFM is used to analyze a groove gap waveguide structure. Besides reducing the size of the matrix equation by CBFM, we have to find a way to rapidly construct the reduced matrix equation. Although the matrix fill-time scales with N^2, where N is the number of subsectional basis functions making up the K CBFs, the solve time scales with K^3, however the time it takes to fill the reduced matrix is still of great importance, since $K \ll N$. There exist a number of hybrid methods to reduce the matrix fill-time, such as Fast Multipole Method (FMM) [39] and the Adaptive Integral Method (AIM) [40]. In the current approach, the reduced matrix is generated by a combination of the CBFM and the Adaptive Cross Approximation (ACA) algorithm. The ACA algorithm, which is developed to exploit the low-rank properties of moment matrix blocks, is also applicable to the fast computation of reaction integrals between macro-domain source and test functions [41].

6.2 Entire-Domain Basis Function Method

Consider a domain $\mathcal{S}$ which represents the support of the surface current $\boldsymbol{J}_{\mathcal{S}}$ formed by the conducting surfaces inside the gap waveguide; in this specific case by the pins and coaxial probes only. The current $\boldsymbol{J}_{\mathcal{S}}$ can be found by solving an integral equation for the electric field and current at the boundary surface $\mathcal{S}$, i.e. [see Eq. (4.5)],

$$-\boldsymbol{E}^{\mathrm{i}}_{\tan} = \boldsymbol{E}^{\mathrm{s}}_{\tan}\left(\boldsymbol{J}_{\mathcal{S}}\right) - Z_{\mathcal{S}}\boldsymbol{J}_{\mathcal{S}}, \qquad \text{for} \quad \boldsymbol{r} \in \mathcal{S} \tag{6.1}$$

where $\boldsymbol{E}^{\mathrm{i}}$ is the impressed incident electric field, $\boldsymbol{E}^{\mathrm{s}}\left(\boldsymbol{J}_{\mathcal{S}}\right)$ is the scattered electric field caused by the source current $\boldsymbol{J}_{\mathcal{S}}$, and $Z_{\mathcal{S}}$ is the surface impedance of the conducting support. The scattered electric field is computed by using Eq. (2.3), where ϕ and $\boldsymbol{A}$ are the electric scalar potential and magnetic vector potential, respectively.

In the CBFM-enhanced MoM for solving (6.1), we first divide the domain $\mathcal{S}$ into L smaller subdomains, each of which supports a set of macro-domain basis functions. These supports generally overlap with each other if there exists an electrical connection between them. Using the same set of entire-domain basis and test functions for the discretization of the EFIE in (6.1), a matrix equation is obtained of the form

$$\mathbf{ZI} = \left(\mathbf{Z}^{\mathrm{PEC}} - \mathbf{Z}^{\mathrm{IBC}}\right)\mathbf{I} = \mathbf{V} \tag{6.2}$$

where the element Z^{PEC}_{pq} is the reaction of the macro basis function $\boldsymbol{J}_q$ on the macro test function $\boldsymbol{J}_p$, that is,

$$Z^{\mathrm{PEC}}_{pq} = \iint\limits_{\mathcal{S}_p} \boldsymbol{E}^{\mathrm{s}}\left(\boldsymbol{J}_q\right) \cdot \boldsymbol{J}_p \mathrm{d}S \tag{6.3}$$

and the pth source term V_p is computed as

$$V_p = -\iint\limits_{\mathcal{S}_p} \boldsymbol{E}^{\mathrm{i}}\left(\boldsymbol{r}\right) \cdot \boldsymbol{J}_p \mathrm{d}S \tag{6.4}$$

where $\mathcal{S}_p$ is the pth subdomain supporting the current $\boldsymbol{J}_p$. In this chapter, it is assumed that the supporting surface is a perfect electric conductor with $Z_{\mathcal{S}} = 0$, so the element Z^{IBC}_{pq}, which is dependent upon this value, is zero for all p, q [22, Sec. 4.2].

6.3 The Characteristic Basis Function Method

6.3.1 Employing Characteristic Basis Functions

The Characteristic Basis Functions (CBFs), which are the macro basis and test functions in CBFM, are generated numerically by combining the low-level basis functions on the corresponding subdomain. On each subdomain we employ the RWG (Rao-Wilton-Glisson) basis functions as the low-level basis functions that have been introduced in Chapter 4. The CBF on the ith subdomain can be expanded as

$$\boldsymbol{J}_i(\boldsymbol{r}) = \sum_{m=1}^{N_i} I_m^i \boldsymbol{f}_m^i(\boldsymbol{r}) \tag{6.5}$$

where $\boldsymbol{f}_m^i$ denotes the mth RWG on the ith subdomain and I_m^i are the expansion coefficients for modeling the shape of the CBF on the ith subdomain. Substituting (6.5) in (6.3) results in

$$Z_{pq}^{\mathrm{PEC}} = \sum_{m=1}^{N_p}\sum_{n=1}^{N_q} I_m^p \left[\iint\limits_{\mathcal{S}_p} \boldsymbol{E}^{\mathrm{s}}\left(\boldsymbol{f}_n^q\right)\cdot \boldsymbol{f}_m^p \mathrm{d}S\right] I_n^q = \mathbf{J}_p^T \mathbf{Z}_{pq}^{\mathrm{RWG}} \mathbf{J}_q. \tag{6.6}$$

Here, $\mathbf{Z}_{pq}^{\mathrm{RWG}}$ is a rectangular matrix of size $N_p \times N_q$, where the subscripts p and q are used for the observation and source CBFs, respectively.

For electrically large subdomains, we need to have a large and linearly independent set of CBFs on each subdomain. At this point it is assumed that the number of CBFs on the pth and qth subdomains are K_p and K_q respectively. Then, instead of (6.6), we have $\mathbf{Z}_{pq}^{\mathrm{CBF}} = \mathbf{J}_p^T \mathbf{Z}_{pq}^{\mathrm{RWG}} \mathbf{J}_q$, where $\mathbf{Z}_{pq}^{\mathrm{RWG}}$ is a $K_p \times K_q$ rectangular matrix block. The matrix $\mathbf{J}_q$ is of size $N_q \times K_q$ and holds the expansion coefficients of the CBFs on the qth subdomain, while $\mathbf{J}_p$ is of size $N_p \times K_p$ and corresponds to the pth subdomain. Hence, $\mathbf{Z}^{\mathrm{CBF}}$ in the reduced matrix equation $\mathbf{Z}^{\mathrm{CBF}}\mathbf{I}^{\mathrm{CBF}} = \mathbf{V}^{\mathrm{CBF}}$ has a block-type structure. That is, when the total domain has been divided into L subdomains [22, Sec. 4.3],

$$\begin{bmatrix} \mathbf{J}_1^T\mathbf{Z}_{11}^{\mathrm{RWG}}\mathbf{J}_1 & \mathbf{J}_1^T\mathbf{Z}_{12}^{\mathrm{RWG}}\mathbf{J}_2 & \dots & \mathbf{J}_1^T\mathbf{Z}_{1L}^{\mathrm{RWG}}\mathbf{J}_L \\ \mathbf{J}_2^T\mathbf{Z}_{21}^{\mathrm{RWG}}\mathbf{J}_1 & \mathbf{J}_2^T\mathbf{Z}_{22}^{\mathrm{RWG}}\mathbf{J}_2 & \dots & \mathbf{J}_2^T\mathbf{Z}_{2L}^{\mathrm{RWG}}\mathbf{J}_L \\ \vdots & \vdots & \ddots & \vdots \\ \mathbf{J}_L^T\mathbf{Z}_{L1}^{\mathrm{RWG}}\mathbf{J}_1 & \mathbf{J}_L^T\mathbf{Z}_{L2}^{\mathrm{RWG}}\mathbf{J}_2 & \dots & \mathbf{J}_L^T\mathbf{Z}_{LL}^{\mathrm{RWG}}\mathbf{J}_L \end{bmatrix} \begin{bmatrix} \mathbf{I}_1^{\mathrm{CBF}} \\ \mathbf{I}_2^{\mathrm{CBF}} \\ \vdots \\ \mathbf{I}_L^{\mathrm{CBF}} \end{bmatrix} = \begin{bmatrix} \mathbf{V}_1^{\mathrm{CBF}} \\ \mathbf{V}_2^{\mathrm{CBF}} \\ \vdots \\ \mathbf{V}_L^{\mathrm{CBF}} \end{bmatrix}. \tag{6.7}$$

6.3.2 Generation of Characteristic Basis Functions

In this section, the proposed procedure for generating the CBFs for a groove gap waveguide is explained and involves the following steps:

Mesh Construction

To increase the speed of the mesh generation for the whole structure, the meshing is performed for only two user-defined building blocks, i.e., for one pin and one coaxial probe; the generated mesh is then replicated at different pin positions throughout the whole array by exploiting translation symmetry. After collecting and aggregating the meshed blocks, the coinciding nodes are removed and RWGs and triangle nodes are renumbered. Finally, to realize an electrical connection between blocks, connection RWGs across common boundaries are generated. This specific way of mesh generation also facilitates the mapping process of CBFs, so that many identical reaction integrals exist between source and observation CBF pairs, as a result of which a large number of the reduced matrix element are the same. In Fig. 6.1 the structure of a entirely meshed groove gap waveguide is shown.

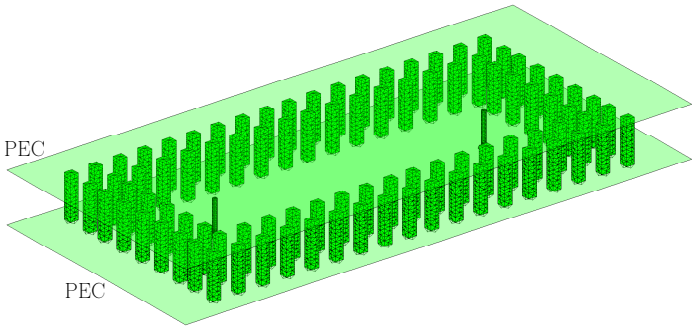

Figure 6.1: Coaxial-probe excited groove gap waveguide.

Numerical Generation of Primary CBFs

The first step in the generation of the CBFs is to extract subdomains from the entirely meshed structure. In the present structure of the groove gap waveguide, there are two coaxial probes for excitation purposes and one periodic texture of pins to realize a high impedance surface. Since each pin is surrounded by other pins, the primary CBFs on each pin can be generated by a spectrum of plane waves incident from different directions, while the single primary CBF on a coaxial probe is generated due to its own excitation by the magnetic frill current and the plane wave spectrum (PWS). As an example, consider Fig. 6.2, where the CBFs are generated for only one of the pins. Here, each pin consists of 382 RWGs. A PWS is incident on the pin with $\Delta\theta^{\mathrm{i}} = \Delta\phi^{\mathrm{i}} = 90^0$ (and two polarizations). This generates an initial set of CBFs, i.e., the columns of the matrix $\boldsymbol{J}$ holding the RWG expansion coefficient vectors. Afterwards, the SVD is invoked on $\boldsymbol{J}$ with an appropriate thresholding procedure on its singular values to retain only a few left-singular vectors as the CBFs. This is explained below in more detail.

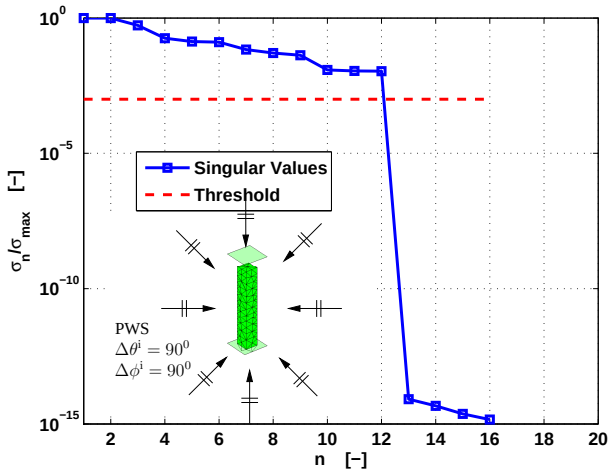

Figure 6.2: Generation of CBFs on a pin using a plane wave spectrum (PWS). The singular value spectrum is shown where a threshold is used to limit the maximum number of employed CBFs.

In Fig. 6.3, the first and secondly generated CBFs on one of the pins and the excitation probes are shown. Assuming that the current $\boldsymbol{J}_{\mathrm{pin},\ell}$ on the ℓth pin is written as a summation

of N_{pin} RWG basis functions

$$\boldsymbol{J}_{\text{pin},\ell}(\boldsymbol{r}) = \sum_{m=1}^{N_{\text{pin}}} I_m^{\text{pin},\ell} \boldsymbol{f}_m^{\text{pin},\ell}(\boldsymbol{r}) \tag{6.8}$$

where $\{I_1^{\text{pin},\ell}, I_2^{\text{pin},\ell}, ..., I_N^{\text{pin},\ell}\}$ are the corresponding pin RWG expansion coefficients. These coefficients are given by solving the matrix equation for that subdomain, i.e.,

$$\mathbf{J}_{\text{pin},\ell} = \mathbf{Z}_{\text{pin},\ell}^{-1} \mathbf{V}_{\text{pin},\ell}. \tag{6.9}$$

Here, $\mathbf{V}_{\text{pin},\ell}$ is the excitation matrix for the plane wave spectrum and $\mathbf{Z}_{\text{pin},\ell}$ is the moment matrix for the RWGs on the ℓth pin.

Reducing the Number of CBFs

To obtain a reduced moment matrix with a sufficiently low condition number, we need to make sure that the CBFs in each of the subdomains are linearly independent. The SVD operation renders the CBFs orthogonal so as to assure a well-conditioned moment matrix. For example, the matrix $\mathbf{J}_q$, which is of size $N_q \times K_q$, where N_q is the number of RWGs and K_q is the number of CBFs on the qth subdomain, is typically rank-deficient. One proper tool for controlling the effective rank of this matrix, is application of the Singular Value Decomposition (SVD). After the SVD operation, where a thresholding procedure is applied on the singular values, $\mathbf{J}_q$ can be written as

$$\mathbf{J}_q = \mathbf{U}\mathbf{D}\mathbf{Q}^H \tag{6.10}$$

where $\mathbf{U}$ is an $N_q \times K_q$ matrix; $\mathbf{Q}$ is a unitary matrix of size $K_q \times K_q$ and $\mathbf{D}$ is a $K_q \times K_q$ diagonal matrix with the entries $[\sigma_1, \sigma_2, ..., \sigma_{K_q}]$ on the main diagonal. These diagonal entries are the singular values of the matrix $\mathbf{J}_q$. To avoid that the columns of $\mathbf{J}_q$ are linearly dependent, all the normalized and ordered singular values are compared to an appropriate threshold, and those that are smaller than the threshold are set to zero. In Fig. 6.4, the magnitude of the normalized singular values in $\mathbf{D}$ are plotted for a pin. With an appropriate thresholding procedure on the singular values, only the first 12 column vectors of the matrix $\mathbf{U}$ are retained and subsequently employed as CBFs to model the current on a pin. The thresholding process on the singular values for a coaxial probe is also shown in Fig. 6.4 (where the threshold is 10^{-3}). As a result, the number of retained orthonormal CBFs for the coaxial probe is only 3.

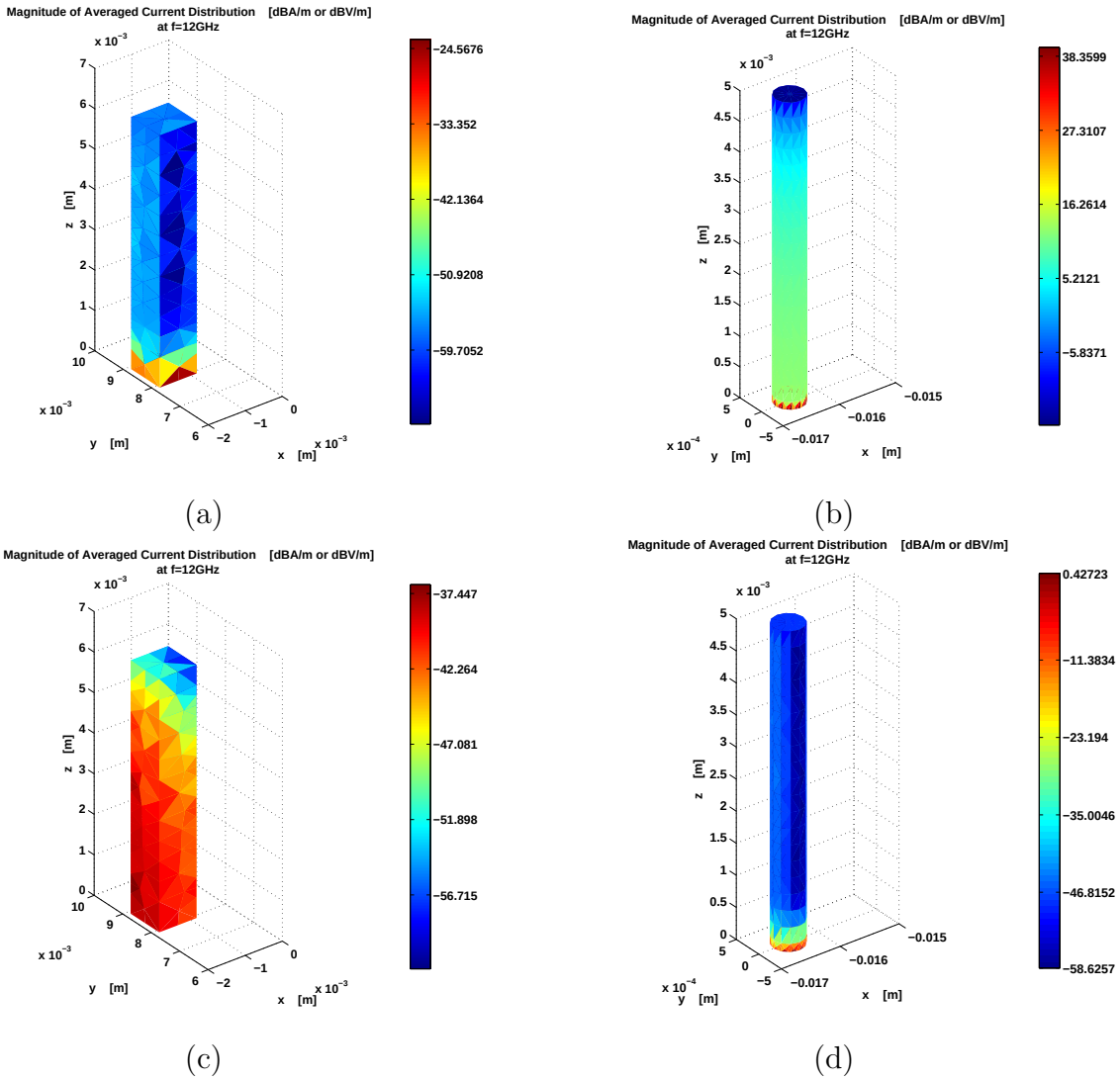

Figure 6.3: On the left: first and secondly generated CBFs on a pin, On the right: first and secondly generated CBFs on a coaxial probe, at a frequency of 12 GHz.

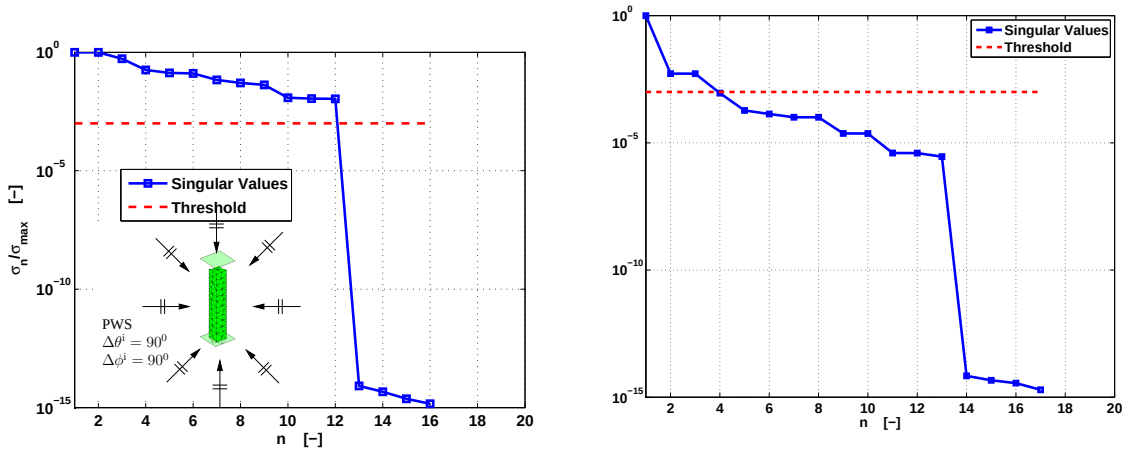

(a) (b)

Figure 6.4: SVD operation on a defined block of a) pin and b) coaxial probe, with SVD threshold of 0.001, at f=12GHz.

Generation of Secondary CBFs

To achieve a more exact solution for the final surface current, the number of CBFs in each subdomain can be increased. Toward this end, the primary CBFs $\mathbf{J}_q$, which are supported by the qth subdomain, can be considered as distant sources relative to the subdomain under consideration; these primary CBFs could represent surface currents that exist on neighboring subdomains located some distance away. For example, for the groove gap waveguide, secondary CBFs are generated on each pin due to distant neighboring pins. We choose not to generate secondary CBFs on coaxial probes, since this may not be needed as the current on the probe is single-mode dominated. A plane wave spectrum in addition to the self-excitation therefore suffices. For the currents on a pin we then have

$$\mathbf{J}_{\text{pin},\ell} = \mathbf{Z}^{-1}_{\text{pin},\ell}\mathbf{V}_{\text{pin},\ell} = \mathbf{Z}^{-1}_{\text{pin},\ell}\mathbf{Z}_{\text{pin},\ell,q}\mathbf{J}_{\text{pin},\ell,q} \tag{6.11}$$

where $\mathbf{Z}_{\text{pin},\ell,q}$ is the moment matrix block for reactions between RWGs on the qth source pin supporting the primary CBFs and the RWGs on the ℓth pin under consideration. After considering several distant current sources surrounding the ℓth pin, we add this newly generated secondary CBFs, $\mathbf{J}_{\text{pin},\ell}$, to the current set of primary CBFs. Again, we apply the SVD to this combined set of primary and secondary CBFs, which leads to a reduced and orthonormalized set of CBFs.

Mapping of CBFs

Now that a reduced set of CBFs has been determined for one pin and one coaxial probe, we map the CBFs onto the completely meshed groove gap waveguide. After this mapping, the entire structure supports CBFs. Afterwards, a reduced matrix equation is generated which will be solved directly without the need to use iterative methods.

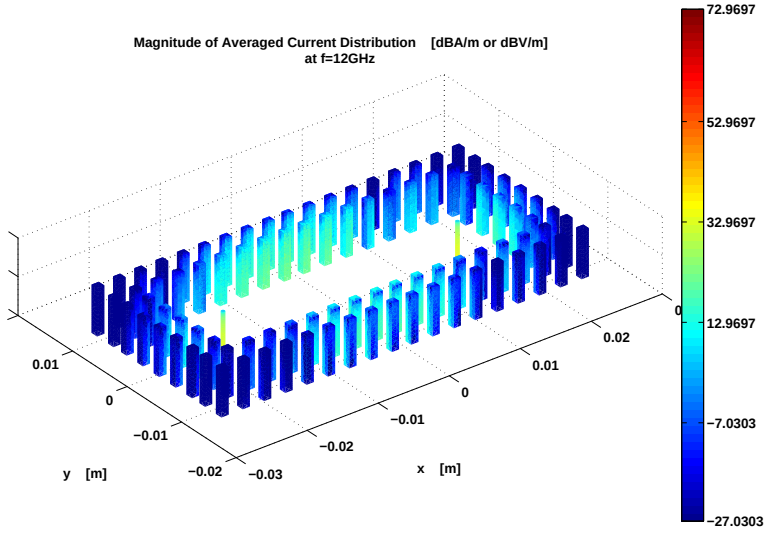

Figure 6.5: The synthesized surface current on the entirely meshed structure of the groove gap waveguide.

6.3.3 Translation Symmetry

One can exploit the translation symmetry that exists of the reactions between sets of CBFs on subdomains, so that the reduced moment matrix is generated in a more efficient way. For example, if the two matrix blocks $\mathbf{Z}_{pq}^{\mathrm{CBF}}$ and $\mathbf{Z}_{p+1;q+1}^{\mathrm{CBF}}$, which hold the reaction integrals between sets of CBFs, are equal, it means that

$$\mathbf{Z}_{pq}^{\mathrm{CBF}} = \mathbf{J}_p^T \mathbf{Z}_{pq}^{\mathrm{RWG}} \mathbf{J}_q = \mathbf{Z}_{p+1;q+1}^{\mathrm{CBF}} = \mathbf{J}_p^T \mathbf{Z}_{p+1;q+1}^{\mathrm{RWG}} \mathbf{J}_q. \tag{6.12}$$

Note that, in order to be able to exploit translation symmetry, the separation distance between sets of CBFs, as well as the sets themselves must be identical.

6.3.4 Application of the ACA Algorithm

In direct methods, the total time to solve the reduced matrix equation scales with N^3, where N is the total number of basis functions. A great saving in solution time can be realized when N is the number of CBFs, which is typically $2-3$ orders smaller than the total number of RWGs. On the other hand, once the number of basis functions to solve for has been reduced, the construction time of the reduced matrix scales with the second power of the total number of RWGs and becomes the dominant contribution in the total solve time. To reduce the fill-time, translation symmetry in the groove gap waveguide can be exploited to rapidly fill the matrix by copying identical blocks. Also, due to reciprocity, only the upper triangular part of the matrix needs to be filled. The last significant time-saver is to approximate $\mathbf{Z}_{pq}^{\mathrm{RWG}}$ with its equivalent low-rank decomposition $\widetilde{\mathbf{Z}}_{pq}^{\mathrm{RWG}}$, so that

$$\mathbf{Z}_{pq}^{\mathrm{CBF}} = \mathbf{J}_p^T \mathbf{Z}_{pq}^{\mathrm{RWG}} \mathbf{J}_q \approx \mathbf{J}_p^T \widetilde{\mathbf{Z}}_{pq}^{\mathrm{RWG}} \mathbf{J}_q. \tag{6.13}$$

To compute $\widetilde{\mathbf{Z}}_{pq}^{\mathrm{RWG}}$, we propose to use the Adaptive Cross Approximation (ACA) technique, which is an adaptive algorithm to build subsets of source and observation RWGs, and performs an on-the-fly block factorization of the incomplete rank sub matrices. This method is entirely algebraic, so its implementation is not dependent on the kernel of the integral equation or type of basis functions; these properties facilitate the combination of this method with different MoM codes and increases the speed of the computational process [41]. It is pointed out that this algorithm is only used for totally separated subdomains which are rank-deficient, since the degree of rank deficiency of the submatrix $\mathbf{Z}_{pq}^{\mathrm{RWG}}$ depends on the size and electrical distance between the observation and source groups.

The block factorization of the approximate submatrix $\widetilde{\mathbf{Z}}_{pq}^{\mathrm{RWG}}$ is done by the ACA technique as

$$\widetilde{\mathbf{Z}}_{pq}^{\mathrm{RWG}} = \mathbf{U}_p^{N_p \times \mathrm{rk}} \mathbf{V}_q^{\mathrm{rk} \times N_q} = \sum_{i=1}^{\mathrm{rk}} \mathbf{u}_i^{N_p \times 1} \mathbf{v}_i^{1 \times N_q} \tag{6.14}$$

where rk represents the effective rank of the matrix $\widetilde{\mathbf{Z}}_{pq}^{\mathrm{RWG}}$. It is concluded that only $(N_p+N_q)\times\mathrm{rk}$ matrix elements need to be stored after the application of the ACA algorithm, which is a much smaller number than the total entries of the full matrix, which is $N_p \times N_q$.

$\mathbf{U}_p$ and $\mathbf{V}_q$ Generation in (6.14)

In the ACA algorithm in (6.14), the rectangular matrices $\mathbf{U}_p$ and $\mathbf{V}_q$ are constructed by the sequential selection of rows and columns of the matrix $\mathbf{Z}_{pq}^{\mathrm{RWG}}$. Also, an approximate error matrix is built, which is computed as $\|\widetilde{\mathbf{R}}\|_F = \|\mathbf{Z}_{pq}^{\mathrm{RWG}} - \widetilde{\mathbf{Z}}_{pq}^{\mathrm{RWG}}\|_F$, where $\|.\|_F$ is the Frobenius norm [42].

In each iteration of the ACA algorithm, after the selection of a row or column of the matrix $\mathbf{Z}_{pq}^{\mathrm{RWG}}$, this selected row or column is subtracted from the corresponding row or column in the approximate matrix obtained in the previous iteration. The selection of the next row or column depends on the location of the largest entry in the last computed error column or last computed error row. After terminating the iterative algorithm, the matrices $\mathbf{U}_p$ and $\mathbf{V}_q$ are composed, respectively, of successively computed column and row vectors.

To increase the speed of this method as compared to direct methods, the ACA algorithm is terminated after rk iterations, where rk is less than $\min(M, N)$, where $M \times N$ is the size of the original matrix $\mathbf{Z}_{pq}^{\mathrm{RWG}}$. This termination criterion can also be expressed as

$$\|\mathbf{R}\|_F \leq \epsilon \|\mathbf{Z}_{pq}^{\mathrm{RWG}}\|_F \tag{6.15}$$

where ϵ is a specified tolerance which controls the number of iterations and therefore the effective rank of $\mathbf{Z}_{pq}^{\mathrm{RWG}}$.

6.4 Results

6.4.1 Comparison of CBFM and HFSS for the groove gap waveguide analysis

In this section, the CBFM is applied for the fast analysis of a groove gap waveguide structure operating at 12 GHz. The geometrical dimensions are as described in Table 6.1. The radius and length of the coaxial probes are 0.25 and 5 mm, respectively, and the parallel-plate distance $d = 7.25$ mm.

The CBFM computations have been carried out on a 64 bit (x86-64) Linux – openSUSE

Table 6.1: Geometrical dimensions of the groove gap waveguide in [mm].

W_{pin}	H_{pin}	L_1	L_2	L_3	L_4
1	6.25	15.8	43.7	5.4	2

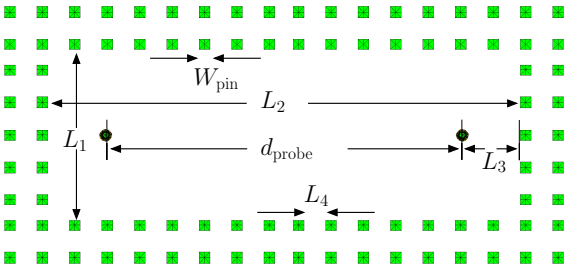

(v.11.4) server equipped with 2 Intel Xeon E5640 CPUs operating at 2.67 GHz (each CPU has 4 cores/8 threads), with access to 144 GB RAM memory and 2 TB harddisk space. The HFSS simulations were performed on a 64 bit Windows XP server equipped with 2 Intel Xeon 5130 CPUs operating at 2 GHz (each CPU has 2 cores/2 threads), 8 GB RAM, and 300 GB harddisk space.

As described in Section 6.3, the first step in the CBFM process is to rapidly generate and mesh the geometry. The efficient meshing for the whole structure starts with the meshing of two user-defined building blocks, i.e., of a pin and a coaxial probe, after which this mesh is copied onto the 94 blocks in the groove gap waveguide by using translation symmetry. This is followed by the process of collecting and integrating of the blocks to establish electrical interconnections. In the present structure of the groove gap waveguide there is no electrical connection between blocks, so there is no need to generate connection RWGs for this case. With reference to the final meshed geometry, Fig. 6.1, there exist a denser mesh on the coaxial probes as compared to the pins, which is due to rapidly changing field on the coaxial probes from the frill current.

The next step is to generate primary CBFs for two user-defined blocks. For the first block containing one pin, the total number of RWGs is 382. After generating the MoM matrix and computing the excitation vectors, the matrix equation for this block is solved through Gaussian elimination. The number of initially generated CBFs is 16, but after the SVD operation, just 12 orthonormal CBFs are retained. The same process is repeated for the second block containing one coaxial probe, where the total number of RWGs is 612. For

this block the number of initially generated CBFs is 17, while the number of retained orthonormal CBFs is only 4. The generation of primary CBFs is done by an incident plane wave spectrum whose angles of incidence are separated by 90 degrees along the θ and ϕ axes, and for two polarizations. It is pointed out that a smaller number of RWGs on the pins is used as compared to the coaxial probes, which is mainly due to their distance from the excitation source.

After mapping the so-generated CBFs onto the 94 blocks within the whole structure, the upper triangular part of the reduced matrix is constructed by filling only 665 mutual MoM matrix blocks, instead of all $94 \times 94 = 8836$. After assembling the reduced matrix and computing the reduced set of excitation vectors (which involves the fields from the magnetic frill currents), the reduced matrix equation with 1110 unknowns can be solved directly and is much smaller of the 37352 RWGs that were required for the discretization of the entire structure. Since the CBFs and therefore the surface currents are expressed in terms of RWGs, the scattering parameters and field patterns can be computed accordingly. In Fig. 6.6(a), the S_{21} and S_{11} parameters as computed by the above-described CBFM procedure are compared to those obtained by the HFSS software. One can observe that there is a good agreement between the CBFM and the plain MoM for the computed scattering parameters.

By changing L_2 one can examine the total solve time as a function of the problem size. The obtained results are shown in Fig. 6.6(b), where the scaling of the solve time for CBFM outforms that of HFSS by about a factor of three. Also, for equal simulation times, the problem size for CBFM can be about twice larger than for the HFSS software. The HFSS software could not handle problems for $d_{\text{probe}} > 1.3$ m, due to memory constraints for that server. The non-gradual increase in simulation time is caused by the adaptive meshing of HFSS.

In Fig. 6.7, the number of CBFs and tetrahedras that are employed in the CBFM and the HFSS software are shown as a function of d_{probe}, respectively. One observes that the number of CBFs grows linearly, while the number of tetrahedras does not, which may be due to the adaptive meshing in HFSS.

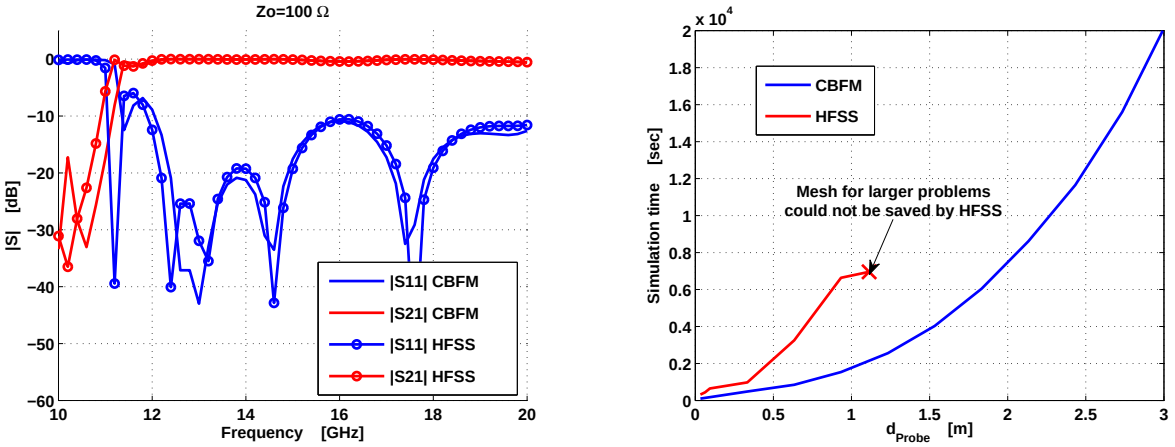

(a) (b)

Figure 6.6: (left) the numerical results as computed by the CBFM employing the parallel-plate Green's function. The numerically computed results are validated through the HFSS software; (right) Scaling of the method: the total solve time as a function of problem size (d_{probe}).

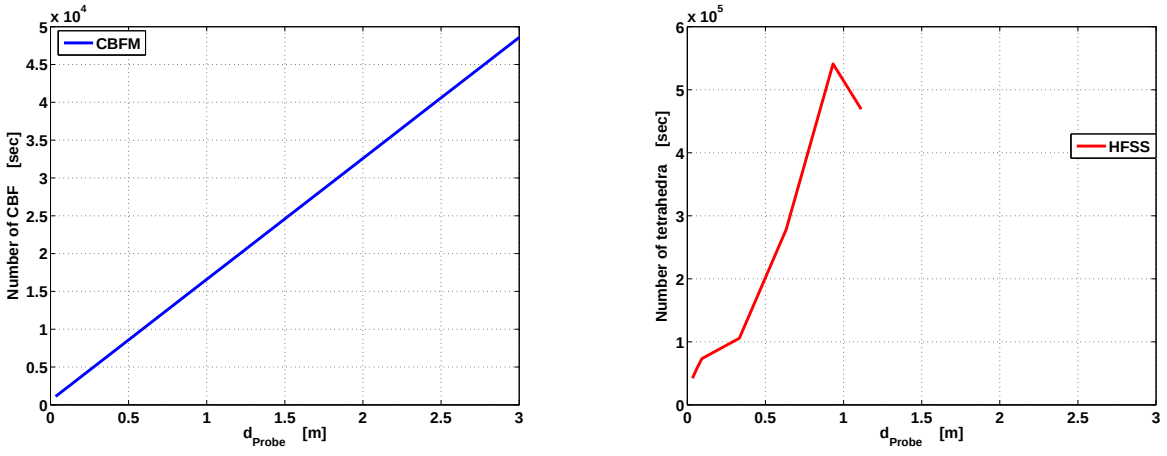

(a) (b)

Figure 6.7: (left) Number of CBFs; (right) Number of tetrahedra as a function of problem size (d_{probe}).

6.4.2 Accuracy and Computation Time Comparisons Between the CBFM and a Plain MoM Approach

In this section, we study besides the accuracy also the timing behavior of the CBFM. For this purpose, a structure consisting of two coaxial probes separated by a row of pins is considered at 12 GHz. The accuracy is assessed by comparing the CBFM with a plain MoM, which employs RWG basis functions only. For the present structure, the same CBFM procedure as for the groove gap waveguide is followed, except that now the total number of pins is 23 in addition to the two coaxial probes. Also, the total number of RWG basis functions is 10230 as compared to the 37352 RWG basis functions that were employed in the groove gap waveguide case. Since the geometry of the pins and probes is the same as for the groove gap waveguide, the total number of RWG basis functions for each pin and probe is identical. Furthermore, by setting the SVD threshold to 10^{-3}, we obtain the same numbers of initially generated CBFs and retained orthonormal CBFs for each of the pins and probes.

In Fig. 6.8, the average current distribution in dBA/m is plotted for both the CBFM and the direct MoM solution. For the purpose of accuracy comparisons between the CBFM and plain MoM solutions, we can analyze the average error of the RWG expansion coefficients. This relative error, which can be plotted as a function of the SVD threshold and also as a function of the number of CBFs per pin, can be defined as

$$\text{Rel. Error} = \frac{\sqrt{\sum_{n=1}^{N} |I_n^{\text{RWG,MoM}} - I_n^{\text{RWG,CBFM}}|^2}}{\sqrt{\sum_{n=1}^{N} |I_n^{\text{RWG,MoM}}|^2}} \times 100\%. \tag{6.16}$$

In Fig. 6.9(a), the relative error (6.16) is plotted as a function of the SVD threshold, which is varying from 10^{-10} to 1. It can be seen that the relative error is increasing as the SVD threshold is increasing. This behavior is expected and can be justified with the help of Fig. 6.4, which shows that for higher SVD thresholds, a smaller number of CBFs are retained for each pin and coaxial probe, which in turn decreases the accuracy of the CBFM. This behavior can also be observed in Fig. 6.9(b), where a larger number of CBFs per pin and probe gives rise to a smaller relative error.

In Fig. 6.10, the total execution time needed for building and solving the system at 12 GHz is plotted versus the number of pins, both for CBFM and MoM. One observes that

the computation time increases for a larger number of pins in the structure, however, the required time to build and solve the system for the CBFM, is seen to be much smaller than the time required for a plain MoM approach.

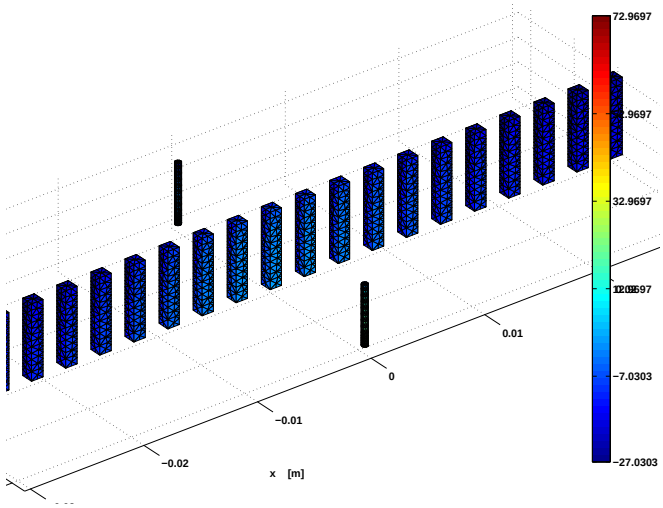

Figure 6.8: Magnitude of the averaged current distribution for the CBFM solution at 12 GHz.

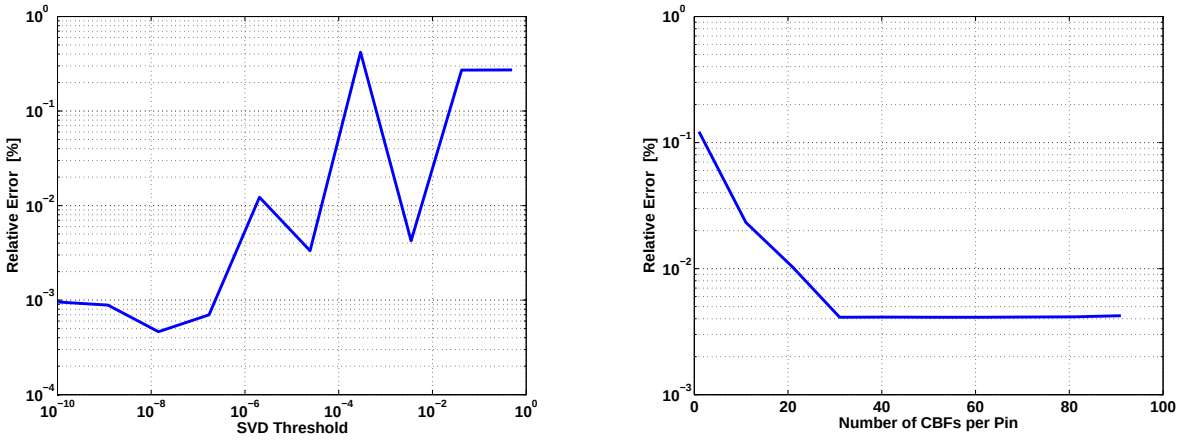

(a) (b)

Figure 6.9: (a) Relative error of the RWG expansion coefficients for the CBFM relative to a plain MoM approach, versus the SVD threshold,(b) and versus the number of CBFs per pin.

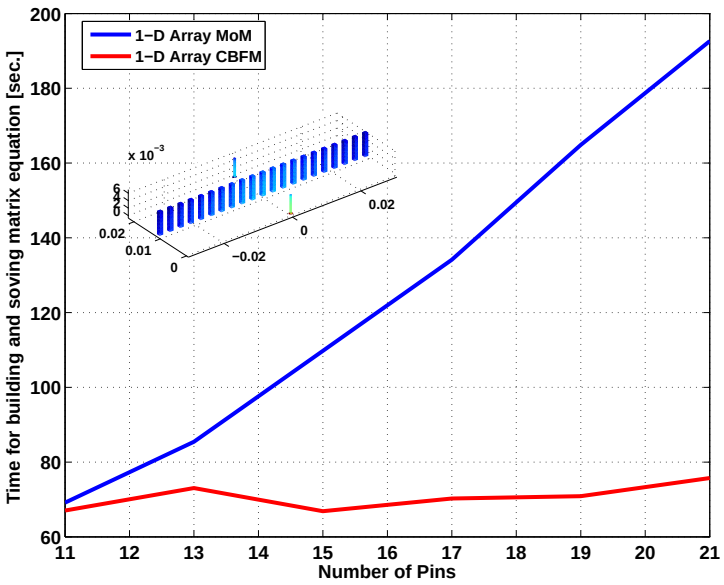

Figure 6.10: Computation time as a function of the total number of pins, for CBFM and a plain MoM approach.

6.5 Conclusions

In this chapter we studied a numerically efficient technique, called the Characteristic Basis Function Method (CBFM), for solving electromagnetic problems involving large gap waveguide structures. This method is based on splitting the original computational domain into a number of smaller subdomains, or blocks. For each block, high-level basis functions called Characteristic Basis Functions (CBFs) can be derived by the application of a plain MoM approach employing triangular RWG basis functions that are supported by triangular patches. While this approach results in a significant reduction of the number of unknowns in the final matrix equation that need to be solved, still the construction of the resulting reduced matrix can be time-consuming. To alleviate the problem of the large matrix fill-time, the Adaptive Cross Approximation (ACA) algorithm has been used hybridized with CBFM to take advantage of the rank-deficient properties of the coupling matrix blocks representing well-separated MoM interactions.

In our first numerical results, the accuracy of the CBFM for the analysis of a groove gap waveguide was validated by comparing the magnitude of the computed S-parameters with

those obtained using the HFSS software. The numerical results as computed by the CBFM have shown to be in good agreement with those obtained through the HFSS software, in the entire frequency range of 10–20 GHz. We also examined the total solve time as a function of the problem size for the CBFM and HFSS simulation results. It is observed that the scaling of the solve time for the CBFM outforms that of HFSS by about a factor of three. Afterwards, the numerical complexity and scaling in terms of the number of CBFs and tetrahedras in CBFM and HFSS was studied as a function of the distance between the two coaxial probes, d_{probe}, where the number of CBFs had a linear growth for larger d_{probe}, but the number of tetrahedras did not grow linearly likely due to adaptive meshing.

In the second example, the accuracy of the proposed CBFM has been studied for a parallel-plate waveguiding structure containing two coaxial probes separated by one row of metallic pins. The accuracy has been computed as the relative error of the RWG expansion coefficients in the CBFM and a direct MoM approach, and has been plotted for different SVD threshold values, where larger SVD threshold values resulted in larger relative errors and therefore lower solution accuracy. Also, it has been shown that the larger number of CBFs for each pin led to a higher solution accuracy. Finally, we observed that the computation time in both CBFM and MoM is increasing for larger structures, however, the CBFM can achieve a noticeable reduction in the overall CPU time and memory storage requirements as compared to a conventional MoM approach.

Chapter 7

Conclusions and Recommendations

7.1 Conclusions

In this thesis, we started by the introducing of the gap waveguide technology as well as the possible methods that can be used for the fast numerical analysis (and optimization) of gap waveguide structures. In Chapter 2, a motivation is provided for considering the simpler infinite parallel-plate waveguide as the basic structure for the numerical analysis of gap waveguides. We continued to identify different approaches that are used for the fast computation of the dyadic parallel-plate Green's function.

The Green's function has been formulated for an infinitely large parallel-plate structure in the spatial domain by considering a point source within the parallel-plate region, after which the image principle was invoked to obtain two infinitely large 1-D array of point sources in free space. The field of this line array was computed rapidly using the Shanks-accelerated spatial Green's function method, while other methods, such as the Ewald summation method, or the spectral-domain summation method, were found to be less efficient for our type of problems. The convergence properties of these acceleration methods were examined through several numerical examples in Chapter 3.

The method of moments was presented in Chapter 4 to compute the impedance and propagation characteristics of electromagnetic structures, such as waveguides. Toward this end, a continuous operator equation with limited spatial domain, i.e. the electric field integral

equation (EFIE), was derived, discretized and then transformed into a matrix equation. The moment matrix elements were computed afterwards and the potential integrals were evaluated numerically for both the free space and the parallel-plate Green's function. The matrix equation resulting from the discretization of the EFIE, can then be solved through the application of a standard Gaussian elimination method. Afterwards, the method of moment has been employed for the numerical analysis of a parallel-plate waveguiding structure, excited by a pair of monopole antennas (coaxial probes) that are separated by a row of pins. The numerically computed results for the S_{11} and S_{22} parameters were found to be in good agreement with those simulated through the HFSS software.

In Chapter 5, the Padé rational function has been studied and employed as a suitable method for the interpolation of spectral domain data, including the input impedance of antennas. This interpolation technique was applied to the structure of two monopole antennas in a waveguide region to approximate the input impedance of the structure using only a few frequency samples. The numerically computed results have been compared to those obtained from a MoM computation. This was done for different numerator and denominator orders, where we found the best fitting model is achieved for the largest number of frequency samples. We then proposed an adaptive frequency sampling method as an approach to minimize the number of samples needed for the Padé rational function fitting, which also minimizes the computation time to reach a desired solution accuracy. This adaptive technique has been applied to two examples: a center-fed dipole antenna; and the structure of two monopole antennas in a waveguiding region. In the former example, the Padé approximation at the final fitting frequencies have been compared to the ones computed through an equivalent circuit model, while for the latter structure the approximated results have been validated through the CAESAR software.

In Chapter 6, we studied a recently developed MoM-based approach, called the Characteristic Basis Function Method (CBFM), which is a numerically efficient computational electromagnetic method for solving large-scale electromagnetic problems. In this chapter we dealt with the employment and generation of Characteristic Basis Functions (CBFs), which have been constructed through the application of a conventional MoM approach. The CBFs are supported on relatively large subdomains and result in a significant reduction of the number of unknowns and thus the size of the MoM matrix. Furthermore, translation symmetry and the application of the Adaptive Cross Approximation technique (ACA) are considered for the efficient generation of the reduced MoM matrix. The accuracy of the CBFM scheme has been shown via numerical examples, where we found that

for higher SVD threshold values, and thus smaller number of CBFs for each pin, lower accuracy of the CBFM solution is achieved. We have also shown that the CBFM can achieve a significant reduction in the CPU time as compared to a plain MoM approach and the HFSS software, which makes it efficient for solving large electromagnetic problems without resorting to iterative solvers.

7.2 Recommendations

This thesis focused on several enhancement techniques for increasing the computational efficiency for the analysis of electromagnetic structures, in particular for gap waveguide structures. However, there are still areas that need to be studied in more detail, and other methods could be used to further improve the computational efficiency.

- In Chapter 2, the Ewald method is presented as an efficient way for the evaluation of the dyadic parallel-plate Green's function. Due to numerical instabilities of the Ewald summation at high frequencies, it is worthwhile to study the robustness of G_{spectral} in this summation. In this context, a more detailed study should also be performed on the choice of the Ewald splitting parameter for different plate distances.

- Presenting the Padé approximation and adaptive frequency sampling in Chapter 5, it is recommended to implement the Padé interpolation in the CAESAR software in conjunction with CBFM (not only for MoM), to rapidly compute the frequency response of very large electromagnetic structures.

- As it is discussed in Chapter 7, the mesh construction is a part of the CBF generation by replicating the mesh of building blocks elsewhere in the array environment through translation. To verify the solution convergence and also to achieve an optimal non-uniform mesh, it is suggested to implement an adaptive mesh-refinement procedure.

Appendix A

Poisson's Summation Formula

The objective is to transform the slowly convergent series (2.38), i.e.,

$$g(z,\epsilon) = \sum_{n=-\infty}^{\infty} e^{-(z-nd_z)^2\epsilon^2} \tag{A.1}$$

into a rapidly converging one. Upon defining the function $f(z) = e^{-z^2\epsilon^2}$, the above summation can be written as

$$g = \sum_{n=-\infty}^{\infty} f(z - nd_z). \tag{A.2}$$

One can see that, since we are summing shifted versions of f by a period d_z, the function g is periodic with period d_z.

If $f(z)$ alone exists over a large interval (because it is a slowly decaying function), and/or d_z is sufficiently small, the spatial summation (A.2) may better be evaluated in the spectral domain to reduce the number of terms that need to be summed. Since g is periodic, we can use the spatial Fourier series to expand g as,

$$g = \sum_{k=-\infty}^{\infty} c_k e^{j\frac{2\pi}{d_z}kz} \tag{A.3}$$

where the complex-valued Fourier coefficients are herein defined as

$$c_k = \frac{1}{d_z}\int_0^{d_z} g(z)e^{-j\frac{2\pi}{d_z}kz}\mathrm{d}z. \tag{A.4}$$

substituting (A.2) in (A.4), and interchanging the summation and integration, yields

$$c_k = \frac{1}{d_z} \sum_{n=-\infty}^{\infty} \int_0^{d_z} f(z - nd_z) e^{-j\frac{2\pi}{d_z}kz} \mathrm{d}z. \tag{A.5}$$

changing variables, i.e. $z - nd_z = z'$, and using that $e^{-j2\pi kn} = 1$, if $\{k, n\} \in \mathbb{Z}$, yields

$$\begin{aligned} c_k &= \frac{1}{d_z} \sum_{n=-\infty}^{\infty} e^{-j2\pi kn} \int_{-nd_z}^{(-n+1)d_z} f(z') e^{-j\frac{2\pi}{d_z}kz'} \mathrm{d}z' \\ &= \frac{1}{d_z} \sum_{n=-\infty}^{\infty} \int_{-nd_z}^{(-n+1)d_z} f(z') e^{-j\frac{2\pi}{d_z}kz'} \mathrm{d}z' \\ &= \frac{1}{d_z} \int_{-\infty}^{\infty} f(z') e^{-j\frac{2\pi}{d_z}kz'} \mathrm{d}z' \\ &= \frac{\sqrt{2\pi}}{d_z} F\left(\frac{2\pi k}{d_z}\right) \end{aligned} \tag{A.6}$$

where F is the Fourier Transform of f, i.e.,

$$F(k_z) = \frac{1}{\sqrt{2\pi}} \int_{-\infty}^{\infty} f(z) e^{-jk_z z} \mathrm{d}z \tag{A.7}$$

and where $k_z = \frac{2\pi k}{d_z}$. Substituting (A.6) in (A.3), gives

$$g = \frac{\sqrt{2\pi}}{d_z} \sum_{k=-\infty}^{\infty} F\left(\frac{2\pi k}{d_z}\right) e^{j\frac{2\pi}{d_z}kz}. \tag{A.8}$$

Finally, substituting (A.2) in (A.8) yields

$$\boxed{\sum_{n=-\infty}^{\infty} f(z - nd_z) = \frac{\sqrt{2\pi}}{d_z} \sum_{k=-\infty}^{\infty} F\left(\frac{2\pi k}{d_z}\right) e^{j\frac{2\pi}{d_z}kz}} \tag{A.9}$$

which is known as Poisson's summation formula. If the summation on the left-hand side of (A.2) is slowly convergent, the summation on the right-hand side may converge much more rapidly.

Next, on account of (2.38) we wish to find the Fourier transform F of the Gaussian function $f(z) = e^{-z^2\epsilon^2}$. For this, we use the tabulated standard Fourier transform pair

$$e^{-\alpha x^2} \quad \longleftrightarrow \quad \frac{1}{\sqrt{2\alpha}} e^{-\frac{\omega^2}{4\alpha}} \qquad (\mathfrak{Re}\{\alpha\} > 0) \tag{A.10}$$

so that

$$F(k_z) = \frac{1}{\sqrt{2}|\epsilon|} e^{-\frac{k_z^2}{4\epsilon^2}} \tag{A.11}$$

Substituting this in (A.9) finally yields for (A.1)

$$\sum_{n=-\infty}^{\infty} e^{-(z-nd_z)^2\epsilon^2} = \frac{\sqrt{\pi}}{d_z|\epsilon|} \sum_{k=-\infty}^{\infty} e^{-\left(\frac{\pi k}{d_z\epsilon}\right)^2} e^{j\frac{2\pi}{d_z}kz}. \tag{A.12}$$

Appendix B

Geometrical Notations

To solve the potential integrals given in (4.32) in closed form, some geometrical quantities need to be introduced. Considering Fig. B.1, we have defined a local cartesian coordinate system $\{\hat{\boldsymbol{u}}, \hat{\boldsymbol{v}}, \hat{\boldsymbol{w}}\}$ where $\hat{\boldsymbol{u}} = (\boldsymbol{q}_2 - \boldsymbol{q}_1)/l_3$. Here the length l_i is the ith edge length opposing the corner vertex $\boldsymbol{q}_i$ of a source triangle of a RWG basis function, and $\hat{\boldsymbol{v}} = \hat{\boldsymbol{n}} \times \hat{\boldsymbol{u}}$, where $\hat{\boldsymbol{n}}$ is normal to the triangle in the uv-plane. Since the local origin is $\boldsymbol{q}_1$, the position vector $\boldsymbol{r}$ is defined as (u_0, v_0, w_0) where $u_0 = (\boldsymbol{r} - \boldsymbol{q}_1) \cdot \hat{\boldsymbol{u}}$, $v_0 = (\boldsymbol{r} - \boldsymbol{q}_1) \cdot \hat{\boldsymbol{v}}$ and $w_0 = (\boldsymbol{r} - \boldsymbol{q}_1) \cdot \hat{\boldsymbol{n}}$. The corner vertices are: $\boldsymbol{q_1} = (0, 0, 0)$, $\boldsymbol{q_2} = (l_3, 0, 0)$ and $\boldsymbol{q_3} = (u_3, v_3, 0)$ and the height of the position vector $\boldsymbol{r}$ above the triangle plane is $\boldsymbol{\rho}_{\|} = \boldsymbol{r} - w_0\hat{\boldsymbol{n}}$.

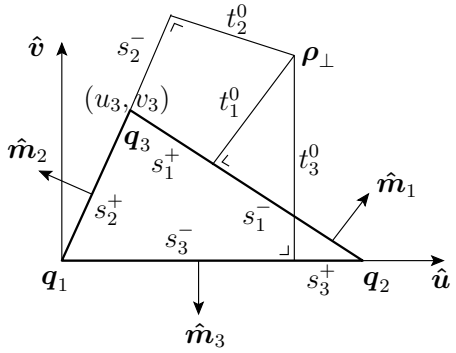

Figure B.1: Geometrical quantities for analytical integration

Using these quantities, the distances from the vector $\boldsymbol{r}$ to the line's begin and end points

are defined as

$$R_1^+ = R_2^- = \|\boldsymbol{r} - \boldsymbol{q}_3\|_2 \qquad R_2^+ = R_3^- = \|\boldsymbol{r} - \boldsymbol{q}_1\|_2 \qquad R_3^+ = R_1^- = \|\boldsymbol{r} - \boldsymbol{q}_2\|_2. \tag{B.1}$$

The distances t_i^0, for $i = 1, 2, 3$, which are the perpendicular distances from the point $\boldsymbol{\rho}_\parallel$ to the ith line segment, are given as

$$t_1^0 = \frac{v_0(u_3 - l_3) + v_3(l_3 - u_0)}{l_1}, \qquad t_2^0 = \frac{u_0 v_3 - v_0 u_3}{l_2}, \qquad t_3^0 = v_0 \tag{B.2}$$

with reference to Fig. B.1, the end points s_i^- and s_i^+ of the line segments can be given as

$$s_1^- = -\frac{(l_3 - u_0)(l_3 - u_3) + v_0 v_3}{l_1} \qquad s_2^- = -\frac{u_3(u_3 - u_0) + v_3(v_3 - v_0)}{l_2} \qquad s_3^- = -u_0 \tag{B.3}$$

and also as

$$s_1^+ = s_1^- + l_1, \qquad s_2^+ = s_2^- + l_2, \qquad s_3^+ = s_3^- + l_3. \tag{B.4}$$

From these equations, it is derived in [23] for the ith edge that

$$I_i^{-1} = \iint\limits_{\partial_i T_n} \frac{1}{R} dl' = ln\left(\frac{R_i^+ + s_i^+}{R_i^- + s_i^-}\right). \tag{B.5}$$

For the higher order terms in α we have from [24]

$$I_i^\alpha = \iint\limits_{\partial_i T_n} R^\alpha dl' = \frac{1}{1+\alpha}\left(s_i^+ (R_i^+)^\alpha - s_i^- (R_i^-)^\alpha + \alpha (R_i^0)^2 I_i^{(\alpha-2)}\right) \tag{B.6}$$

where $\alpha = 1, 3, 5, ...$, and we know that

$$w_0 K_1^{-3} = w_0 \iint\limits_{T_n} \frac{1}{R^3} dS' = \begin{cases} 0 & w_0 = 0 \\ \frac{w_0}{|w_0|} \sum_{i=1}^3 \beta_i & \text{otherwise} \end{cases} \tag{B.7}$$

and for $w_0 \neq 0$ we have that

$$\beta_i = \begin{cases} \arctan\left(\frac{t_i^0 s_i^+}{(R_i^0)^2 + |w_0| R_i^+}\right) - \arctan\left(\frac{t_i^0 s_i^-}{(R_i^0)^2 + |w_0| R_i^-}\right) & t_i^0 \neq 0 \\ 0 & \text{otherwise} \end{cases} \tag{B.8}$$

Now we can evaluate the integrals in (4.32) analytically by

$$K_1^\alpha = \begin{cases} \frac{1}{2+\alpha} \sum_{i=1}^3 t_i^0 I_i^\alpha & w_0 = 0 \\ \frac{1}{2+\alpha}\left(\alpha w_0^2 K_1^{\alpha-2} + \sum_{i=1}^3 t_i^0 I_i^\alpha\right) & \text{otherwise} \end{cases} \tag{B.9}$$

$$\boldsymbol{K}_2^\alpha = (\boldsymbol{\rho}_\parallel - \boldsymbol{q}) K_1^\alpha + \frac{1}{2+\alpha} \sum_{i=1}^3 I_i^{2+\alpha} \boldsymbol{m}_i \tag{B.10}$$

where $\boldsymbol{m}_i$ are the outward unit normals to the edges $\partial_i T_n$.

Appendix C

Adaptive Frequency Sampling Code and Functions

To perform the adaptive frequency sampling method in the CAESAR software for the fast computation of the impedance characteristics of electromagnetic structures, several matlab functions have to be developed. After defining the EM structure in the main script of CAESAR, the first function of interest is the **RunEMSimulatorNew**. This function includes three more functions: **RunEMSimulator**; **padeeMatrix**; and **NextFreq**. Except of the **RunEMSimulator** function, which is used here to yield the antenna impedance matrix at the desired frequency, we describe the **padeeMatrix** function, which is used to give the Padé approximation of the entire 2×2 impedance matrix elements, and **NextFreq**, which adaptively determines the next sampling frequency point.

C.1 RunEMSimulatorNew.m

```
function RunEMSimulatorNew(Const,Geom,CBFM,ExcitationField,Array)
if Const.AdaptiveFreqSampling
    if Const.RunEngine
        fout=Const.Freq;
        NoOfFreq=length(fout);
        FreqIndex=[1,NoOfFreq];
```

```
fin=fout(FreqIndex).';
% the first two fitting frequencies are selected as the
%first and the last point in the desired frequency range
Const.Freq=fin;
Zin=RunEMSimulator(Const,Geom,CBFM,ExcitationField,Array);
% the fin is given as the input of the RunEMSimulator to
%determine the corresponding impedance matrix
[con_old,Zout_old,den_old]=padeeMatrix(fin,Zin,fout);
%in padeeMatrix the rational function for Zin, which is here a
%(lenght(fin),2,2) matrix, is estimated at given frequencies in
%fout
NextFreqIndex=round(NoOfFreq/2);
% the third selected frequency is in the middle of output
% frequency range
TotalError=[];
MaxRelError=1e100;
con_new=1;

% for each added frequency point, the impedance matrix is
% estimated for the updated fin in padeeMatrix.
% The maximum relative error between the two recently
% estimated impedance matrix is then checked every time
% against the specified estimation error. it is checked
% also that the maximum condition number of the impedance
% matrix is less than a maximum specified value.

while(MaxRelError>Const.AdaptiveFreqTolerance)&
(max(max(con_new))<Const.MaxCond)
  RelError=zeros(NoOfFreq,1);
  FreqIndex=[FreqIndex NextFreqIndex];
  fin=fout(FreqIndex).';
  Const.Freq=fout(NextFreqIndex);
  Zin(length(FreqIndex),:,:)=
  RunEMSimulator(Const,Geom,CBFM,ExcitationField,Array);
  [con_new,Zout_new,den_new]=padeeMatrix(fin,Zin,fout);
  [MaxRelError,NextFreqIndex,Zout_old]=
  NextFreq(Zout_old,Zout_new,FreqIndex,Const);
```

```
       end
        if max(max(con_new))>Const.MaxCond
            Zin(end,:,:)=[];
            fin(end)=[];
            [con_new,Zout_new,den_new]=padeeMatrix(fin,Zin,fout);
        end
        Const.Freq=fout;
        for FreqCount=1:length(Const.Freq)
            Zant=squeeze(Zout_new(FreqCount,:,:));
            % here Zant is a 2*2 impedance matrix
            % computed at each frequency point.
        end
    end
else
    RunEMSimulator(Const,Geom,CBFM,ExcitationField,Array)
end
return
```

C.1.1 padeeMatrix.m

```
function [con,Zout,den]= padeeMatrix(fin,Zin,fout)
% Zin is the impedance matrix computed at optimum vector fin.
con=zeros(size(Zin,2),size(Zin,3));
% con is the condition number matrix
den=con;
Zout=zeros(length(fout),size(Zin,2),size(Zin,3));
for m=1:size(Zin,2)
  for n=1:size(Zin,3)
   [con(m,n),Zout(:,m,n),den(m,n)]=padee(fin,Zin(:,m,n),fout);
  end
end
return
```

padee.m

```
function [con,Zout,den]= padee(fin,Zin,fout)
% in this function the denominator order is selected automatically.
Nf=length(fin);
den=0;
num=Nf-den-1;
conOld=inf;
conNew=inf;

while (conNew<=conOld)&&(Nf-den-2>0)
    den=den+1;
    num=Nf-den-1;
    A=zeros(Nf,Nf);
    for i=0:num
        A(:,1+i)=fin.^i;
    end

    for i=0:den-1
        A(:,num+2+i)=-Zin.*fin.^i;
        % Zin is the impedance element vector which has
        %the same size as fin.
    end
    conOld=conNew;
    conNew=cond(A);
end
if den>1
    den=den-1;
    % the optimum value of den is the one before the last one.
end
num=Nf-den-1;
A=zeros(Nf,Nf);

for i=0:num
    A(:,1+i)=fin.^i;
end
```

```
for i=0:den-1
    A(:,num+2+i)=-Zin.*fin.^i;
end
con=cond(A);
b=Zin.*fin.^den;
x=inv(A)*b;
N=flipud(x(1:num+1)); D=flipud(x(num+2:end));
Zout=polyval(N,fout)./(polyval(D,fout)+fout.^den);
% the impedance matrix rational function estimated at fout;
```

C.1.2 NextFreq.m

```
function [MaxRelError,NextFreqIndex,Zout_old]
=NextFreq(Zout_old,Zout_new,FreqIndex,Const)
for i=1:size(Zout_old,1)
        RelError(i)=norm(squeeze(Zout_new(i,:,:)-Zout_old(i,:,:)))
        /norm(squeeze(Zout_old(i,:,:)));
end
[MaxRelError,Index]=sort(RelError,'descend');
%finding the relative error vector between the two
%newly computed impedance matrix and their corresponding
%frequency indexes
n=1;
while (~isempty(find(Index(n)==FreqIndex)))&&(n~=length(Index))
    n=n+1;
end
% the while loop is for finding the first frequency index with
% maximum relative error which is not part of the current
% frequency index.
if n==length(Index)
    MaxRelError=0;% when the selected fitting frequencies have
    %the same length as the output frequencies
    NextFreqIndex=[];
    return
elseif MaxRelError(n)>Const.AdaptiveFreqTolerance
    NextFreqIndex=Index(n);
```

```
    MaxRelError=MaxRelError(n);
    Zout_old=Zout_new;
else
    NextFreqIndex=[];
end
return
```

Appendix D

Publications

The work as presented in this thesis has resulted in two conference publications which are included below. The first paper is entitled "Comparison of Parallel-Plate Greens Function Acceleration Techniques" has been accepted and presented at the EuCAP 2012 conference, which was held in Prague, Czech Republic. The second paper with the title "Fast Analysis of Gap Waveguides Using the Characteristic Basis Function Method and the Parallel-Plate Green's Function" has been accepted for presentation at the ICEAA-IEEE APWC 2012, which will be held in Cape Town, South Africa.

Comparison of Parallel-Plate Green's Function Acceleration Techniques

Pegah Takook
Department of Signals and Systems
Chalmers University of Technology
S-41296 Gothenburg, Sweden
Email: takook@student.chalmers.se

Rob Maaskant
Department of Signals and Systems
Chalmers University of Technology
S-41296 Gothenburg, Sweden
Email: rob.maaskant@chalmers.se

Per-Simon Kildal
Department of Signals and Systems
Chalmers University of Technology
S-41296 Gothenburg, Sweden
Email: per-simon.kildal@chalmers.se

***Abstract*—A comparative study of acceleration methods for computing the infinite series summation arising in parallel-plate Green's functions is performed. The spectral summation, the application of the Shanks-transformed spatial summation, and the Ewald method are examined. Results are presented which show that, although the convergence rates of Ewald's method and the spectral summation are generally largest (i.e. less number of terms), the total series evaluation time for reaching a certain specified accuracy – which is ultimately of more importance – is shortest for the Shanks accelerated spatial summation in most cases of practical interest.**

I. Introduction

Recently, the novel low-loss low-cost *gap waveguide technology* has been developed for high-frequency waveguide and transmission-line applications [1]. Both the groove and ridge gap waveguides employ perfect electric conductors in the upper and lower plates in conjunction with a bed of nails to realize a perfect magnetic conductor [2]. Fig. 1 illustrates an example of a ridge-gap waveguide that has been manufactured and measured [3]. It is shown that the propagating electric field is confined in between the ridge and top lid, which demonstrates the close resemblance with the TEM stripline transmission line. Indeed, below the parallel-plate cut-off frequency, when the distance between the upper metallic surface and the bottom ground plane is smaller than $\lambda/4$, a single dispersion-free quasi TEM-wave can be excited which is confined in the gap formed by the ridge and the top ground plane (over an octave bandwidth) [2], [4].

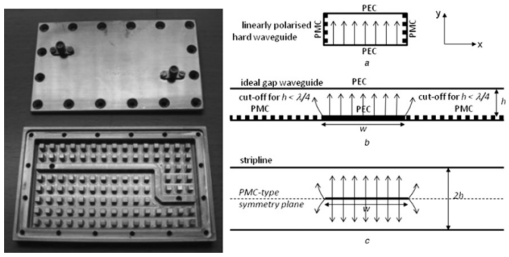

Fig. 1. Left: ridge gap-waveguide with S-bended ridge. Right: (a) ideal PMC-PEC waveguide boundary conditions for TEM-mode propagation; (b) PMC realization using a bed of nails; (c) stripline transmission line equivalence.

In the stop-band, the pins inside the PEC box prevent the fields from leaking towards its sidewalls, so that one can remove the sidewalls without affecting the field propagation characteristics at these frequencies. Hence, the equivalent structure that can be analyzed constitutes a bed of nails which is connected to the bottom (or top) plate of a parallel-plate waveguide. Consequently, in a method-of-moment (MoM)-based approach, it suffices to employ the simpler parallel-plate instead of the more complex cavity Green's function, which simplifies the numerical analysis of gap waveguide structures – operating the in the stop band – significantly. Furthermore; the MoM matrix-fill time can be reduced, since the translation symmetry of the computed reaction integrals between pairs of basis functions is maintained.

To compute the parallel-plate Green's function, the image principle is invoked for an infinitsimally small dipole source placed inside a parallel-plate waveguiding region, after which the slowly convergent 1-D infinite series summation of spatial Green's functions is transform into a rapidly convergent one. Among the most popular methods, we mention the Shanks transformation [5], the spectral summation technique [6], and Ewald's method [7]. Most frequently, one focusses on minimizing the number of summation terms to increase the convergence rate. However, to reach a certain convergence accuracy, the total series evaluation time may still exceed that of a more straightforward method requiring more summation terms. The method to use depends on the required accuracy, the geometry, the position and orientation of the dipole source, as well as the observation location.

With reference to the physics-based interpretation of the parallel-plate waveguide fields in Fig. 2, a spherical-wave, cylindrical-wave, or hybrid-mode expansion should be chosen for representing the parallel-plate waveguide fields. To investigate the differences, the required time for computing the field generated by a z-oriented dipole placed at the center of a parallel-plate waveguide (*cf.* Fig. 2) will be examined as a function of the source-observation and parallel-plate separation distance $\rho \geq 0.1\lambda$ and $0.1\lambda \leq d \leq 0.9\lambda$, respectively. In the spatial, spectral, or Ewald summation method, this time is estimated as

$$T^{\text{Method}} = T_0^{\text{Method}} N^{\text{Method}}(\epsilon, d, \rho) \qquad (1)$$

where "Method" $\in \{\text{Spatial}, \text{Spectral}, \text{Ewald}\}$, T_0 is the time required to evaluate one series term, and N is the number of terms needed to reach the relative accuracy ϵ. The evaluation time for the Shanks transformation can be described by

$$T^{\text{Shanks},n} = T_0^{\text{Spatial}}[N^{\text{Shanks},n}(\epsilon, d, \rho) - n] + T_{\text{e}}^{\text{Shanks},n} \quad (2)$$

where n is the order of the Shanks transformation and $T_{\text{e}}^{\text{Shanks},n}$ is the infinite-sum extrapolation time needed after summing $N - n$ spatial terms.

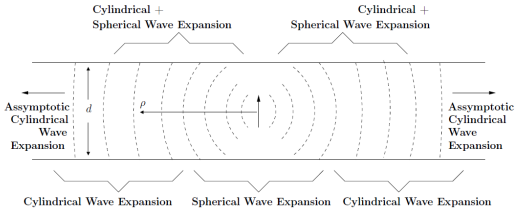

Fig. 2. An illustration of the radiated field of a z-oriented dipole centered inside a parallel-plate waveguide. Physics shows that a spherical-type of wave expansion is best suited near the source point, while a cylindrical-wave expansion seems more appropriate for observation points farther out and for a small plate distance d. Furthermore, the fields in the intermediate region may be best described by a hybrid method. The appropriate selection of the respective acceleration methods in terms of the total Green's function evaluation time is subject of investigation in this paper.

II. Spatial Summation

From a physics point of view, the spatial Green's function summation seems most suited in the near-source region, see also Fig. 3. The periodic Green's function for this 1D periodic infinite array of equally strong and equidistant point sources spaced a distance d apart, is given by

$$G_N = \frac{1}{4\pi} \sum_{n=-N}^{N} \frac{e^{-jkR_n}}{R_n} \quad (3)$$

where $R_n = \sqrt{\rho^2 + (nd)^2}$ is the distance between the observation point and the nth source point.

A. Shanks Accelerated Spatial Summation

It is well-known that the summation in (3) is slowly convergent. One of the methods used to accelerate the Green's function series convergence is the Shanks transformation. Although in [8] it is proposed to combine the Shanks transformation with Kummer's transformation, repeated application of Shanks transformation alone can already have great effect in reducing the computation time. The first-order Shanks transformation (extrapolation) of the partial sum G_N is defined as [5]

$$G_\infty \approx \frac{G_{N+1}G_{N-1} - G_N^2}{G_{N+1} - 2G_N + G_{N-1}}. \quad (4)$$

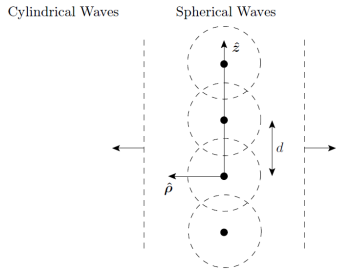

Fig. 3. Line array of point sources spaced a distance d apart, which individually generate spherical waves (i.e. observation point near one of the sources), but collectively generate cylindrical waves (i.e. observation point away from the sources).

III. Spectral Summation

When the fields of more point sources contribute significantly, as in case of observation points away from the 1-D array of source points and/or small d, the summation of spectral terms is desired instead. Physically, this can be understood by realizing that each point source emits a spherical wave and, on account of Huygen's principle, all spherical wave fronts together form a cylindrical wave which propagates away from the line array. The 3-D spectral Green's function for a 1-D array of equally-phased dipoles is written as [6]

$$G = \frac{1}{4jd_z} \sum_{n=-\infty}^{\infty} H_0^{(2)}(\alpha_n \rho) e^{jk_{z,n}z} \quad (5)$$

where $H_0^{(2)}$ is the Hankel function of the second kind and zeroth order, and where

$$\alpha_n = \begin{cases} \sqrt{k^2 - k_{z,n}^2} & \text{if } k^2 > k_{z,n}^2 \\ -j\sqrt{k_{z,n}^2 - k^2} & \text{if } k^2 < k_{z,n}^2 \end{cases}, \text{ and } k_{z,n} = \frac{2\pi n}{d}. \quad (6)$$

The nth wavenumber along ρ is denoted by α_n, and $k_{z,n}$ is the nth wavenumber along z-axis. Here, as in the case of a lossless medium, $\Im\mathrm{m}\{\alpha_n\} = 0$ represents the propagating waves and $\Im\mathrm{m}\{\alpha_n\} < 0$ represents the attenuating waves along the ρ-axis, respectively. It is well-known that, in the evaluation of the Green's function in (5), a singularity is encountered when $\rho = 0$, i.e., when the observation point is on the line array. However, in MoM approaches, this problem can be handled easily by using Ewald's method or any other spatial Green's function representation in combination with the singularity subtraction method.

IV. Ewald's Method

Rather than summing the fields either in the spatial or spectral domain, one can perform the summation over both domains simultaneously using Ewald's summation method. In the Ewald summation, only a few spectral and spatial terms are needed, since the series exhibit Gaussian decay

for both the spectral and spatial summation. Using the integral representation of the free-space Green's function, i.e., $\exp(-jkR)/R = \int_0^\infty \exp(-R^2\epsilon^2 + k^2/(4\epsilon^2))\mathrm{d}\epsilon$, where the integration path is taken in the complex plane as indicated in [9], the periodic Green's function is split up as

$$G = G_{\text{spatial}} + G_{\text{spectral}} \tag{7}$$

where the spatial and the spectral part of the Green's function are defined by

$$G_{\text{spatial}} = \frac{1}{2\pi^{3/2}} \sum_{n=-\infty}^{\infty} \int_E^\infty e^{-R_n^2\epsilon^2 + \frac{k^2}{4\epsilon^2}} \mathrm{d}\epsilon \tag{8a}$$

$$G_{\text{spectral}} = \frac{1}{2\pi^{3/2}} \sum_{n=-\infty}^{\infty} \int_0^E e^{-R_n^2\epsilon^2 + \frac{k^2}{4\epsilon^2}} \mathrm{d}\epsilon. \tag{8b}$$

where E is the Ewald splitting parameter. Since the complementary error function is defined as

$$\operatorname{erfc}(z) = \frac{2}{\sqrt{\pi}} \int_z^\infty e^{-t^2} \mathrm{d}t \tag{9}$$

it can be shown that (8a) can be evaluated as [9]

$$G_{\text{spatial}} = \frac{1}{8\pi} \sum_{n=-\infty}^{\infty} \frac{1}{R_n} \left[e^{jkR_n} \operatorname{erfc}\left(R_n E + \frac{jk}{2E}\right) + e^{-jkR_n} \operatorname{erfc}\left(R_n E - \frac{jk}{2E}\right) \right] \tag{10}$$

Finally, it can also be shown that [10]

$$G_{\text{spectral}} = \frac{1}{4\pi d} \sum_{n=-\infty}^{\infty} e^{jk_{z,n}z} \sum_{q=0}^{\infty} \frac{1}{q!} (j\rho E)^{2q} \mathcal{E}_{q+1}\left(\frac{-\alpha_n^2}{4E^2}\right) \tag{11}$$

where the qth-order exponential integral defined as

$$\mathcal{E}_q(z) = \int_1^\infty \frac{e^{-zt}}{t^q} \mathrm{d}t \qquad (q = 0, 1, ...; \Re\mathrm{e}\{z\} > 0). \tag{12}$$

As mentioned in [10], the recursive relation $\mathcal{E}_{q+1}(z) = q^{-1}[e^{-z} - z\mathcal{E}_q(z)]$, for $n = 1, 2, ...$, is useful for the numerical evaluation of (11), so that only the exponential integral $\mathcal{E}_1(z)$ needs to be explicitely evaluated. Furthermore, in the absence of losses, and for propagating waves, $\alpha_n > 0$, which causes the argument of the exponential integral in (11) to become negative. In our case of lossless media, the evaluation of $\mathcal{E}_{q+1}(z)$ is performed through the formula $\mathcal{E}_1(-z + j0^+) = -\mathrm{Ei}(z) - j\pi$, and the improper integral

$$\mathrm{Ei}(z) = -\mathrm{P.V.} \int_{-z}^\infty \frac{e^{-t}}{t} \mathrm{d}t \qquad z > 0 \tag{13}$$

where P.V. denotes the Cauchy principal-value integration [11].

A. A Note on Ewald's Splitting Parameter

To obtain an optimum value for Ewald's splitting parameter E, one first examines the convergence of G_{spectral} and G_{spatial} given in (11) and (10), respectively. In the spatial summation, the compementary error function for large arguments behaves as

$$\operatorname{erfc}(z) \sim e^{-z^2}/(\sqrt{\pi}z), \quad \text{for } |z| \to \infty \tag{14}$$

so that, in the spatial summation,

$$\begin{aligned} e^{-(R_n E \pm \frac{jk}{2E})^2} &= e^{-(R_n^2 E^2 \pm jkR_n - \frac{k^2}{4E^2})} \\ &= e^{-R_n^2 E^2 (1 \pm \frac{jk}{R_n E^2} - \frac{k^2}{4R_n^2 E^4})} \\ &\sim e^{-R_n^2 E^2} \qquad \text{for large value of } n \end{aligned} \tag{15}$$

In the spectral summation, the exponential integral behaves for large arguments as

$$\mathcal{E}_{q+1}(z) \sim e^{-z}/z \tag{16}$$

as a result of which (11) behaves as $\sim \exp(\alpha_n^2/(4E^2))$ for large values of n. The optimum splitting parameter is found by enforcing the rates of decay (convergence) of both the spectral and spactial summation to be equal, which means that $\alpha_n^2 = -4R_n^2E^4$. This equality results in the optimum splitting parameter [9]

$$E = \frac{\sqrt{\pi}}{d_z}. \tag{17}$$

As discussed in [10], the numerical instability of (7) at high frequencies – or large inter-element spacings d – leads to another choice of the optimum splitting parameter E. In our case, however, since the inter-element spacing $d < \lambda$, the optimum splitting parameter in (17) is a sufficiently good choice.

V. Numerical Results

In this section, we asses the convergence behavior of the periodic Green's function for the spectral, spatial, and the Ewald summation methods, applied to the situation as depicted in Fig. 2. The convergence rate is examined through the relative error

$$\text{Rel. Error} = \sqrt{\frac{|G^{\text{exact}} - G^{\text{Spectral,Spatial,Ewald}}|^2}{|G^{\text{exact}}|^2}} \times 100\% \tag{18}$$

where G^{exact} constitutes the reference solution, which is taken to be the spectral or spatial Green's function, evaluated for a sufficiently large number of terms.

Table I shows the computation times for evaluating only one spatial, spectral, and Ewald term. To minimize estimation error, we have computed the *average* evaluation time based on a large number of realizations. The computations were carried out in Matlab (operating system: Windows Vista Business), on a 2.3 GHZ AMD Athlon(tm) 64 X2 Dual Core Processor 4400+, equipped with 4 GB of RAM memory.

TABLE I
Series evaluation time for a single term as used in (1) and (2).

T_0^{spatial} [sec]	T_0^{spectral} [sec]	T_0^{Ewald} [sec]
3.1843×10^{-6}	1.4882×10^{-4}	2.9000×10^{-3}

Table II illustrates the extrapolation times $T_e^{\text{Shanks},n}$ of the repeated Shanks transformation, i.e., for several Shanks-orders n [*cf.* Eq. (2)].

TABLE II
INFINITE SERIES EXTRAPOLATION TIME $T_E^{\text{SHANKS},n}$ AS USED IN (2), FOR SEVERAL SHANKS ORDERS n.

$T_e^{\text{Shanks},1}$ [sec]	$T_e^{\text{Shanks},2}$ [sec]	$T_e^{\text{Shanks},3}$ [sec]	$T_e^{\text{Shanks},4}$ [sec]
2.1508×10^{-5}	4.4158×10^{-5}	7.3252×10^{-5}	11.885×10^{-5}

Fig. 4 shows that, although the number of terms required to reach a certain accuracy of the Green's function decreases for an increasing order of the Shanks transformation, the series evaluation time also increases, as illustrated in Fig. 5 and in accordance with Eq. (2). It is concluded from Fig. 5 that, in order to reach the relative error $\epsilon < 0.01\%$ (which is typically good enough in practice), the 2nd-order Shanks transformation is generally the fastest among the other spatial series summations (region of validity: $0.1\lambda \leq \rho \leq \lambda$; $0.1\lambda \leq d \leq 0.9\lambda$).

In Fig. 6, the error of the spectral summation is computed relative to its exact value G_{spectral}. As expected – based on the physical field interpretation in Fig. 2 – the relative error increases for a larger plate distance d, while it decreases for larger ρ. It is worth noting that the minimum evaluation time (only one term) for the spectral summation already exceeds 10^{-4} sec, which is independent of the source-observation and the plate distance d. Hence, for $0.1\lambda \leq \rho \leq \lambda$, the Shanks-2-transformed Green's function summation outperforms the spectral Green's function summation if a relative (though typical) accuracy of $\epsilon \sim 0.01\%$ is desired.

In Fig. 7, one can observe the relative error of the Ewald summation, as computed in (18), versus the number of Ewald terms. The curves are for two observation points, i.e. for $\rho = 0.01\lambda$, and 0.1λ, and for the plate distances $d = .1\lambda$, $.3\lambda$, $.5\lambda$, and $.9\lambda$. The optimum Ewald splitting parameter is selected according to Eq. (17). The number of q-terms in (11) is set to $Q = 20$, which is large enough for the cases presently considered [10]. Fig. 7 also shows that, for more than one Ewald term, a relative error with seven digits of accuracy has already been obtained for all the d values, while this relative error is not decreasing further for an increasing number of Ewald terms [10].

It is overall concluded that, for the cases studied, the Ewald method converges faster than both the Shanks-transformed spatial and spectral Green's function summation. The relative accuracy achieved after one Ewald term is already $\sim 10^{-5}\%$, which may, however, be larger than strictly required in most computations that are of practical interest, particularly if one realizes that the numerical evaluation of one Ewald term is relatively time-consuming. The Shanks-2-transformed spatial Green's function summation seems to the best choice for our purposes and for a minimum required relative accuracy of about 0.01%. Only for $\rho >\sim \lambda$, the spectral Green's function summation becomes the preferred option, while the Ewald method may become unstable for large ρ.

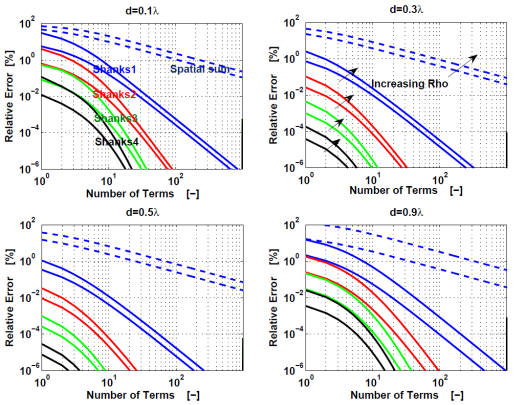

Fig. 4. Relative error, Eq. (18), for the spatial summation and the repeated Shanks transformation as a function of the number of terms for $\rho = 0.1\lambda$ and $\rho = 0.5\lambda$, the direction of increasing ρ is visualized in the figure.

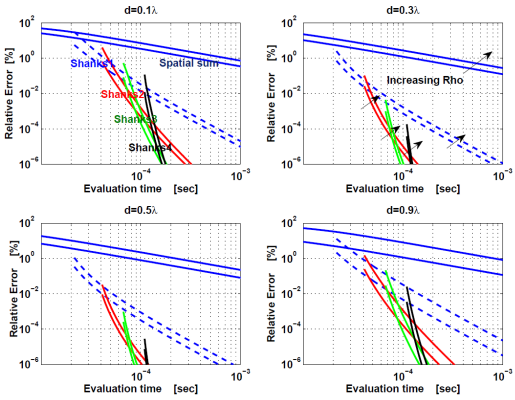

Fig. 5. Relative error, Eq. (18), for the spatial Green's function summation and the repeated Shanks transformations as a function of the evaluation time, Eq. (2), for $\rho = 0.1\lambda$ and 0.5λ.

VI. CONCLUSIONS

Several different acceleration methods have been implemented for computing the parallel-plate Green's function. The convergence properties of the Shanks-transformed spatial Green's function summation, the spectral Green's function summation, and Ewald's hybrid series representation for the parallel-plate Green's function have been examined with the aid of several numerical examples. In addition, the total evaluation time for each of the methods to reach a minimum required accuracy has been analyzed.

It has been concluded that, for the cases studied, the Ewald

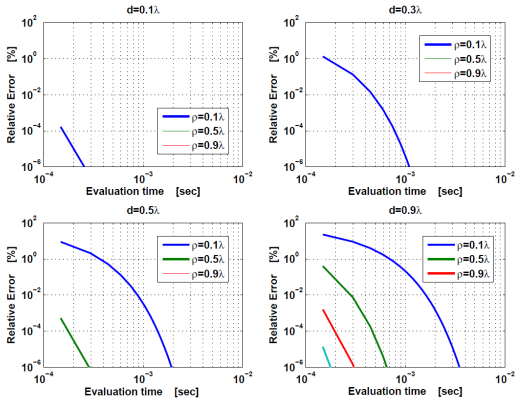

Fig. 6. Relative error, Eq. (18), for the spectral Green's function summation as a function of the total evaluation time, Eq. (1).

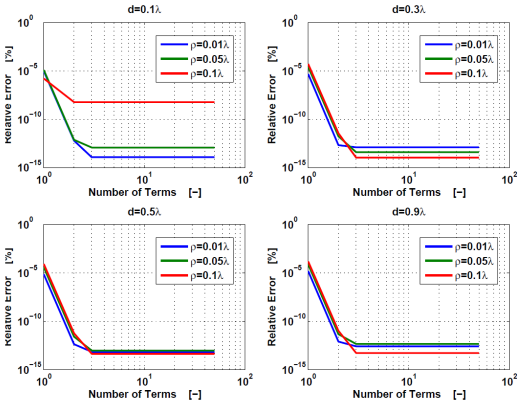

Fig. 7. Relative error, Eq. (18), for the Ewald summation as a function of the number of Ewald terms

method converges faster than both the Shanks-transformed spatial and spectral Green's function summation. The relative accuracy achieved after one Ewald term is already $\sim 10^{-5}\%$, which may, however, be larger than strictly required in most practical computations. This is particularly important if one realizes that the numerical evaluation of one Ewald term is relatively time-consuming. The Shanks-2-transformed spatial Green's function summation seems to the best choice for our purposes, where a minimum required relative accuracy of about 0.01% is required. Only for $\rho >\sim \lambda$, the spectral Green's function summation becomes the preferred option, while the Ewald method may become unstable for large ρ.

ACKNOWLEDGMENT

This work is part of the research programme Rubicon, which is partly financed by the Netherlands Organization for Scientific Research (NWO).

REFERENCES

[1] P.-S. Kildal, E. Alfonso, A. Valero-Nogueira, and E. Rajo-Iglesias, "Local metamaterial-based waveguides in gaps between parallel metal plates," *IEEE Antennas Wireless Propag. Lett.*, vol. 8, no. 1, pp. 84–87, 2009.

[2] P.-S. Kildal, "Three metamaterial-based gap waveguides between parallel metal plates for mm/submm waves," in *Proc. European Conference on Antennas and Propag. (EuCAP)*, Berlin, Germany, Mar. 2009, pp. 23–27.

[3] P.-S. Kildal, A. U. Zaman, E. Rajo-Iglesias, E. Alfonso, and A. Valero-Nogueira, "Design and experimental verification of ridge gap waveguides in bed of nails for parallel plate mode suppression," *Microwaves, Antennas & Propagation, IET*, vol. 5, no. 3, pp. 262–270, Mar. 2011.

[4] M. Bosiljevac, Z. Sipus, and P.-S. Kildal, "Construction of green's functions of parallel plates with periodic texture with application to gap waveguides - a plane wave spectral domain approach," *Microwaves, Antennas & Propagation, IET*, vol. 4, no. 11, pp. 1799–1810, Nov. 2010.

[5] S. Singh and R. Singh, "Application of transforms to accelerate the summation of periodic free-space green's functions," *IEEE Trans. Microw. Theory Tech.*, vol. 38, no. 11, pp. 1746–1748, Nov. 1990.

[6] C. Craeye, A. G. Tijhuis, and D. H. Schaubert, "An efficient MoM formulation for finite-by-ininite arrays of two-dimensional antennas arranged in a three dimensional structure," *IEEE Trans. Antennas Propag.*, vol. 51, no. 9, pp. 2054–2056, Sep. 2003.

[7] P. P. Ewald, "Die berechnung optischer und elektrostatischen gitterpotentiale," *Ann. Phys.*, vol. 64, pp. 253–268, 1921.

[8] S. Singh, W. F. Richards, J. R. Zinecker, and D. R. Wilton, "Accelerating the convergence of series representing the free space periodic green's function," *IEEE Trans. Antennas Propag.*, vol. 38, no. 12, pp. 1958–1962, Dec. 1990.

[9] A. Kustepeli, "Analysis and implementation of the ewald method for waveguide and cavity structures," Ph.D. dissertation, Clemson University, dec. 1999.

[10] F. Capolino, D. Wilton, and W. Johnson, "Efficient computation of the 3d green's function for the helmholtz operator for a linear array of point sources using the ewald method," *Journal of Computational Physics*, vol. 223, no. 1, pp. 250–261, Nov. 2007.

[11] M. Abramowitz and I. A. Stegun, *Handbook of Mathematical Functions*. Dover, 1970.

Fast Analysis of Gap Waveguides Using the Characteristic Basis Function Method and the Parallel-Plate Green's Function

R. Maaskant* P. Takook† P.-S. Kildal‡

Abstract — **The Characteristic Basis Function Method is employed in conjunction with the parallel-plate dyadic Green's function method to obtain the impedance characteristics of electrically large gap-waveguide structures. Numerical results are shown for the groove gap waveguide demonstrating reduced execution times relative to the HFSS software, while the solution accuracy is barely compromised.**

1 INTRODUCTION

To anticipate to future trends in high-frequency electronics, a novel low-loss low-cost waveguide and transmission-line technology has been proposed – referred to as the gap waveguide technology [1]. The basic structure consists of a pair of perfect electric conducting (PEC) top and bottom ground planes in conjunction with a bed of nails for realizing a perfect magnetic conductor (PMC) boundary condition. Fig. 1 illustrates an example of a groove

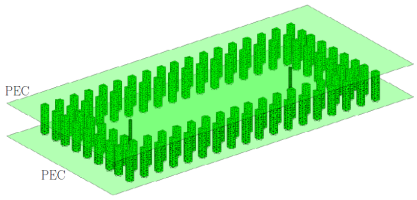

Figure 1: Coaxial-probe excited groove gap waveguide.

gap waveguide, where two coaxial probes are used to excite the waveguide fields. The groove is bordered by only a few rows of pins to prevent the fields from leaking out (sideways) when operating in the stop band. The pins are electrically interconnected to the bottom PEC plate, while no electrical contact between the pins and the upper PEC plate is required. The so-formed capacitive gap in the "gap waveguide" is not only needed to realize the PMC, but represents a mechanical advantage as well.

To allow for a fast analysis and optimization of gap waveguides, it is required to develop tailored computational electromagnetic methods that are numerically efficient. In this paper, we propose to employ the Characteristic Basis Function Method (CBFM, [2]) in conjunction with the parallel-plate Green's function [3]. This methodology enhances the computational efficiency of conventional method of moment (MoM) codes significantly. Furthermore, the CBFM is memory efficient and allows us to solve problems that are typically 1–3 orders larger in size.

2 PARALLEL PLATE DYADIC GREEN'S FUNCTION

Consider Fig. 2, where the EM field of a dipole point source inside a parallel-plate region is computed with the help of the image principle. Depending upon whether the dipole has an x-, y-, or z-orientation, the field for each polarization is regarded as being radiated by two superimposed 1D-line arrays of dipole point sources with the original and possibly mirrored polarization, respectively. Each line array has an inter-dipole spacing of twice the plate distance. In Dyadic form, the spatial parallel-plate Green's function $\mathbf{G}$ is expressed as $\mathbf{G}(\boldsymbol{r},\boldsymbol{r}') = G^N_{xx}\hat{\boldsymbol{x}}\hat{\boldsymbol{x}}^T + G^N_{yy}\hat{\boldsymbol{y}}\hat{\boldsymbol{y}}^T + G^N_{zz}\hat{\boldsymbol{z}}\hat{\boldsymbol{z}}^T$, where

$$\begin{aligned} G^N_{xx} &= \sum_{n=-N}^{N} \frac{e^{-jk_0\sqrt{\rho^2+(z-z'+2dn)^2}}}{4\pi\sqrt{\rho^2+(z-z'+2dn)^2}} \\ &\quad - \sum_{n=-N}^{N} \frac{e^{-jk_0\sqrt{\rho^2+(z+z'+2d(n-1))^2}}}{4\pi\sqrt{\rho^2+(z+z'+2d(n-1))^2}} \\ G^N_{yy} &= G^N_{xx} \\ G^N_{zz} &= \sum_{n=-N}^{N} \frac{e^{-jk_0\sqrt{\rho^2+(z-z'+2dn)^2}}}{4\pi\sqrt{\rho^2+(z-z'+2dn)^2}} \\ &\quad + \sum_{n=-N}^{N} \frac{e^{-jk_0\sqrt{\rho^2+(z+z'+2d(n-1))^2}}}{4\pi\sqrt{\rho^2+(z+z'+2d(n-1))^2}} \end{aligned} \quad (1)$$

*Chalmers University of Technology, Dept. of Signals and Systems, 412 96, Gothenburg , Sweden, e-mail: rob.maaskant@chalmers.se

†Chalmers University of Technology, Dept. of Signals and Systems, 412 96, Gothenburg , Sweden, e-mail: takook@student.chalmers.se

‡Chalmers University of Technology, Dept. of Signals and Systems, 412 96, Gothenburg , Sweden, e-mail: per-simon.kildal@chalmers.se

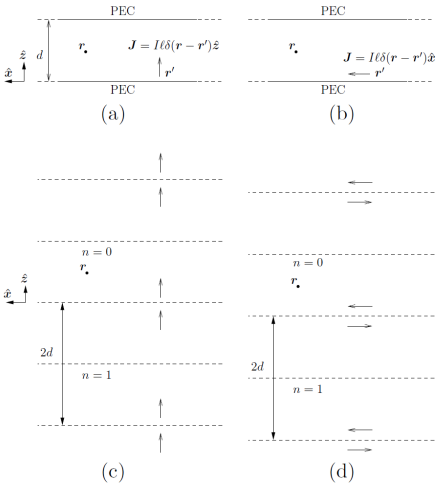

Figure 2: (a) z-polarized and (b) x-polarized electric Hertzian dipole currents in between two infinitely large parallel PEC plates separated by a distance d; (c) and (d), the repeated application of the image principle for both dipole polarizations, respectively.

for $N \to \infty$, and where we have defined that $\rho^2 = (x - x')^2 + (y - y')^2$. It is well-known that each summation in Eq. (1) is performed over a slowly convergent series. However, the field of a line array can be computed rapidly using the Shanks-accelerated spatial Green's function method. Other methods, such as the Ewald summation method, or the spectral-domain summation method, were found to be less efficient for our type of problems [3]. For instance, the Ewald summation method requires very few terms in the near-field region of the source, but the computation time of a single term is orders larger than that of a spatial Green's function term. Furthermore, if only a few digits accuracy is required, which is often sufficiently good, only a few terms are needed. In fact, we found that for our type of problems, the overall series evaluation time is shortest for the Shanks-accelerated spatial Green's function method. Finally, we point out that the Shanks transformation is easy to implement. For example, when considering the new series G_{xx}^N, for $N = 1, 2, \ldots$, the extrapolated value for $N \to \infty$ is

$$G_{xx}^{\infty} \approx \frac{G_{xx}^{N+1} G_{xx}^{N-1} - \left(G_{xx}^{N}\right)^2}{G_{xx}^{N+1} - 2G_{xx}^{N} + G_{xx}^{N-1}} \qquad (2)$$

where N is taken sufficiently large. We concluded that the double Shanks tranformation on the orignal spatial Green's function series represents the best trade off between the solution accuracy and the total series evaluation time [3].

3 CHARACTERISTIC BASIS FUNCTION METHOD

To minimize the total number of basis functions, entire-domain basis functions are employed for the electric surface currents on the conductors inside the gap waveguide; in this specific case on the pins and coaxial probes only. Each of these so-called Characteristic Basis Functions (CBFs) is expanded in terms of a fixed combination of lower-level basis functions, which are herein chosen to be the Rao-Wilton-Glisson (RWG) basis functions. The CBFs are generated for a small part of the structure only, namely by solving for the current in the corresponding subdomain. As an example, consider Fig. 3, where the CBFs are generated for one of the pins. Here, each pin consists of 382 RWGs. A

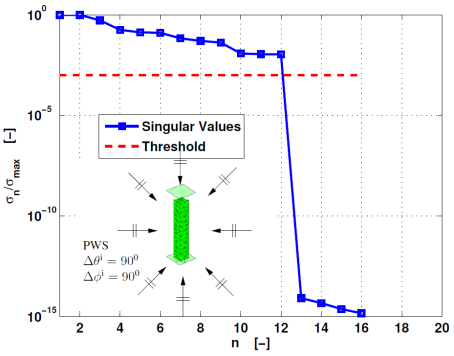

Figure 3: Generation of CBFs on a pin using a plane wave spectrum (PWS). The singular value spectrum is shown where a threshold is used to limit the maximum number of employed CBFs.

plane wave spectrum is incident on the pin with $\Delta\theta^i = \Delta\phi^i = 90^0$ (and two polarizations). This generates 16 currents on the pin. The currents are stored as RWG expansion coefficients vectors and make up the columns of the matrix $\mathbf{J} = \mathbf{UDV}^H$, where the right-hand side is the SVD of $\mathbf{J}$. The magnitude of the normalized singular values in $\mathbf{D}$ are plotted in Fig. 3. With an appropriate thresholding procedure on the singular values, only the first 12 column vectors of the left-singular matrix $\mathbf{U}$ are retained and subsequently used as CBFs. The

reduction in the number of unknowns per pin is therefore 382/12=31.8 (@ 12 GHz).

Since the set of CBFs is identical for each pin, we use symmetry to generate a set for all the pins through translation [4]. The same procedure is followed for the coaxial probes. More details on the generation of CBFs can be found in [2], where also electrically interconnected subdomains are considered.

After generating the CBFs for all M subdomains, i.e., $\mathbf{J}_m$, for $m = 1, 2, \ldots, M$, one can construct the reduced moment matrix equation $\mathbf{Z}^{\text{red}}\mathbf{I}^{\text{red}} = \mathbf{V}^{\text{red}}$, where

$$\mathbf{Z}^{\text{red}} = \begin{bmatrix} (\mathbf{J}_1)^T \mathbf{Z}_{11}\mathbf{J}_1 & \cdots & (\mathbf{J}_1)^T \mathbf{Z}_{1M}\mathbf{J}_M \\ \vdots & \ddots & \vdots \\ (\mathbf{J}_M)^T \mathbf{Z}_{M1}\mathbf{J}_1 & \cdots & (\mathbf{J}_M)^T \mathbf{Z}_{MM}\mathbf{J}_M \end{bmatrix} \tag{3}$$

and

$$\mathbf{V}^{\text{red}} = \left[(\mathbf{J}_1)^T \mathbf{V}_1, \cdots, (\mathbf{J}_M)^T \mathbf{V}_M \right]^T \tag{4}$$

and where the elements of the matrix block $\mathbf{Z}_{mn}$ are the reaction integrals between the RWG basis functions on the nth source and mth observation subdomain, respectively. Likewise, $\mathbf{V}_m$ is the original RWG voltage excitation vector for the mth subdomain, where the incident electric field is generated by the impressed magnetic frill currents that are supported by the coaxial apertures. This CBFM procedure leads to a reduced MoM matrix equation which can be solved in-core using standard Gaussian elimination techniques.

One observes that the CBFM can be regarded as an enhancement technique for conventional MoM approaches, since the original MoM-matrix blocks and excitation vectors are reduced with the help of the above-described CBFs. Although the methodology is very general and independent of the Green's function, in this work the MoM is used to discretize an Electric Field Integral Equation (EFIE) for the electric current inside a parallel-plate waveguide region using Galerkins method and RWG basis and test functions.

Finally, the CBFM is memory efficient and allows us to solve problems that are many wavelengths in size, even though the structure exhibits very fine geometrical features requiring detailed discretizations (multi-scale features).

4 Numerical Results

In this section the numerical results on the groove gap waveguide are presented, whose geometrical dimensions are as described in Table 1. Additionally,

Table 1: Geometrical dimensions of the Groove gap waveguide in [mm].

W_{pin}	H_{pin}	L_1	L_2	L_3	L_4
1	6.25	15.8	43.7	5.4	2

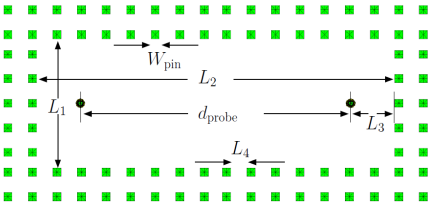

the radius and length of the coaxial probes are 0.25 and 5 mm, respectively. The parallel-plate distance $d = 7.25$ mm.

The CBFM computations have been carried out on a 64 bit (x86-64) Linux – openSUSE (v.11.4) server equipped with 2 Intel Xeon E5640 CPUs operating at 2.67 GHz (each CPU has 4 cores/8 threads), with access to 144 GB RAM memory and 2 TB harddisk space. The HFSS simulations were performed on a 64 bit Windows XP server equipped with 2 Intel Xeon 5130 CPUs operating at 2 GHz (each CPU has 2 cores/2 threads), 8 GB RAM, and 300 GB harddisk space.

Firstly, to verify the accuracy of CBFM, the 100-Ohm S-parameters for the gap waveguide structure (*cf.* Table 1) have been computed, both by our CBFM-enhanced MoM procedure and the HFSS software. In HFSS, the adaptive meshing terminates if the relative field error is less than 1%. The computed S-parameters for CBFM and HFSS are shown in Fig. 4 and are in good agreement. The solve times for this relatively small problem is 1 min. 41 sec. and 1 min. 24 sec. for CBFM and HFSS, respectively. The simulation times are comparable due to the relatively large overhead needed by the CBFM to determine the CBFs. The CBFM employed 37088 RWGs (1112 CBFs), while HFSS employed 42158 tetrahedra. Owing to the array structure, the meshing time is only 5 sec. for the CBFM, while it takes 3 min. 57 sec. for HFSS.

By changing L_2 one can examine the total solve time as a function of the problem size. The results are shown in Fig. 5, where the scaling of the solve time for CBFM outforms that of HFSS by about a factor of three. Also, for equal simulation times, the problem size for CBFM can be about twice larger than for the HFSS software. The HFSS software

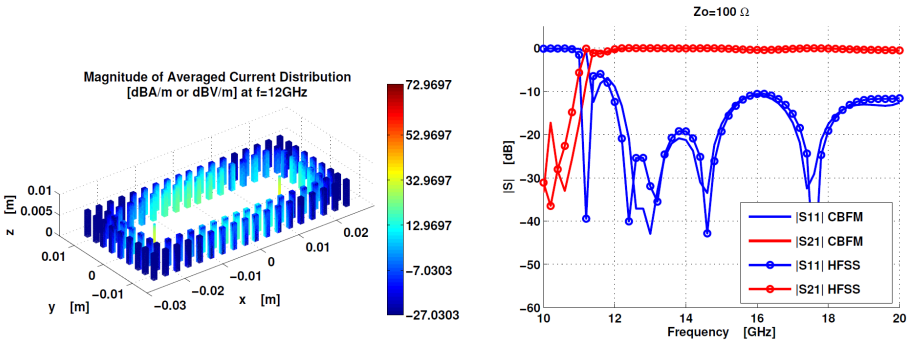

(a) (b)

Figure 4: (left) the magnitude of the computed electric current and S-parameters of a groove gap-waveguide when excited by a pair of coaxial probes; (right) the numerical results are computed by the CBFM employing the parallel-plate Greens function. The numerically computed results are validated through the HFSS software.

could not handle problems for $d_{\text{probe}} > 1.3$ m, due to memory constraints for that server. The non-gradual increase in simulation time is caused by the adaptive meshing of HFSS.

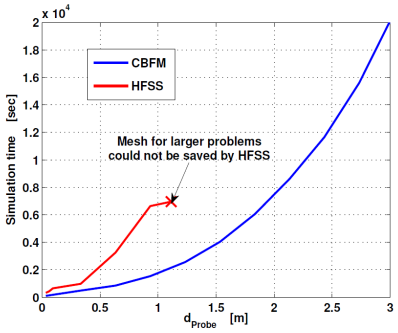

Figure 5: Scaling of the method: the total solve time as a function of problem size (d_{probe}).

5 Conclusions

The CBFM has been supplemented with the parallel-plate Green's function to enable the fast analysis of gap waveguide structures. By comparing the computed S-parameters obtained from CBFM and the HFSS software, it has been concluded that the solution accuracy for the CBFM is hardly compromised, while it is at least a factor three faster than the HFSS software.

Acknowledgments

This work is part of the research programme Rubicon, which is partly financed by the Netherlands Organization for Scientific Research (NWO).

References

[1] P.-S. Kildal, E. Alfonso, A. Valero-Nogueira, and E. Rajo-Iglesias, "Local metamaterial-based waveguides in gaps between parallel metal plates," *IEEE Antennas Wireless Propag. Lett.*, vol. 8, no. 1, pp. 84–87, 2009.

[2] R. Maaskant, R. Mittra, and A. G. Tijhuis, "Application of trapezoidal-shaped characteristic basis functions to arrays of electrically interconnected antenna elements," in *Proc. Int. Conf. on Electromagn. in Adv. Applicat. (ICEAA)*, Torino, Sep. 2007, pp. 567–571.

[3] P. Takook, R. Maaskant, and P.-S. Kildal, "Comparison of parallel-plate greens function acceleration techniques," in *Proc. European Conference on Antennas and Propag. (EuCAP)*, Prague, Czech Republic, Mar. 2012, pp. 1–5.

[4] R. Maaskant, R. Mittra, and A. G. Tijhuis, "Fast solution of multi-scale antenna problems for the square kilomtre array (SKA) radio telescope using the characteristic basis function method (CBFM)," Applied Computational Electromagnetics Society (ACES) Journal, vol. 24, no. 2, pp. 174–188, Apr. 2009.

Bibliography

[1] P.-S. Kildal, "Three metamaterial-based gap waveguides between parallel metal plates for mm/submm waves," in *Proc. European Conference on Antennas and Propag. (EuCAP)*, Berlin, Germany, Mar. 2009, pp. 23–27.

[2] M. Bosiljevac, A. Polemi, S. Maci, and Z. Sipus, "Analytic approach to the analysis of ridge and groove gap waveguides comparison of two methods," in *Proc. European Conference on Antennas and Propag. (EuCAP)*, Rome, Apr. 2011, pp. 1886–1889.

[3] M. Bosiljevac, Z. Sipus, and P.-S. Kildal, "Construction of green's functions of parallel plates with periodic texture with application to gap waveguides - a plane wave spectral domain approach," *IET*, vol. 4, pp. 1799–1810, Nov. 2010.

[4] E. Pucci, "Characterization of losses in ridge, groove and microstrip gap waveguides," Ph.D. dissertation, Chalmers University of Technology, 2011.

[5] P.-S. Kildal, A. U. Zaman, E. Rajo-Iglesias, E. Alfonso, and A. Valero-Nogueira, "Design and experimental verification of ridge gap waveguides in bed of nails for parallel plate mode suppression," *IET*, vol. 5, no. 3, pp. 262–270, Mar. 2011.

[6] C. A. Balanis, *Advanced Engineering Electromagnetics*. New York: John Wiley and Sons, Inc., 1989.

[7] ——, *Antenna Theory, Analysis and Design, third edition*. New York: John Wiley and Sons, Inc., 2005.

[8] P. P. Ewald, "Die berechnung optischer und elektrostatischen gitterpotentiale," *Ann. Phys.*, vol. 369, pp. 253–268, 1921.

[9] F. Capolino, D. Wilton, and W. Johnson, "Efficient computation of the 3d green's function for the helmholtz operator for a linear array of point sources using the ewald method," *Journal of Computational Physics*, vol. 223, pp. 250–261, nov. 2007.

[10] ——, "Efficient computation of the 2-d green's function for 1-d periodic structures using the ewald method," *Antennas and Propagation, IEEE Transactions on*, vol. 53, no. 9, pp. 2977–2984, sept. 2005.

[11] C. Craeye, A. G. Tijhuis, and D. H. Schaubert, "An efficient MoM formulation for finite-by-ininite arrays of two-dimensional antennas arranged in a three dimensional structure," *IEEE Trans. Antennas Propag.*, vol. 51, no. 9, pp. 2054–2056, Sep. 2003.

[12] I. S. M. Abramowitz, *Handbook of Mathematical Functions.* Dover, 1970.

[13] A. Kustepeli, "Analysis and implementation of the ewald method for waveguide and cavity structures," Ph.D. dissertation, Clemson University, dec. 1999.

[14] S. Singh and R. Singh, "Application of transforms to accelerate the summation of periodic free-space green's functions," *IEEE Trans. Microw. Theory Tech.*, vol. 38, no. 11, pp. 1746–1748, Nov. 1990.

[15] S. Singh, W. F.Richards, J. R.Zinecker, and D. R. Wilton, "Accelerating the convergence of series representing the free space periodic greens function," *Antennas and Propagation, IEEE Transactions on*, vol. 38, no. 12, pp. 1958–1962, Dec 1990.

[16] D. Shanks, "Non-linear transformations of divergent and slowly convergent sequences," *Math, Physics*, vol. 34, pp. 1–42, 1955.

[17] P. Wynn, "On a device for computing the $e_m(s_n)$ transformation," *Math, Physics*, vol. 10, pp. 91–96, 1956.

[18] F. J. Perez, F. Quesada, A. Alvarez, E. Sorolla, and B. Gimeno, "Discussion on the efficient evaluation of the greens functions of point sources inside infinite parallel plate waveguides," in *Proc. 3rd EuCAP Conference*, Berlin, Mar. 2009, pp. 163–167.

[19] R. F. Harrington, *Field Computation by Moment Method.* New York: The MacMillan Company, 1968.

[20] J. J. H. Wang, "Generalized moment methods in electromagnetics," *IEE Proceedings*, vol. 137, no. 2, Apr. 1990.

[21] S. M. Rao and D. R. Wilton, "Electromagnetic scattering by surface of arbitrary shape," *IEEE Trans. Antennas Propag.*, vol. AP-30, no. 3, May 1982.

[22] R. Maaskant, "Analysis of large antenna systems," Ph.D. dissertation, Eindhoven University of Technology, 2010.

[23] D. R. Wilton, S. M. Rao, A. W. Glisson, D. H. Schaubert, O. M. Al-Bundak, and C. M. Butler, "Potential integrals for uniform and linear source distributions on polygonal and polyhedral domains," *IEEE Trans. Antennas Propag.*, vol. 32, no. 3, pp. 276–281, Mar. 1984.

[24] P. Y. Oijala and M. Taskinen, "Calculation of cfie impedance matrix elements with RWG and $\boldsymbol{n}\times$RWG functions," *Antennas and Propagation, IEEE Transactions on*, vol. 51, no. 8, Aug. 2003.

[25] R. Maaskant and B. Yang, "A combined electromagnetic and microwave antenna system simulator for radio astronomy," in *Proc. European Conference on Antennas and Propag. (EuCAP)*, Nice, France, Nov. 2006, pp. 1–4.

[26] A. U. Zaman, "Gap waveguide for high frequency microwave application," Ph.D. dissertation, Chalmers University of Technology, 2011.

[27] (2012) Wikipedia, the free encyclopedia. [Online]. Available: http://en.wikipedia.org/wiki/Coaxial_cable

[28] A. Corp., High Frequency Structure Simulator Users Guide, 2008.

[29] E. K. Miller, "Model-based parameter estimation in electromagnetics. i. background and theoretical development," *Antennas and Propagation, IEEE Transactions on*, vol. 40, pp. 42–52, Feb 1998.

[30] D. H. Werner and R. J. Allard, "The simultaneous interpolation of antenna radiation patterns in both the spatial and frequency domains using model-based parameter estimation," *Antennas and Propagation, IEEE Transactions on*, vol. 48, no. 3, pp. 383–392, Mar 2000.

[31] M. Hamid and R. Hamid, "Equivalent circuit of dipole antenna of arbitrary length," *Antennas and Propagation, IEEE Transactions on*, vol. 45, no. 11, pp. 1695–1696, Nov 1997.

[32] R. S. Elliott, *Antenna Theory and Design.* Englewood Cliffs, NJ: Prentice-Hall, 1981.

[33] E. K. Miller, "Using adaptive estimation to minimize the number of samples needed to develop a radiation or scattering pattern to a specified uncertainty," *ACES*, vol. 17, no. 3, pp. 176–186, Nov 2002.

[34] ——, "Using adaptive sampling to minimize the number of samples needed to represent a transfer function," *Antennas and Propagation Society International Symposium, 1996. AP-S. Digest*, vol. 1, pp. 588–591, Jul 1996.

[35] J. Heinstadt, "New approximation technique for current distribution in microstrip array antennas," *Microwave and Optical Technology Letters*, vol. 29, pp. 1809–1810, Oct 1993.

[36] V. V. Prakash and R. Mittra, "Characteristic basis function mehod: A new technique for efficient solution of method of moments matrix equations," *Microwave and Optical Technology Letters*, vol. 36, no. 2, Jan. 2003.

[37] W. B. Lu, T. J. Cui, Z. G. Qian, X. X. Yin, and W. Hong, "Accurate analysis of large-scale periodic structures using an efficient sub-entire-domain basis function method," *Antennas Propagation, IEEE Transactions on*, vol. 52, no. 11, pp. 3078–3085, Nov 2004.

[38] D. J. Bekers, S. J. L. van Eijndhoven, A. A. F. van de Ven, P. P. Borsboom, and A. G. Tijhuis, "Eigencurrent analysis of resonant behavior in finite antenna arrays," *Microwave. Theory Tech., IEEE Transactions on*, vol. 54, no. 6, pp. 2821–2829, Jun 2006.

[39] C. Craeye, "A fast impedance and pattern computation scheme for finite antenna arrays," *Antennas Propag, IEEE Transactions on*, vol. 54, no. 10, pp. 3030–3034, Oct 2006.

[40] M. B. E. Bleszynski and T. Jaroszewicz, "Aim: Adaptive integral method for solving large-scale electromagnetic scattering and radiation problems," *Radio Science*, vol. 31, no. 5, pp. 1225–1251, Sep 1996.

[41] K. Zhao, M. N. Vouvakis, and J. F. Lee, "The adaptive cross approximation algorithm for accelerated method of moments computations of EMC problems," *IEEE Trans. Electromagn. Compat.*, vol. 47, no. 4, pp. 763–773, Nov. 2005.

[42] G. H. Golub and C. F. van Loan, *Matrix Computations*. Baltimore,MD: Johns Hopkins, 1996.